Stable water isotopes in the global water cycle: Atmospheric model simulations and application to proxy data

Dissertation zur Erlangung des akademischen Grades eines
Doktors der Naturwissenschaften

Dr. rer. nat.

im Fachbereich 5 (Geowissenschaften)

der Universität Bremen

vorgelegt von

Thejna Tharammal

Bremen, May 2013

N a m e : ....Thejna Tharammal........................... Datum ....08.05.2013.......

Anschrift : ....Leherheerstrasse 118, Bremen-28359..................................

E r k l ä r u n g

Hiermit versichere ich, dass ich

1. die Arbeit ohne unerlaubte fremde Hilfe angefertigt habe,

2. keine anderen als die von mir angegebenen Quellen und Hilfsmittel benutzt habe und

3. die den benutzten Werken wörtlich oder inhaltlich entnommenen Stellen als solche kenntlich gemacht habe.

_____, den ....

(Unterschrift)

"At the heart of science is an essential balance between two seemingly contradictory attitudes – an openness to new ideas, no matter how bizarre or counterintuitive, and the most ruthlessly sceptical scrutiny of all ideas, old and new. This is how deep truths are winnowed from deep nonsense."

–Carl Sagan [in: *The Demon-Haunted World: Science as a Candle in the Dark (1996), p. 287.*]

Gutachter

Prof. Dr. Michael Schulz

Prof. Dr. Michal Kucera

Promotionskolloquium: 04.07.2013

Mitglieder der Kommission:

Herr Prof. Dr. Michael Schulz
Herr Prof. Dr. Michal Kucera
Herr Prof. Dr. Heiko Pälike
Herr Dr. André Paul
Frau Dr. Aline Govin
Frau Rike Völpel

TABLE OF CONTENTS

Acknowledgements

To my Parents

Abstract

Stable isotopes of water recorded in polar ice cores are used to reconstruct past temperatures and the fractionation during phase changes make them a useful tracer of the hydrological cycle. This study focuses on the global and regional variations in the distribution of water isotopes with changes in the climate. Sensitivity experiments and time-slice simulations for the Last Glacial Maximum (LGM), Heinrich Stadial-1 and mid-Holocene climates were carried out both to understand the boundary conditions that exert the maximum influences on the isotopic composition of precipitation, and to reproduce the isotopic distribution of precipitation during these time periods. The numerical climate model, the National Center for Atmospheric Research (NCAR) Community Atmosphere Model CAM3.0 fitted with an oxygen-isotope module (Iso-CAM), is used to carry out the experiments.

The first part of this study focuses on understanding the distribution of oxygen isotopes in precipitation ($\delta^{18}O_{\text{precip}}$) during the LGM and to associate the anomalies from the control climate with the influence of different boundary condition constraints. Results from a pre-industrial control simulation are compared against experiments in which the influence of individual boundary conditions (greenhouse gases, ice-sheet albedo and topography, sea-surface temperature (SST), and orbital parameters) were changed each at a time to the LGM values to assess their individual impact. The results show that the SST and ice-sheet topography changes during the LGM are responsible for most of the modeled variations in the climate and hence the $\delta^{18}O_{\text{precip}}$ distribution. In this study a detailed analysis of the seasonal and annual variations of $\delta^{18}O_{\text{precip}}$ for the control and a combined LGM simulation is carried out. In addi-

tion, the spatial and temporal slopes between the $\delta^{18}O_{\text{precip}}$ and surface temperature are calculated for the combined LGM and control simulations over Greenland and Antarctica, which are compared with the reconstructions from the ice-cores and those simulated with other isotope models.

Secondly, four different time slice experiments - pre-industrial, mid-Holocene, LGM, and Heinrich Stadial-1 - were carried out to analyze the water isotope distribution over the African continent during these time periods. The local and non-local climate influences on the hydrogen isotope composition of precipitation (δD_{precip}) during these different climates are investigated. The study highlights the strong impact of convection and rainout on the δD_{precip} over the tropics, along with the changes in large-scale circulation. In addition, model results for δD_{precip} for these time periods are compared with δD_{wax} data obtained from the stable hydrogen isotope composition of plant leaf-wax n-alkanes, and show a qualitative agreement between the proxy and the model data.

In a third part of the thesis, the present-day distribution of the isotopes in precipitation and water vapor were compared with the observations. The measurements of isotopes in water vapor have the advantage over the isotopes in precipitation that the observations are available around the year and also over arid regions where the precipitation events are very few. The study highlights the robustness of the results as well as some of the drawbacks of the model due to deficiencies in reproducing the hydrology over the land and because of the simplistic cloud isotope scheme.

Zusammenfassung

Stabile Wasserisotope werden zum Beispiel in Eisbohrkernen aufgezeichnet und erlauben die Rekonstruktion von Temperaturänderungen in der Erdgeschichte. Ihre Fraktionierung bei Phasenübergängen macht sie zu einem nützlichen Tracer für den Wasserkreislauf. Diese Untersuchung konzentriert sich auf die globalen und lokalen Schwankungen in der Verteilung der Wasserisotope, die durch Klimaänderungen hervorgerufen werden. Es wurden Sensitivitätsexperimente und Zeitscheiben-Simulationen für das Klima des letzten Hochglazials (Last Glacial Maximum, LGM), des Heinrich-Stadials 1 und des mittleren Holozäns durchgeführt, um die Randbedingungen mit dem stärksten Einfluss auf die Isotopenzusammensetzung der Niederschläge zu identifizieren und die Verteilung der Wasserisotope während dieser Zeitintervalle zu reproduzieren. Für die Durchführung der Experimente wurde das numerische Klimamodell IsoCAM des National Center for Atmospheric Research (NCAR, Boulder, Colorado, USA) eingesetzt. Dieses Modell geht auf das Community Atmosphere Model (CAM3.0) zurück und enthält ein Wasserisotopenmodul.

Im ersten Teil dieser Arbeit lag der Schwerpunkt auf dem Verständnis der Sauerstoffisotopenverteilung in den Niederschlägen ($\delta^{18}O_{precip}$) zur Zeit des LGM. Ziel war es, die Unterschiede zum Kontrollklima den Einflüssen zuzuordnen, die die verschiedenen Randbedingungen ausübten. Die Ergebnisse einer vorindustriellen Kontrollsimulation wurden mit Experimenten verglichen, in denen die individuellen Einflussfaktoren – die Treibhausgaskonzentrationen, die Albedo und Topographie des Inlandeises, die Meeresoberflächentemperatur (Sea-Surface Temperature, SST) und die Parameter der Erdumlaufbahn – einzeln auf ihre LGM-Werte geändert wurden, um

ihren individuellen Einfluss abzuschätzen.

Die Ergebnisse zeigen, dass die SST und die Inlandeistopographie zur Zeit des LGM für den größten Teil der simulierten Änderungen im Klima und damit auch in der Sauerstoffisotopenverteilung in den Niederschlägen verantwortlich waren. Neben einer detaillierten Analyse der saisonalen und jährlichen Schwankungen der $\delta^{18}O_{\text{precip}}$-Werte in der Kontrollsimulation und einer Simulation, die alle LGM-Randbedingungen kombinierte, wurden die Steigungen in den räumlichen und zeitlichen Beziehungen zwischen $\delta^{18}O_{\text{precip}}$ und der Oberflächentemperatur für Grönland und die Antarktis berechnet und mit Rekonstruktionen aus Eisbohrkernen und den Ergebnissen anderer Isotopenmodelle verglichen.

Für den zweiten Teil der Arbeit wurden vier verschiedene Zeitscheiben-Simulationen durchgeführt, um die Verteilung der Wasserisotope auf dem afrikanischen Kontinent im vorindustriellen Klima sowie während des mittleren Holozäns, des LGM und des Heinrich-Stadials 1 zu analysieren. Insbesondere wurden die örtlichen und überörtlichen Einflüsse auf die Isotopenzusammensetzung der Wasserstoffisotope in den Niederschlägen (δD_{precip}) untersucht. Neben den Auswirkungen der Änderungen in der großskaligen Zirkulation unterstreichen die Ergebnisse besonders die große Bedeutung der Konvektion und des Ausregnens auf die (δD_{precip})–Verteilung in den Tropen. Zusätzlich wurden die simulierten (δD_{precip})-Werte für diese Zeitintervalle mit δD_{wax}-Daten verglichen, die aus der Analyse der isotopischen Zusammensetzung von n-Alkanen gewonnen wurden, die ursprünglich aus der Wachsschicht von Pflanzenblättern stammten. Die Paläodaten und die Modellergebnisse zeigten eine gute qualitative Übereinstimmung.

Im dritten Teil dieser Arbeit wurde die Verteilung der Isotope in den Niederschlägen und im Wasserdampf unter den gegenwärtigen Randbedingungen simuliert und mit Beobachtungen verglichen. Messungen der Isotopenzusammensetzung des Wasserdampfs haben gegenüber Messungen der Isotopenzusammensetzung der atmo-

sphärischen Niederschläge den Vorteil, dass die Beobachtungen ganzjährig möglich sind und auch in Trockengebieten durchgeführt werden können, in denen es nur selten zu Niederschlagsereignissen kommt. Zusammenfassend zeigt dieser Teil der Arbeit die grundsätzliche Verlässlichkeit der Ergebnisse, er deckt aber auch einige Mängel des Modells auf, die auf Schwachstellen in der Darstellung der Hydrologie der Landoberfläche und einer allzu stark vereinfachenden Behandlung der Wasserisotope in den Wolken zurückzuführen sind.

Chapter I

Introduction

1.1 Introduction

1.2 Stable water isotopes - general introduction

Isotopes are atoms of the same chemical element with different atomic mass due to the presence of different number of neutrons in its nucleus. For the water molecule, three stable isotopes of oxygen and two for hydrogen constitute different isotopologues such as $H_2^{18}O$, $H_2^{16}O$ and HDO. The relative abundance of the heavy with respect to the light isotope in a sample is denoted by isotope ratio R, which is D/H for the hydrogen isotope and $^{18}O/^{16}O$ for the oxygen isotope. The stable isotope composition of water is stated with reference to the standard isotopic ratio of Vienna Standard Mean Ocean Water (VSMOW), and is expressed as the normalized difference between the measured and VSMOW isotope ratios, with the δ notation ($\delta^{18}O$ for the oxygen isotope composition and δD for the hydrogen isotope composition) reported in units of permil (‰, parts per thousand) (Sharp, 2007). The absolute $^{18}O/^{16}O$ ratio of the VSMOW is 2005.20×10^{-6}, while the D/H ratio for the VSMOW is 155.95×10^{-6} (Araguás-Araguás et al., 2000). For instance, the oxygen isotope composition of a

sample is given by

$$\delta^{18}O=(R_{\text{SAMPLE}}/R_{\text{VSMOW}}-1) \times 1000\text{‰},$$

where R_{SAMPLE} and R_{VSMOW} are the isotopic concentrations of the sample and of VSMOW, respectively.

1.2.1 Isotope Fractionation

The observed variations of deuterium and ^{18}O content in the global water cycle are associated with the isotope fractionation occurring during the phase changes of the water molecule (during evaporation and condensation) due to the different saturation vapor pressure of the isotopic species. The lighter molecule gets evaporated preferentially as the vapor pressures of the lighter molecule is higher than the heavier molecule, whereas during condensation the heavier molecule preferentially condensates, thereby bringing changes in the isotopic composition of the remaining water vapor and of the source.

Based on the process that causes the change of isotopic abundance in a sample, the mass-dependent fractionation is distinguished as equilibrium, kinetic and transport fractionation (Gat, 2010). The fractionation (under equilibrium conditions) is represented with the isotope equilibrium fractionation factor α, the ratio of saturation vapor pressures of the isotopes. Between two substances A and B it is defined as

$$\alpha_{B/A} = R_B/R_A, \tag{1.1}$$

where R_A and R_B are the ratio of the heavy to light isotope in A and B respectively. As the vapor pressure is dependent on the temperature, α is also dependent on the ambient temperature with the fractionation increasing with lower temperatures. For temperatures below 100°C, Majoube (1971) calculated the equilibrium fractionation

factors between liquid-vapor and solid-vapor phase changes. The α values for the isotopologues HDO and $H_2^{18}O$ are given below (from Majoube, 1971 and Merlivat and Nief, 1967).

For HDO, the equilibrium fractionation factor between vapor and liquid is

$$\ln \alpha = \frac{24.844}{T^2} \times 10^3 - \frac{76.248}{T} + 52.612 \times 10^{-3}, \tag{1.2}$$

and for vapor to ice

$$\ln \alpha = \frac{16288}{T^2} 9.34 \times 10^{-2}. \tag{1.3}$$

For $H_2^{18}O$, the equilibrium fractionation factor between vapor and liquid is

$$\ln \alpha = \frac{1.137}{T^2} \times 10^3 - \frac{0.4156}{T} - 2.0667 \times 10^{-3}, \tag{1.4}$$

and for vapor to ice

$$\ln \alpha = \frac{11.839}{T^2} 2.8224 \times 10^{-2}, \tag{1.5}$$

where T is the absolute ambient temperature in K. Since the ratio of the molecular diffusivities for both the HDO and $H_2^{18}O$ are nearly the same, the kinetic effects for both isotopologues are similar. However, the equilibrium fractionation for HDO is approximately eight times greater than for $H_2^{18}O$, giving rise to the global Meteoric Water Line (Craig, 1961).

A widely used model of fractionation is the Rayleigh distillation model that applies to an open equilibrium system from which material is removed continuously with a constant fractionation factor (Gat, 2010). For instance, for precipitation of liquid water from water vapor, the evolution of the isotopic composition is described by a Rayleigh equation with fractionation factor α as:

$$R_f = R_i . F^{\alpha-1}, \tag{1.6}$$

where R_i and R_f are the initial and final isotopic ratios of the heavier to the lighter isotope, respectively. Furthermore, α is the fractionation factor between liquid and vapor, and F is the fraction of the water vapor remaining.

1.2.2 Evaporation and condensation

During evaporation of water into unsaturated air, the fractionation process is different from the equilibrium fractionation (where the fractionation depends only on the vapor pressures of the different isotopes). In addition, it is influenced by the different rates of molecular diffusivity of the isotopes of water ("kinetic effects"). The kinetic fractionation factor α_k is a function of sea surface temperature, the relative humidity of the air masses formed and the near surface winds (Stewart, 1975; Merlivat and Jouzel, 1979). Craig and Gordon (1965) provided a model for isotope fractionation during evaporation based on the Langmuir linear resistance model, and was widely used in the atmospheric models to estimate the fractionation during evaporation. The model assumes an equilibrium condition at the air/water interface and no divergence or convergence in the vertical air column and no isotopic fractionation during the evaporative transport of water molecules by a fully turbulent transport (cf. Horita et al., 2008; Luz et al., 2009; Gat, 2010). Based on the Craig-Gordon model, the isotopic composition of evaporative flux is defined by, from Horita et al., 2008,

$$\delta_E = \frac{\alpha_{V/L}\delta_L - h\delta_A - (\varepsilon^* + \varepsilon_K)}{(1 - h) + 10^{-3}\,\varepsilon_K} \tag{1.7}$$

where δ_E, δ_L, δ_A are the isotopic compositions of evaporating vapor, liquid water, and the water vapor, respectively. $\alpha_{V/L}$ is the fractionation factor between water vapor and liquid water and ε^* is given by $(1 - \alpha_{V/L}) \times 10^3$. The value ε_K represents a kinetic isotope effect that arises from the transport of water vapor through the three layers explained in the model. h is the relative humidity of the ambient atmosphere.

Condensation of water vapor is rather considered as an equilibrium process as the condensed phase is assumed to be in isotopic equilibrium with the surrounding vapor and to be removed immediately from the parcel. So, the process is adequately described by a Rayleigh process when the rainout determines atmospheric moisture budget (Dansgaard, 1964; Gat, 2010).
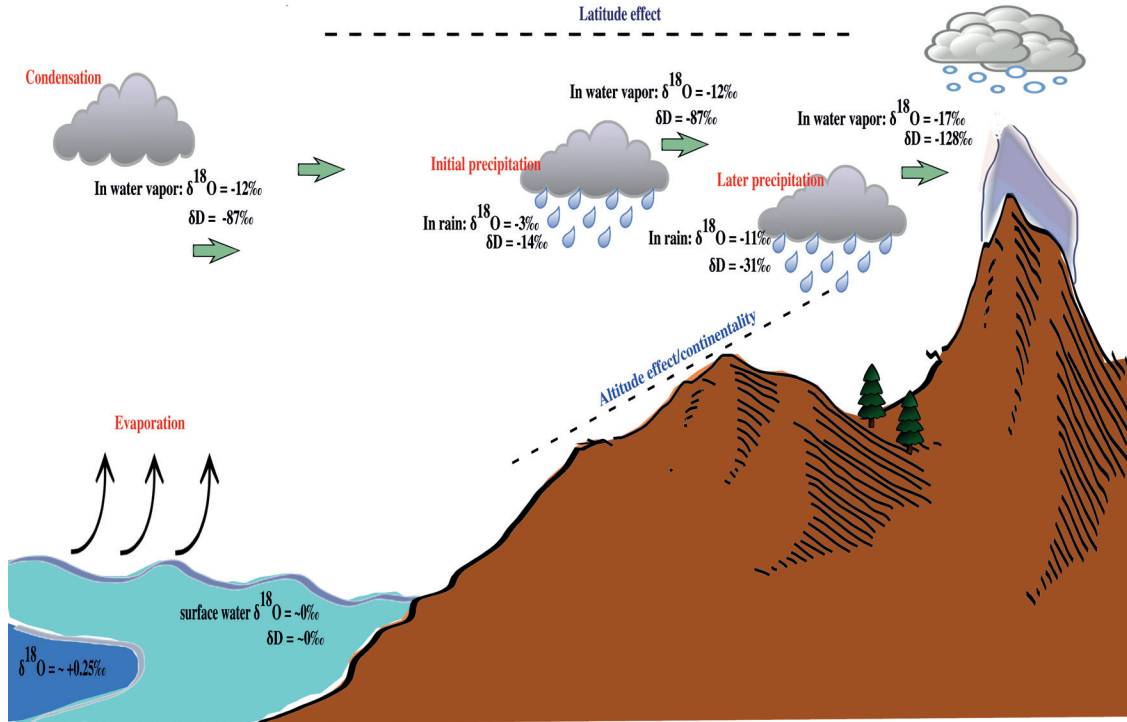
Figure 1.1: Schematic representation of isotopes in the hydrological cycle with idealized values of isotopic composition of the oxygen (δ^{18}O) and hydrogen (δD).

1.3 Spatial distribution of isotopes in precipitation

Studies like Dansgaard (1964) and Rozanski et al. (1993) based on the observational data from the Global Network of Isotopes in Precipitation (GNIP) suggest that the isotopic composition of local precipitation integrates the entire travel history of precipitating air masses. Such environmental conditions include the evaporation from the ocean, the mutual relation between precipitation and evapotranspiration (Rozanski

et al., 1993) along the distance to the precipitation site, and the possible mixing with other air masses. Other studies for example, Araguás-Araguás et al. (2000) confirm the empirical relationship of the observed composition of isotopes in precipitation to the environmental parameters. Following these studies, the observed effects and the factors controlling the isotopic composition of precipitation are discussed in the paragraphs below. A schematic representation of the isotopes in hydrological cycle is given in Figure 1.1.

Temperature effect

Dansgaard (1964) found that the isotopic composition of precipitation in temperate climates is positively correlated with the surface temperature. Later studies using the GNIP data (Rozanski et al., 1993; Araguás-Araguás et al., 2000) proved this relation in the high latitudes, which is explained based on a Rayleigh distillation model. The fractionation during condensation increases with decreasing temperature, thereby reducing the ratio of heavier isotopes in the remaining vapor. According to Sharp (2007) however, rather than the increase in fractionation at colder temperatures, it is the strength of the rainout that causes the temperature effect. Below 14°C, the global relationship of $\delta^{18}O$ in precipitation ($\delta^{18}O_{precip}$) and δD in precipitation (δD_{precip}) to mean temperature (T) in °C is given by

$$\delta^{18}O_{precip}=0.69T-13.6‰ \tag{1.8}$$

and

$$\delta D_{precip}=5.6T-100‰. \tag{1.9}$$

The "latitude effect " observed in the isotopes in precipitation is similar to the temperature effect and represents the decrease of δ values with increasing latitude,

due to the lower temperatures and increasing degree of rainouts.

Altitude effect

The heavy isotope contents of rainwater decreases with increasing altitude, which is attributed to the progressive condensation of atmospheric water vapor and rainout when the air masses climb up along the slopes of high mountains and cool off as a consequence of adiabatic expansion. The amount of water vapor in the airmass decreases rapidly with the increase in relief, and the remaining water vapor becomes progressively depleted in heavy isotopes. From the isotopic records throughout many of the world's mountain belts, Poage and Chamberlain (2001) find that the oxygen and hydrogen isotopic composition of precipitation decreases linearly with increasing elevation in most regions of the world except in the Himalayas and for elevations >5000 m. They estimated an isotopic lapse rate of $\approx 0.28‰/100$ m for $\delta^{18}O$ over most regions of the world except at the extreme latitudes where isotopic lapse rates are higher. In addition, Gonfiantini et al. (2001) recognize that the parameters that affect the isotope composition in precipitation-altitude relationships are the vertical gradient of the temperature lapse rate and the initial relative humidity of the ascending air mass.

Amount effect

"Amount effect" is the inverse relationship of the δ values to the precipitation amount (Dansgaard, 1964). Highly depleted (in heavy isotopes) stable isotope concentrations are observed during time periods of intense precipitation (Rozanski et al., 1993) over the convectively active regions in the tropics. Vuille et al. (2003) suggest that the amount effect is caused by the small-scale vertical convection associated with precipitation in the tropics. As condensation proceeds, heavier isotopes are preferentially removed and the relative abundance of the heavier isotopes in the water vapor de-

creases. The isotopic composition of the rainfall thus gets depleted with the increased convective nature of the rainfall. This effect can be amplified by the fact that isotopic exchange with water vapor and evaporative enrichment of raindrops are both greatly reduced with heavy rains (Dansgaard, 1964). Contrary to Vuille et al. (2003), Risi et al. (2008a) conclude that the predominant processes leading to the amount effect in the tropics are related to the fall and reevaporation of precipitation, rather than processes occurring during the ascent of air parcels. They further find that the fractionation process during rain fall contributes the most to the amount effect in regimes of weak precipitation, and the injection of vapor from the unsaturated downdraft is predominant in regimes of strong precipitation.

Continentality

Continentality, also referred to as the distance-from-coast effect, is the progressive depletion of the heavier isotopes in precipitation with increasing distance from the ocean (source of water vapor) and varies considerably with different seasons and topography of the regions (Rozanski et al., 1993). Sharp (2007) adds that the continentality effect is associated mainly with the temperature decrease between the source of atmospheric vapor and the point of precipitation so that the effect is greater during the winter season.

Seasonality

Isotopic seasonality refers to the differences in the stable isotopic composition of precipitation between the summer and winter of the respective hemispheres. Rozanski et al. (1993) found that the mid- and high-latitude stations of the GNIP data have high δ values during the summer and low δ values during the winter. The seasonality arises mainly due to the seasonal changes in temperature, which causes seasonal variations in the amount of precipitable water and rainout via a Rayleigh process. Seasonal

variations in the evapotranspiration flux over the continents and the source regions and transport pathways also contribute to the isotopic seasonality. For example, in the Asian monsoon region, studies have found a reverse isotopic seasonality with lower precipitation $\delta^{18}O_{\text{precip}}$ values during the summer monsoon despite warmer temperatures (Araguás-Araguás et al., 1998; Johnson and Ingram, 2004) and is suggested to be related to the strength of the monsoon (Vuille et al., 2005).

Feng et al. (2009) suggested that the dominant mechanism controlling seasonality of $\delta^{18}O_{\text{precip}}$ is the north-south migration of the meridional convective circulation cells and the corresponding systematic shifts in the latitudinal positions of the subtropical highs. Their study finds that separation of the high and low-latitude zones happens around 30°S and 30°N, which are the mean boundaries between the tropical Hadley cells and the subtropical Ferrel cells.

1.3.1 Distribution of isotopes in water vapor

Stable isotopic composition of water vapor provides information on the source of atmospheric moisture, water vapor transport, mixing and fractionation (Rozanski and Sonntag, 1982; White and Gedzelman, 1984; Lawrence et al., 2004). Vertical sampling of the deuterium composition of the tropospheric water vapor by Taylor (1972) documented a general decrease of heavy isotope values with altitude in the lower and mid troposphere and a high positive correlation between the isotopic ratios and the specific humidity of the air. Rozanski and Sonntag (1982) using a one dimensional model suggest that a complete isotope exchange of the falling raindrops with the water vapor and cloud water at various atmospheric levels could explain the steep deuterium profiles observed. Likewise, studies (for example, Worden et al., 2007; Brown et al., 2008; Risi et al., 2008b; Field et al., 2010) suggest that the effects of mixing of the airmasses, evaporation of condensate and precipitation, isotopic exchange of water vapor with precipitation, and continental recycling introduce more

isotopic variability in the atmospheric water than that predicted by Rayleigh models. Likewise, recent studies using general circulation models also reveal that the cloud microphysical processes such as the nature of the phase change, the retention of cloud droplets in the cloud, and interactions between the vapor and raindrops falling from above also affect the isotopic composition of the vapor (Lee and Fung, 2008; Risi et al., 2008a). In addition, Stewart (1975) finds that partial re-evaporation of the raindrops falling into unsaturated air enriches the raindrop, but leads to depletion of surrounding vapor in heavy isotopes. Similar to this, Risi et al. (2008b) suggest that the partial re-equilibration of the rain drop with the surrounding vapor through diffusive exchanges or re-evaporation leads to variations in the composition of the low-level vapor, and can be transmitted to the isotopic composition of precipitation.

Using a general circulation model (GCM), Wright et al. (2009) find that the isotopic signature of free tropospheric water vapor in the tropics and subtropics is largely determined by the processes within convective clouds and by the evaporation of condensate formed within convective clouds. Risi et al. (2008b) make an associated finding that convection has a strong impact on the isotopic composition of the water vapor and precipitation. Similarly, Field et al. (2010) studied the effect of non-Rayleigh-postcondensation exchange on the isotopic composition of water in the atmosphere and find that the process depletes water vapor. They further find that during heavy rainfall events, post condensation exchange tends to deplete vapor and precipitation of heavy isotopes via atmospheric moisture recycling. Brown et al. (2008) recognize the importance of rainfall recycling that occurs locally over the Amazon basin to produce the anomalously low isotope values during the wet season.

More recently, the measurements of atmospheric water columns using satellites, for instance, data from the Tropospheric Emission Spectrometer (TES, Worden et al., 2007) and Scanning Imaging Absorption Spectrometer for Atmospheric Cartography (SCIAMACHY, Frankenberg et al., 2009) provide a a more comprehensive view of

vertical water transport throughout the troposphere. These data highlight the importance of the large scale circulation including subsiding branch of Hadley-cell circulation on the isotope distribution in vapor (Frankenberg et al., 2009) and the rainfall evaporation (Worden et al., 2007) on the isotopic composition of the water vapor.

1.4   Isotopes as a proxy for past climate changes

Stable isotope-based paleoclimate reconstructions are founded on the assumption that the mean $\delta^{18}O$ and δD values of precipitation are related to the ambient temperature, especially in the high latitudes where the precipitation forms near to the surface (Sharp, 2007). Dansgaard (1964) recognized that at low temperatures $\delta^{18}O_{precip}$ is strongly correlated with the local surface temperature ("temperature effect", Dansgaard, 1964; Rozanski et al., 1993) and for temperatures below 14°C, the annual-mean $\delta^{18}O_{precip}$ is closely related to the annual-mean surface temperature T as given in Equation 1.8 (and Equation 1.9 for hydrogen).

The $\delta^{18}O_{precip}$ record from the first deep core drilled in 1966 at Camp Century (northwestern Greenland; Ueda and Garfield, 1968; Johnsen et al., 1972) gave evidences for the large variability of climate during the last glacial period in Greenland, as summarized in Johnsen et al. (2001). The $\delta^{18}O$ record showed a 14% shift between the glacial to interglacial in the Camp Century core and the extremely cold glacial period was marked by many warm events, the so-called Dansgaard-Oeschger cycles (cf. Rozanski et al., 1997). These results were later confirmed with the ice core records from Dome-C and Vostok stations in Antarctica (Lorius et al., 1985; Stenni et al., 2004; Barbante et al., 2006).

Marine oxygen isotope proxy records preserved in fossil carbonate shells of planktonic or benthic foraminifers ($\delta^{18}O_c$) deposited in ocean sediments depend on the temperature of calcification and the ratio of oxygen isotopes of the ambient seawater

($\delta^{18}O_w$, Bijma et al., 1999), where $\delta^{18}O_w$ is influenced by variations in the hydrological cycle, i.e, the local precipitation-evaporation balance as well as the continental ice volume (Wefer et al., 1999). For instance, paleoceanographic studies use the differences in the $\delta^{18}O_c$ values of shallow-living and deep-living planktonic foraminifera as a proxy for the thermal stratification of surface waters (Mulitza et al., 1997; Niebler et al., 1999; Mulitza et al., 2003). On the other hand, oxygen isotope ratios recorded in the benthic foraminiferal carbonate are utilized as a proxy for bottom-water conditions (Lynch-Stieglitz, 2003), or are interpreted to reflect global ice-volume changes (Shackleton and Opdyke, 1973; Mackensen et al., 1989; Mackensen and Bickert, 1999), if circulation-induced fluctuations in the temperature and salinity of the oceanic bottom waters are negligible.

Apart from the ice-core records and marine stable water isotope records, it has been shown that the compound-specific stable hydrogen isotope composition of sedimentary n-alkanes (originating from the epicuticular wax layer of terrestrial plants) can be used for reconstructing past changes in tropical hydrological cycle (Sauer et al., 2001; Schefuß et al., 2005; Collins et al., 2011; Tierney et al., 2011a; Schefuß et al., 2011; Collins et al., 2013). The principle behind is that the plant waxes get enriched in deuterium with increased evapo-transpiration, also the soil water gets enriched with the heavier isotope under arid conditions. Thus, the δD values derived from plant waxes (δD_{wax}) correspond to the evaporation-precipitation balance and can be used as a proxy for past changes in the hydrological cycle.

1.5 Modeling the water isotopes

In order to explain the spatial and temporal variability of isotopes in precipitation, Jouzel and Merlivat (1984) developed the first model of isotopic composition of atmospheric moisture in terms of the progressive loss of heavy isotopes through frac-

tionation based on Rayleigh's distillation process. Rayleigh models have simplified atmospheric hydrology, thereby, they are unable to account for the complexity of processes in the atmosphere like mixing of air masses or the variable trajectories of the vapor transport (Yoshimura et al., 2003). These models were successful in explaining the temperature effect in high latitudes, but were insufficient to explain the variability of isotopes in precipitation due to the absence of air mass mixing, post-condensation exchange, and evaporative recharge of the isotopes (Hoffmann et al., 2000).

For a better representation of the hydrological cycle and the above-mentioned processes, efforts have been made to fit isotope modules to general circulation models. Stable water isotopes have been included in the hydrological cycle of various global atmospheric models, namely, GISS (Jouzel et al., 1987), ECHAM (Hoffmann et al., 1998), MUGCM (Noone and Simmonds, 2002), CAM2.0 (Lee et al., 2007), LMDZ (Bony et al., 2008), CAM3.0 (Sturm et al., 2010); ocean general circulation models, namely, MOM - version 2 (Paul et al., 1999), GISS ocean general circulation model (Schmidt, 1998) and the atmosphere-ocean coupled models HadCM3 (Tindall et al., 2009) and GISS ModelE-R (LeGrande and Schmidt, 2009). These models have been successfully used for simulating the present and past distributions of the stable isotopes in the global hydrological cycle. A description of these isotope enabled GCMs and model versions are provided in Noone and Sturm (2010).

1.6 Objective and research questions of this study

The main objective of this study is to simulate the distribution of water isotopes during the past climates, and to understand the climate factors that lead to the variabilities in the distribution of the water isotopes through these paleo-simulations. The study addresses the changes in the relationship between the climate variables and the isotopes in precipitation, which is a critical metric for paleothermometry/past

precipitation reconstructions. An atmospheric model equipped with water isotopes tracers in its hydrological cycle is used for the simulations and the following research questions are addressed in this thesis with the climate-model simulations of both past time periods and present-day.

- What are the boundary conditions and climate factors that influence the glacial isotope distribution, and does the δ^{18}O - temperature relationship hold through different climate states?

  The glacial climate is very different from the present-day climate and the Last Glacial Maximum (LGM, 21 ka) boundary conditions are sufficiently well known. From a series of sensitivity experiments explained in Chapter 3 we try to distinguish the boundary conditions and the climate factors that caused maximum variability in the δ^{18}O$_{precip}$ during the LGM. The study also investigates the changes in the spatial and temporal slopes between the climates that has implications for the temperature reconstructions.

- How does the isotopic distribution over the tropics change with the local and remote changes in the climate during the past? Can the comparison between the reconstructed leaf-wax isotope proxy data over Africa, and modeled δD values ascertain the skills of the model to simulate the past isotope distributions with climates, that differ starkly from the present?

  In contrast to the higher latitudes where the "temperature effect" plays the dominant role in determining the isotopic composition of the precipitation, in the tropics, the isotope distribution in precipitation is more related to the amount of precipitation, where most of the precipitation arises from convective processes that strongly affect the isotopic composition of both water vapor and precipitation (Bony et al., 2008; Risi et al., 2008a). The study investigates whether it is possible to distinguish these effects from the δD$_{precip}$ anomalies. The results are

compared with the hydrogen isotope composition of leaf-wax recorded in the sediment cores for the corresponding time periods, as it will be advantageous to understand whether the model and proxy data record similar climate events of the past.

- How well does the model simulate the present-day distribution of the isotopes in precipitation and the isotopes in water vapor and what are the possible causes of the discrepancies between the model and observations? Validation of the model results with the present-day observations is important to determine the skills and deficiencies of the model and to assess the implications on the proxy data reconstructions. For this, present-day model results are compared with observations of isotopes in water vapor and in precipitation.

1.6.1 Outline of the Thesis

The numerical model used for carrying out the experiments is described in Chapter 2. The results are presented in three manuscripts in Chapter 3, Chapter 4 and Chapter 5, respectively.

- **Chapter 3 : Influence of Last Glacial Maximum boundary conditions on the global water isotope distribution in an atmospheric general circulation model.**

  T. Tharammal, A. Paul, U. Merkel and D. Noone (published in *Climate of the Past*, doi:10.5194/cp-9-789-2013).

  The study intents to understand the validity of $\delta^{18}O$ proxy records as indicators of past temperature change and to analyze the spatial variations of the oxygen isotopic composition in response to individual climate factors. For this, a series of experiments was conducted to test the influence of individual boundary con-

ditions during the LGM (greenhouse gases, ice-sheet albedo and topography, sea-surface temperature, and orbital parameters) on the $\delta^{18}O_{precip}$.

- **Chapter 4: Hydrogen isotopes of meteoric water in Africa: Modeling and comparison to data.**

  T. Tharammal, A. Paul, J. Collins, U. Merkel and S. Mulitza (submitted to *Quaternary Science Reviews*).

  In this study, the water isotope distribution over the African continent during three past time periods (mid-Holocene, Heinrich Stadial-1, the LGM) is analyzed. Model results for δD_{precip} for these time periods are compared with the data obtained from the stable hydrogen isotope composition of plant leaf-wax *n*-alkanes (Collins et al., 2013).

- **Chapter 5: Stable isotopes of water in an atmospheric model: Major features and model evaluation with observations.**

  T. Tharammal, K. Weigel, A. Paul, D. Noone and R. A. Scheepmaker (in preparation for *Geoscientific Model Development*).

  Model results from a present-day simulation are validated against the observations to assess the model performance quantitatively, and to recognize the aspects to be improved in simulating the isotope distribution in both water vapor and precipitation. Model results for the isotopes in precipitation are compared against available observations from the Global Network of Isotopes in Precipitation (GNIP). The simulated isotopic composition of water vapor is compared with total column averaged δD data from the Scanning Imaging Absorption Spectrometer for Atmospheric Cartography (SCIAMACHY).

Chapter 6 includes the discussion and conclusion of the thesis. In addition, Chapter 6 includes an outlook on modeling of water isotopes and suggestions for future research.

Chapter II

Methodology

2.1 The Model

The NCAR Community Atmosphere Model CAM3.0 (Collins et al., 2004, 2006), fitted with a water isotope module (referred as IsoCAM) in its hydrological cycle is used to carry out the climate simulations in the study. The spatial resolution employed in our experiments corresponds to a spectral truncation of T31 and 26 hybrid levels in the vertical. The related Gaussian grid has a spatial resolution of approximately 3.75°(48 grid points in latitude and 96 grid points in longitude). The ability of CAM3.0 to efficiently simulate the global hydrological cycle is detailed in Hack et al. (2006).

2.1.1 Brief overview of model physics formulations

The model physics parameterizations in CAM3.0 consists of a sequence of components, i.e. precipitation, clouds and radiation, surface model, and turbulent mixing, which are further subdivided into various subcomponents. A detailed description of the model physics is given in Collins et al. (2004). The process of deep convection in the CAM3.0 is treated with the parametrization scheme developed by Zhang and McFarlane (1995), and shallow convection is parameterized using the Hack scheme (Hack, 1994). In this formulation, moist convection occurs only when there is con-

vective available potential energy (CAPE). Convective precipitation can evaporate into its environment following Sundqvist (1988), and enhancement of atmospheric moisture through this mechanism was offset by drying, introduced by changes in the longwave absorptivity and emissivity (Collins et al., 2004).

Cloud fraction (cloud amount) in the model depends on relative humidity, atmospheric stability and convective mass fluxes, and the diagnosis of cloud fraction in the model is a generalization of the scheme by Slingo (1987), modified as in Kiehl et al. (1998). Three types of cloud – low-level marine stratus, convective cloud, and layered cloud – are diagnosed by the scheme. More details of the cloud-type diagnosis are given in Collins et al. (2004).

The method of Berger (1978) is used to calculate insolation, and this formulation could be used to determine the insolation for any time within 10^6 years of 1950 AD, thereby enabling the use of the model for paleoclimate simulations.

2.1.1.1 Land, ice and ocean interactions

CAM is coupled to the Community Land Model, CLM (Bonan et al., 2002), which uses the same grid as the atmospheric model. CLM includes different forms of land surface types within each grid cell, namely lakes, glaciers, wetlands and up to 16 land plant functional types (PFTs) that can include a bare soil (Dickinson et al., 2006). The land and atmosphere models are coupled with a fully explicit time stepping procedure, and the current state of the atmosphere is used to force the land model. Monin-Obukhov similarity theory applied to the surface (constant flux) layer is used to calculate the land surface fluxes of momentum, sensible heat, and latent heat (Collins et al., 2004). Surface energy, constituent, momentum and radiative fluxes (latent heat flux, sensible heat flux) from the land model are then used to update the atmosphere (Bonan, 1996).

A thermodynamic sea-ice model (CSIM) represents the sea-ice component of the

model. CSIM computes the surface fluxes when used with prescribed SST (Briegleb et al., 2002). It further predicts snow depth, brine pockets, internal shortwave radiative transfer, surface albedo, ice-atmosphere drag and surface exchange fluxes without the use of a flux coupler (Collins et al., 2006). For uncoupled integrations, snow depth on sea ice is prognostic as snow accumulates when precipitation falls as snow, and it melts when allowed by the surface energy balance. The maximum snow depth is fixed at 0.5 m for the stand-alone CAM3.0. Sea ice or snow on sea ice are not effected by rain in the model (Collins et al., 2004). Atmospheric state variables and downwelling fluxes along with surface state variables, and surface properties are used to compute atmosphere-ice shortwave and longwave fluxes, wind stress, sensible and latent heat fluxes. The bulk formulas used are based on Monin-Obukhov similarity theory. Surface state variables are temperature and albedos, which, in turn depend on spectral band, snow thickness, ice thickness and surface temperature. Surface properties are longwave emissivity and aerodynamic roughness. Additionally, certain flux temperature derivatives required for the ice temperature calculation are computed, as well as a reference diagnostic surface air temperature (Collins et al., 2004).

For the ocean, the turbulent fluxes of momentum (stress), water (evaporation/latent heat), and sensible heat into the atmosphere over ocean surfaces are determined using bulk formulas as, from Collins et al. (2004):

$$(\tau, E, H) = \rho_A |\Delta\vartheta|(C_D\Delta\vartheta, C_E\Delta q, C_p C_H \Delta\theta), \tag{2.1}$$

where ρ_A is atmospheric surface density and C_p is the specific heat. Since CAM3.0 does not allow for motion of the ocean surface, the velocity difference between surface and atmosphere is $\Delta\vartheta = \vartheta_A$, the velocity of the lowest model level. The potential temperature difference is $\Delta\theta = \theta_A\text{-}T_S$, where T_S is the surface temperature and, q_a and θ_A are the lowest level atmospheric humidity and potential temperature. The

specific humidity difference is $\Delta q = q_a\text{-}q_s\,(T_S)$, where $q_s\,(T_S)$ is the saturation specific humidity at the sea-surface temperature.

2.1.1.2 Initial and boundary conditions

In CAM3.0 each atmospheric grid box is partitioned into three surface types: land, sea ice, and ocean. Land fraction is assigned at model initialization and is considered fixed throughout the model run. Ice concentration data is provided by the external time varying dataset along with the SST dataset, with new values determined by linear interpolation at the beginning of every time-step. Any remaining fraction of a grid box not already partitioned into land or ice is regarded as ocean (Collins et al., 2004). Surface fluxes are then calculated separately for each surface type, weighted by the appropriate fractional area, and then summed to provide a mean value for a grid box (Collins et al., 2004). For each time-step, the aggregated grid box fluxes are passed to the atmosphere and all flux arrays which have been used for the accumulations are reset to zero in preparation for the next time-step. A detailed description of the initial and boundary datasets is given in (McCaa et al., 2004).

2.1.2 Isotope module

IsoCAM is based on an earlier isotopic scheme by Noone and Simmonds (2002), but includes a more sophisticated treatment of surface exchange and cloud processes to make use of the multiple water phases predicted by CAM (Noone, 2003, 2006; Noone and Sturm, 2010; Sturm et al., 2010). The stable isotope ratios of water in the hydrological cycle of IsoCAM are transported through the atmosphere and the ground by the same processes (advection, moist convection, evapo-transpiration etc.) used to transport normal water (Sturm et al., 2010). Isotopic fractionation occurs with every phase change of the water species in the model hydrology. IsoCAM employs a semi-Lagrangian formulation for the water vapor and tracer transport (Williamson and

Rasch, 1994; Williamson and Olson, 1994). This formulation uses a shape-preserving interpolation method (Williamson and Rasch, 1989), which avoids the generation of spurious minima or maxima through supersaturation by the transport of water vapor (Williamson and Olson, 1994). The scheme has been found to be sufficiently accurate for conserving isotopic ratios during advection to low-temperature environments (Noone and Simmonds, 2002; Noone and Sturm, 2010), however, it does not guarantee mass conservation (Staniforth and Côté, 1991; Rasch and Williamson, 1990; Williamson and Olson, 1994; Williamson and Rasch, 1994). A "mass fixer" that repeatedly restores global mass is used in CAM3.0 to account for this imbalance (Collins et al., 2004). Studies with the MUGCM (Noone and Simmonds, 2002) find that the application of such a mass fixer leads to fictitious changes in the isotope distribution, as the mass restoration is not local and the mass is not balanced where the spurious sinks/sources have removed/added the mass, which affects especially the polar regions. The avoidance of mass-fixing causes an annual global energy imbalance at the top of the model (TOM) and the surface (cf. Table 3.5) in comparison with the high-resolution model simulations using CAM3.0 (Hack et al., 2006). The surface temperature and precipitation patterns in the simulations conducted were nearly identical to the fully-coupled Community Climate System Model (CCSM3.0). Since IsoCAM gives a better tracer-tracer correlation without the application of a posteriori mass fixer, our simulations were carried out without mass fixing.

2.1.2.1 Isotope fractionation

A description of isotopic fractionation during evaporation, condensation and post-condensation processes in the model is given in this section. The isotope module traces the water isotopes through each component of the model's hydrological cycle in parallel to normal water (H_2O) (Noone and Simmonds, 2002). During the phase change of water molecules, the stable isotopologues in consideration - HDO and H_2O^{18}

- are differentiated by the mass-dependent fractionation based on the mass mixing ratio. The fractionation coefficients are taken from empirically derived formulas, given by the Equations 1.2 to 1.5. The inclusion of fractionation processes is treated in the physical parameterizations of the model.

For the calculation of isotope ratios over land, a simple bucket model (Manabe, 1969) is used, which does not differentiate between evaporation and river runoff or different soil/vegetation types (Deardorff, 1977; Noone and Simmonds, 2002). Evaporation in the model occurs without fractionation and the isotopic ratio of the evaporated moisture is equal to that in the upper soil layer. Over ice, snow and frozen soil no fractionation during evaporation is assumed as the low diffusivity of the isotopic species in the solid phase prevents isotopic exchange (Noone and Simmonds, 2002).

The isotopic ratio of the ocean is set to be spatially uniform and for present-day conditions, a sea-surface enrichment of 0.5‰ for $\delta^{18}O$ and 4‰ for δD was applied (cf. Craig and Gordon, 1965; Hoffmann et al., 1998). Evaporation from the ocean surface is treated as equilibrium fractionation with a correction applied for the wind-dependent kinetic effects according to Merlivat and Jouzel (1979) (Equation 1.7). Evaporative fluxes of the isotopic species at the ocean surface are calculated similar to the normal water with a bulk formula as

$$E_i = \rho c \eta (R_s q_s - q_i), \tag{2.2}$$

where c is an exchange coefficient, q_s is the saturation mixing ratio at the source temperature T_s and ρ is the density of dry air. R_s is the isotopic composition of the source vapor and is equal to R_{ocean}/α_e, where α_e is the equilibrium fractionation factor that depends on the surface temperature and R_{ocean} is the isotopic ratio of the ocean surface water (Noone and Sturm, 2010). Diffusion of the different isotopes introduces kinetic fractionation and kinetic effects are accounted for as a function of

the turbulence strength, by the modification of the drag coefficient by the efficiency factor k_{mol} based on the study by Merlivat and Jouzel (1979).

The isotopic fractionation during condensation and post-condensation process is based on Noone and Simmonds (2002). Condensation into droplets or ice crystals is treated as an equilibrium fractionation process. For in-cloud large scale condensation, isotopic calculations follow the "Mixed Cloud Isotopic Model" by Ciais and Jouzel (1994), which facilitate mixed clouds into the Rayleigh-type model, thereby allowing supercooled liquid droplets and ice crystals to coexist between -15°C and -40°C (Noone and Simmonds, 2002). In the case of convective precipitation, Rayleigh distillation is assumed for solid condensate (temperatures less than -10°C) that will rapidly fall from the layer, whereas for the formation of liquid condensate, total equilibrium is assumed. For large scale or stratiform precipitation, equilibrium fractionation is assumed as the drop size is considered to be small, where the water vapor and condensate is in isotopic equilibrium before the condensate is removed. According to the findings of Hoffmann et al. (1998), 45% of the condensate is equilibrated to the surroundings in the case of convective precipitation which vastly consists of large drops, while 95% is equilibrated for the large scale stratiform precipitation with small drop size (Sturm et al., 2010). Kinetic effects are included for temperatures below -20°C for both large scale and convective precipitation and the effective fractionation factor is calculated following the parameterization of Jouzel et al. (1987). Kinetic effects are important for the reevaporation of the condensate falling below the cloud base, and the process is incorporated without fractionation in the case of reevaporation from ice, and with fractionation and kinetic effects for liquid precipitation (Noone and Simmonds, 2002). Kinetic effects are parameterized based on effective humidity following Stewart (1975) and Joussaume and Jouzel (1993).

2.2 Experimental set-up

To understand the effect of individual forcing factors on the $\delta^{18}O_{precip}$ distribution during the LGM, a series of sensitivity experiments were conducted. A pre-industrial simulation was performed as the control experiment, as well as a simulation with all the boundary conditions set to Last Glacial Maximum (LGM) values. Results from the pre-industrial and LGM simulations were compared to experiments in which the influence of individual boundary conditions (greenhouse gases, ice-sheet albedo and topography, sea-surface temperature, and orbital parameters) were changed each at a time to assess their individual impact. The spatial and temporal variations of $\delta^{18}O_{precip}$ were analyzed with respect to the changes in the mean climate variables, and results were compared with the proxy data from Greenland and Antarctica. The details of these sensitivity experiments are given in Chapter 3.

In order to study the past water isotope distribution over the African continent, four different time slice experiments - pre-industrial (PI, approximately 1800 AD), mid-Holocene (6 ka BP), LGM (21 ka BP) and Heinrich Stadial-1 (HS1, 16-18 ka BP) were conducted. Proxy evidences (Gasse, 2000 and references therein) suggest that compared to present-day the hydrological cycle over the continent during these time periods varied significantly. Model results for the hydrogen isotope composition of precipitation (δD_{precip}) for these time periods were compared with δD data obtained from the stable hydrogen isotope composition of plant leaf-wax n-alkanes (δD_{wax}, Collins et al., 2013). Extended descriptions of the model set-up and the δD_{wax} data are given in Chapter 4.

A present-day simulation with boundary conditions set according to the standard Atmospheric Model Intercomparison Project (AMIP, Gates et al., 1999) protocol was conducted to validate the model results against observations of isotopes in the water cycle. The model was forced with an observed sea surface temperature (SST)

climatology from the melded HadISST/Reynolds data for 1979-2001 (Hurrell et al., 2008). The model results for the isotopes in precipitation were compared against available observations from the Global Network of Isotopes in Precipitation (GNIP). The simulated isotopic composition of water vapor was compared with total column averaged HDO data from the Scanning Imaging Absorption Spectrometer for Atmospheric Cartography (SCIAMACHY, Frankenberg et al., 2009). Methodology and data used for the comparison are described in detail in Chapter 5. All simulations were carried out on the Linux cluster in the Geosystem Modeling Group of the Faculty of Geosciences/Fachbereich Geowissenschaften (FB5).

Chapter III

Influence of Last Glacial Maximum boundary conditions on the global water isotope distribution in an atmospheric general circulation model

T. Tharammal, A. Paul, U. Merkel and D. Noone

3.1   Abstract

To understand the validity of $\delta^{18}O$ proxy records as indicators of past temperature change, a series of experiments was conducted using an atmospheric general circulation model fitted with water isotope tracers (Community Atmosphere Model version 3.0, IsoCAM). A pre-industrial simulation was performed as the control experiment, as well as a simulation with all the boundary conditions set to Last Glacial Maximum (LGM) values. Results from the pre-industrial and LGM simulations were compared to experiments in which the influence of individual boundary conditions (greenhouse gases, ice-sheet albedo and topography, sea-surface temperature, and orbital parameters) were changed each at a time to assess their individual impact. The experiments were designed in order to analyze the spatial variations of the oxygen isotopic com-

position of precipitation ($\delta^{18}O_{\text{precip}}$) in response to individual climate factors. The change in topography (due to the change in land-ice cover) played a significant role in reducing the surface temperature and $\delta^{18}O_{\text{precip}}$ over North America. Exposed shelf areas and the ice sheet albedo reduced the Northern Hemisphere surface temperature and $\delta^{18}O_{\text{precip}}$ further. A global mean cooling of 4.1 °C was simulated with combined LGM boundary conditions compared to the control simulation, which was in agreement with previous experiments using the fully coupled Community Climate System Model (CCSM3). Large reductions in $\delta^{18}O_{\text{precip}}$ over the LGM ice sheets were strongly linked to the temperature decrease over them. The SST and ice-sheet topography changes were responsible for most of the changes in the climate and hence the $\delta^{18}O_{\text{precip}}$ distribution among the simulations.

3.2 Introduction

The Last Glacial Maximum (LGM, about 19,000-23,000 years before present) marks the peak of the last glacial period between about 110,000 and 10,000 years before present. A strong cooling in both hemispheres is recorded in proxy records from Greenland (Dahl-Jensen et al., 1998) and Antarctica (Stenni et al., 2004) (EPICA community members, 2004). During the LGM, a large portion of North America and northern Eurasia was covered by ice sheets, hence the sea level was reduced by about 120 m (Fairbanks, 1989; Lambeck and Chappell, 2001). The newly exposed land areas and differences in vegetation and soil type impacted the surface albedo. The Laurentide ice sheet covering most of Canada and a large portion of the northern United States had a first-order impact on the large-scale atmospheric circulation in the Northern Hemisphere via topographic and thermal forcing as demonstrated in global circulation models (e.g., Hansen et al., 1984; Manabe and Broccoli, 1985). A reduced atmospheric concentration of CO2 (185 ppmv, Petit et al., 1999) compared

to the pre-industrial (PI, approximately 1800 AD) value of 280 ppmv also influenced climate, as reduced greenhouse gas (GHG) levels have a direct effect on radiative forcing (Shin et al., 2002). Sensitivity studies using slab-ocean models (e.g., Manabe and Broccoli, 1985) find that the reduction in GHG is accountable for the global cooling during the LGM, whereas the ice sheets induce a regional cooling in the Northern Hemisphere. Hewitt and Mitchell (1997) and Kim (2004) using coupled atmosphere ocean-general circulation models similarly conclude that the ice-sheet topography is a dominant factor in reducing the surface temperature in the Northern Hemisphere. A recent sensitivity study by Pausata et al. (2011a) finds that the ice-sheet topography also plays a key role in altering the circulation pattern over the North Atlantic Ocean. These studies demonstrate the importance of studying the relative role of individual Last Glacial Maximum boundary conditions.

Changes in atmospheric temperature and circulation are closely reflected in the relative abundance of the isotopes of the water molecule $H_2^{18}O$, $H_2^{16}O$ and HDO, which is why these isotopes are useful indicators of current and past climate changes (Dansgaard, 1964; Jouzel, 2003; Noone and Sturm, 2010). A temperature-dependent isotopic fractionation occurs during any phase transition because of the differences in their saturation vapor pressures. This causes the ratios of the heavier to lighter isotopes in the different reservoirs of the hydrological cycle to vary depending on the atmospheric conditions (Gat, 1996). In our study, we focused on $H_2^{18}O$ and $H_2^{16}O$. The ratios of the heavy to the light isotopes are denoted by so-called δ values, given as $\delta^{18}O = (R_{SAMPLE}/R_{VSMOW} - 1) \times 1000$ ‰, where R is the ratio of the abundance of the heavier oxygen isotope ^{18}O to the abundance of the lighter isotope ^{16}O. Furthermore, R_{SAMPLE} and $R_{VSMOW} = 2.0052 \times 10^{-3}$ are the isotopic concentrations of the sample and of VSMOW (Vienna Standard Mean Ocean Water), respectively. In the tropics, $\delta^{18}O$ in precipitation ($\delta^{18}O_{precip}$) is closely related to the precipitation

amount ("amount effect", Dansgaard, 1964). Thus, highly depleted stable isotope concentrations are observed during time periods of intense precipitation (Rozanski et al., 1993). At high latitudes, $\delta^{18}O_{\text{precip}}$ is strongly correlated with the local surface temperature ("temperature effect", Dansgaard, 1964; Rozanski et al., 1993) and for temperatures below 14°C, the annual-mean $\delta^{18}O_{\text{precip}}$ is closely related to the annual-mean surface temperature T as $\delta^{18}O = 0.62‰/°C\ T - 15.25‰$ (Dansgaard et al., 1973; Johnsen et al., 1989). Models have been used to determine whether this present-day temperature-$\delta^{18}O_{\text{precip}}$ relationship could be extended to climates that differ starkly from the present (e.g., Lee et al., 2008). Stable water isotopes have been included in the hydrological cycle of various global atmospheric models, namely, GISS (Jouzel et al., 1987), ECHAM (Hoffmann et al., 1998), MUGCM (Noone and Simmonds, 2002), CAM2.0 (Lee et al., 2007), LMDZ (Bony et al., 2008), CAM3.0 (Noone and Sturm, 2010) and the atmosphere-ocean coupled model HadCM3 (Tindall et al., 2009). These models have been successfully used for simulating the present and paleoclimatic distributions of the stable isotopes in the global hydrological cycle. Charles et al. (1994) find that changes in moisture transport and source regions for Greenland at the LGM may have produced an isotopic response independently of temperature changes. A similar result has also been found for shorter (millennial-scale) climate variations (Liu et al., 2012). Masson-Delmotte et al. (2006) show that a major part of Greenland and Antarctic coolings of the GCM simulations is caused by the prescribed local elevation increase due to ice sheets at the LGM. Werner et al. (2000) find an increased seasonality in the annual cycle of precipitation over Greenland during the LGM, but not over Antarctica. Conventionally, the spatial slope over a region (the relationship between $\delta^{18}O_{\text{precip}}$ and temperature over a region) was assumed to hold through different climates, irrespective of time, and the temporal slope (relationship of $\delta^{18}O_{\text{precip}}$ with surface temperature at a single geographical location through different climates over time) was considered to be similar to the spatial slope

(Jouzel, 2003). Modeling studies (for example, Lee et al., 2008) find that the apparent temporal slope over eastern Antarctica is half of the observed spatial slope for the LGM and that the value of the temporal slope is related to the temperature decrease over the Southern Ocean. These studies point to the importance of understanding the influence of the various forcing factors on the isotope distribution.

In our study, we aim to understand the change in $\delta^{18}O_{precip}$ during the LGM and associate the changes to the influence of the different boundary condition constraints. Following Broccoli and Manabe (1987b), we employed a similar method using an atmospheric general circulation model to test the effect of the individual boundary conditions on the Last Glacial Maximum climate in terms of surface temperature, precipitation and $\delta^{18}O_{precip}$.

3.3 The model and experiments

3.3.1 The model

We used the NCAR Community Atmosphere Model CAM3.0 (Collins et al., 2006) with a water isotopes scheme included, hereafter referred to as IsoCAM. The isotopic version of CAM is based on the earlier isotopic scheme of Noone and Simmonds (2002), but includes a more sophisticated treatment of surface exchange and cloud processes to make use of the multiple water phases predicted by CAM (Noone, 2003, 2006; Noone and Sturm, 2010; Sturm et al., 2010). The spatial resolution employed in our experiments corresponds to a spectral truncation of T31 and 26 hybrid levels in the vertical. The related Gaussian grid has a spatial resolution of approximately 3.75°(48 grid points in latitude and 96 grid points in longitude). Each atmospheric grid box in CAM3.0 contains a specific fraction of land, ice, or ocean. The ability of CAM3.0 to efficiently simulate the global hydrological cycle is detailed in Hack et al. (2006). CAM is coupled to the Community Land Model, CLM (Bonan et al., 2002),

which uses the same grid as the atmospheric model. CLM includes different forms of land surface types within each grid cell, namely lakes, glaciers, wetlands and up to 16 land plant functional types (PFTs) that can include a bare soil (Dickinson et al., 2006). For the calculation of isotope ratios over land a simple bucket model (Manabe, 1969) is used, which does not differentiate between evaporation and river runoff or different soil types (Deardorff, 1977; Noone and Simmonds, 2002). The isotope ratios over land do not take into account the fractionation during evapo-transpiration or the effect of different vegetation types.

A thermodynamic sea-ice model (CSIM) represents the sea ice component of the model. CSIM computes the surface fluxes when used with prescribed SST. It further predicts snow depth, brine pockets, internal shortwave radiative transfer, surface albedo, ice-atmosphere drag and surface exchange fluxes without the use of a flux coupler (Collins et al., 2006).

The stable isotope ratios of water in the hydrological cycle of IsoCAM are transported through the atmosphere and the ground by the same processes (advection, moist convection, evapo-transpiration etc.) used to transport normal water (Noone and Sturm, 2010). The isotopes of hydrogen are also included in the model, but were not analyzed in the present study. The isotopic fractionation occurs with every phase change of the water species in the model hydrology. IsoCAM employs a semi-Lagrangian formulation for the water vapor and tracer transport (Williamson and Rasch, 1994; Williamson and Olson, 1994). This formulation uses a shape-preserving interpolation method (Williamson and Rasch, 1989), which avoids the generation of spurious minima or maxima through supersaturation by the transport of water vapor (Williamson and Olson, 1994). The scheme has been found to be sufficiently accurate for conserving isotopic ratios during advection to low-temperature environments (Noone and Simmonds, 2002; Noone and Sturm, 2010), however, it does not guarantee mass conservation (Staniforth and Côté, 1991; Rasch and Williamson, 1990;

Williamson and Olson, 1994; Williamson and Rasch, 1994). A "mass fixer"that re-
peatedly restores global mass is used in CAM3.0 to account for this imbalance (Collins
et al., 2004). Studies with the MUGCM (Noone and Simmonds, 2002) find that the
application of such a mass fixer leads to fictitious changes in the isotope distribution,
as the mass restoration is not local and the mass is not balanced where the spurious
sinks/sources have removed/added the mass, which affects especially the polar re-
gions. Since IsoCAM gives a better tracer-tracer correlation without the application
of an a posteriori mass fixer (not shown), our simulations were carried out without
mass fixing.

3.3.2 Experiments and boundary conditions

A simulation with all the boundary conditions set to LGM values was carried out fol-
lowing the PMIP2 (Paleoclimate Modelling Intercomparison Project) protocol (LGM-
combined hereafter). In addition, a series of experiments was carried out by changing
the individual boundary conditions (greenhouse gases, ice sheet albedo and topog-
raphy, SST along with sea-ice concentration, orbital parameters) each at a time to
LGM values. A pre-industrial (PI, approximately 1800 AD) simulation with bound-
ary conditions also according to the PMIP2 protocol (Braconnot et al., 2007) served
as the control run. The extent and the height of the ice-sheets at the LGM were
taken from the ICE-5G ice-sheet topography (Peltier, 2004). The SST datasets for
the pre-industrial and LGM periods were derived from previous fully-coupled CCSM3
simulations (Merkel et al., 2010). For the SST and LGM-combined simulations, the
SST dataset for the LGM was used; for all other simulations, the pre-industrial SST
dataset was chosen. In comparison to a multi-proxy reconstruction of the LGM SST
from the MARGO project (MARGO, 2009), the model's LGM SST anomaly with
respect to PI (supplementary Figure 3.1) shows a tropical cooling largely consistent
with the MARGO estimate. However, the proxy data suggest a stronger cooling near

the western coasts of Africa and South America than the model. Otto-Bliesner et al.
(2009) attribute this reduced cooling in the simulations to model deficiencies that pro-
duce biases in tropical upwelling and the thermocline structure, and to insufficient
model resolution. Other PMIP2 models show similar differences from the proxy data
(Braconnot et al., 2012). The PI and LGM SST data used for our simulations were
very similar to the results of higher resolution CCSM3 experiments (Otto-Bliesner
et al., 2006a). For all our experiments, the sea-surface oxygen and hydrogen isotope
ratios were set to the global mean surface ocean values of 0.5‰ and 4‰, respectively
(cf. Craig and Gordon, 1965).

Table 3.1: Summary of experiments and boundary conditions.

Experiment	SST	Orbital year	Topography	GHG	Ice sheet albedo
PI	PI	1950	PI[a]	PI	PI[b]
GHG$_{(LGM)}$	PI	1950	PI	LGM	PI
Albedo$_{(LGM)}$	PI	1950	PI	PI	LGM
Topography$_{(LGM)}$	PI	1950	LGM	PI	PI
SST$_{(LGM)}$	LGM	1950	PI	PI	PI
Orbital$_{(LGM)}$	PI	21 ka	PI	PI	PI
LGM-combined	LGM	21 ka	LGM	LGM	LGM

[a]Present day values are used for the topography and coast lines in the
PI (control) simulation following the PMIP2 protocol.
[b]Present day values are used for the ice sheets in the PI (control) simulation
following the PMIP2 protocol.

The boundary conditions for each experiment are listed in Tables 3.1 and 3.2.
The orbital parameters for the pre-industrial control, GHG, albedo and topography
simulations were prescribed to the reference values of 1950 AD, while the orbital
parameters for the orbital-only and for the LGM-combined simulation were set to the
21 ka BP values (Berger, 1978).

In the GHG experiment, only the atmospheric greenhouse gas concentrations were
reduced to the LGM concentrations to show the direct influence of changes in atmo-
spheric heating due to infrared absorption, rather than the fully integrated climate
response to lower GHG concentrations during the LGM which is better captured by

Table 3.2: Atmospheric greenhouse gas concentrations for the PI and LGM time periods.

Greenhouse gases	Pre-industrial	LGM
CO_2 (ppmv)	280	185
CH_4 (ppbv)	760	350
N_2O (ppbv)	270	200

the stronger forcing provided by prescribing the LGM SSTs. The albedo experiment was conducted by replacing the land-ice cover of the PI simulation with LGM values, thereby only changing the surface albedo to that of the LGM. The topography experiment was conducted by taking into account the change in ice sheet topography and the lowering of sea level during the LGM by 120 m (Fairbanks, 1989). All simulations were integrated for 35 model years, and the last 10 years of each simulation were used for analysis.

The coupled CCSM3.0 model has been shown to successfully reproduce the observed distributions of surface temperature and total precipitation as described in Otto-Bliesner et al. (2006b) and Hack et al. (2006). Here the uncoupled CAM3.0 model is forced with a prescribed SST, and the analysis focuses on the changes to the $\delta^{18}O$ of precipitation that are associated with this SST forcing and other boundary conditions. The annual and seasonal distributions of $\delta^{18}O_{precip}$ for the PI control climate are shown in Figure 3.1.

The IsoCAM model captures well the main features of the annual-mean $\delta^{18}O_{precip}$ when compared to the Global Network of Isotopes in Precipitation (GNIP; IAEA/ WMO, 2006) database (not shown). The temporal $\delta^{18}O_{precip}$-surface temperature (TS) slope between the control run and the LGM-combined simulation was calculated as a linear fit for Antarctica and Greenland as Stemporal= [$\delta^{18}O_{precip}$(LGM) - $\delta^{18}O_{precip}$(PI)] /[TS(LGM) - TS(PI)]. This relationship is a critical metric for interpreting model results because it is most pertinent for estimating past temperature from ice core records. The insight offered by the IsoCAM is in association with the
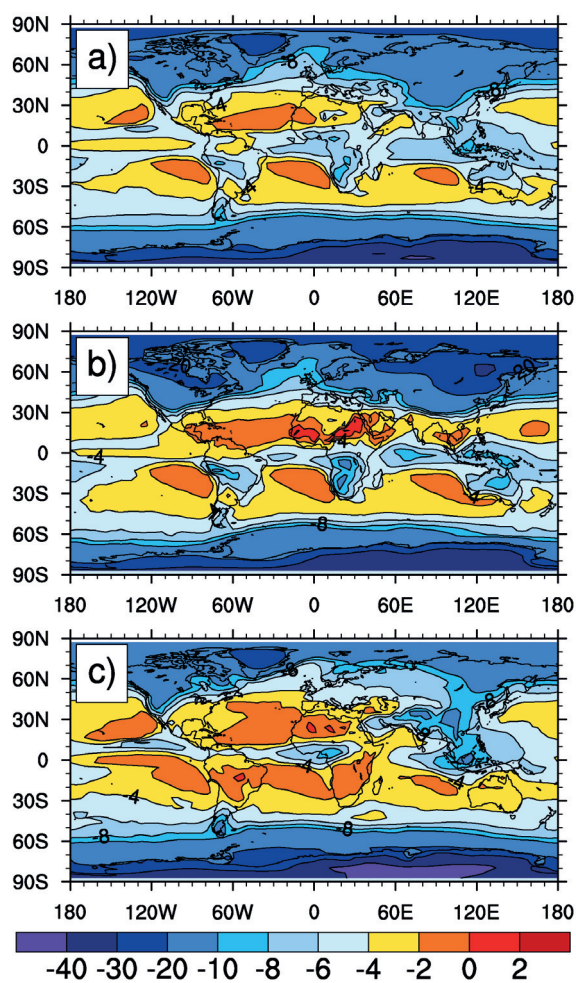
Figure 3.1: Global distribution of $\delta^{18}O_{\text{precip}}$ (‰) for the control run: **(a)** annual mean, **(b)** December–January–February (DJF) season, and **(c)** June–July–August (JJA) season.

simulated changes in $\delta^{18}O_{\text{precip}}$ that correspond to the changes in TS, which in turn result from a systematic variation of the boundary conditions.

Results

3.4 Geographical annual mean responses in surface temperature and precipitation

Because the experimental design makes use of the atmospheric component forced by conditions that result from a coupled model, it is prudent to confirm the performance of the uncoupled simulation. The impact of the glacial boundary conditions on the surface temperature and precipitation in defined geographical regions is summarized in Tables 3.3 and 3.4, respectively. The global annual-mean cooling in the surface temperature was 4.1°C in our LGM-combined experiment with respect to the PI experiment, while the reduction of global annual-mean precipitation was $0.22 \, \mathrm{mm \, day^{-1}}$, in good agreement with previous coupled simulations using CCSM3 (Otto-Bliesner et al., 2006a). The SST experiment brought about a global mean cooling of 2.79°C. The direct influence of albedo and GHG changes was a cooling of 0.18°C and 0.14°C in these experiments, respectively, which was comparatively small, and much smaller than the response that results from them when coupled with ocean surface temperature. The fixed SST suppressed the ocean-atmosphere feedback and so only the land temperature was free to interact with the CO_2 change. The change in topography caused a mean cooling of 0.59°C in the Northern Hemisphere (NH), while in the Southern Hemisphere (SH) the magnitude of the induced cooling was only 0.27°C. The global mean cooling in the orbital experiment was the weakest among all the simulations. The precipitation in the tropics was reduced in all the experiments except for the GHG simulation and showed the strongest response in the SST experiment. The global annual mean energy budgets for our simulations are summarized in Table 3.5. The annual global energy imbalance for the control run at the top of the model (TOM) and the surface was -2.39 $\mathrm{W \, m^{-2}}$ and +5.12 $\mathrm{W \, m^{-2}}$ (a positive sign means

that the system is gaining heat), respectively. The TOM and surface residual energy imbalances for the LGM-GHG and LGM-SST experiments were larger than for the PI experiment. The model conserves energy within $(7.5\pm0.2)\,\mathrm{W\,m^{-2}}$ for all experiments. Since the model is forced with a prescribed SST dataset, the model need not be in energy balance. The surface latent heat flux was higher in the GHG experiment in association with lower global relative humidity due to changes in the atmospheric longwave heating profile, while it was reduced in other experiments.

Table 3.3: Annual mean surface temperature (TS) in °C over the globe ($\mathrm{TS_{global}}$), land points alone ($\mathrm{TS_{land}}$), Northern and Southern hemispheres ($\mathrm{TS_{NH}}$, $\mathrm{TS_{SH}}$), and tropics ($\mathrm{TS_{tropics}}$; 20° S to 20° N) in the different experiments. The difference to the control experiment is given in the adjacent columns.

Experiment	$\mathrm{TS_{global}}$		$\mathrm{TS_{land}}$		$\mathrm{TS_{NH}}$		$\mathrm{TS_{SH}}$		$\mathrm{TS_{tropics}}$	
PI	12.89		6.70		13.057		13.01		25.66	
$\mathrm{GHG_{(LGM)}}$	12.75	-0.14	6.28	-0.42	12.82	-0.24	12.96	-0.05	25.63	-0.03
$\mathrm{Albedo_{(LGM)}}$	12.71	-0.18	6.08	-0.62	12.69	-0.37	13.00	-0.01	25.66	0.00
$\mathrm{Topography_{(LGM)}}$	12.45	-0.44	5.32	-1.38	12.47	-0.59	12.73	-0.27	25.53	-0.13
$\mathrm{Orbital_{(LGM)}}$	12.86	-0.02	6.31	-0.38	13.00	-0.05	13.01	0.0	25.67	0.01
$\mathrm{SST_{(LGM)}}$	10.10	-2.79	2.93	-3.76	10.27	-2.78	9.92	-3.08	24.00	-1.65
LGM-combined	8.79	-4.1	-0.52	-7.22	8.35	-4.71	9.58	-3.42	23.84	-1.83

Table 3.4: As Table 3.3, but for precipitation in $\mathrm{mm\,day^{-1}}$.

Experiment	$\mathrm{precip_{global}}$		$\mathrm{precip_{land}}$		$\mathrm{precip_{NH}}$		$\mathrm{precip_{SH}}$		$\mathrm{precip_{tropics}}$	
PI	2.77		2.10		2.64		2.90		4.44	
$\mathrm{GHG_{(LGM)}}$	2.80	0.03	2.05	-0.04	2.67	0.03	2.94	0.03	4.49	0.04
$\mathrm{Albedo_{(LGM)}}$	2.76	-0.00	2.06	-0.04	2.62	-0.01	2.91	0.01	4.43	-0.01
$\mathrm{Topography_{(LGM)}}$	2.75	-0.01	2.12	0.01	2.61	-0.02	2.89	-0.01	4.40	-0.04
$\mathrm{Orbital_{(LGM)}}$	2.77	0.0	2.10	0.0	2.64	0.0	2.90	0.0	4.43	-0.01
$\mathrm{SST_{(LGM)}}$	2.55	-0.22	1.98	-0.12	2.39	-0.24	2.70	-0.20	4.15	-0.28
LGM-combined	2.55	-0.22	1.86	-0.24	2.38	-0.25	2.71	-0.18	4.17	-0.27

3.5 Zonal mean response of δ^{18}O in precipitation

The orbital, GHG, and albedo experiments produced lower $\delta^{18}\mathrm{O_{precip}}$ values in the northern high latitudes (Figure 3.2). The topography changes also produced lower $\delta^{18}\mathrm{O_{precip}}$ values by 1‰ to 2‰ in the northern high latitudes, where the zonal mean

surface temperature (not shown) was reduced by 2°C to 3°C; and by 2‰ to 3‰ in the southern high latitudes, which was associated both with the significant altitude change over the Antarctic ice sheet and changes to the atmospheric circulation over the Southern Ocean. The LGM-combined experiment yielded a strong response in the Southern Hemisphere mid-latitudes and in the south polar regions with a depletion by 2‰ to 4‰. The SST experiment and the LGM-combined experiment showed similar higher δ^{18}O$_{\mathrm{precip}}$ values in the tropics and equatorial regions where the precipitation was reduced by 5-10% (not shown). In the higher latitudes, however, the effect of the ice-sheet albedo and topography in the LGM-combined experiment led to lower δ^{18}O$_{\mathrm{precip}}$ values as compared to the SST simulation.
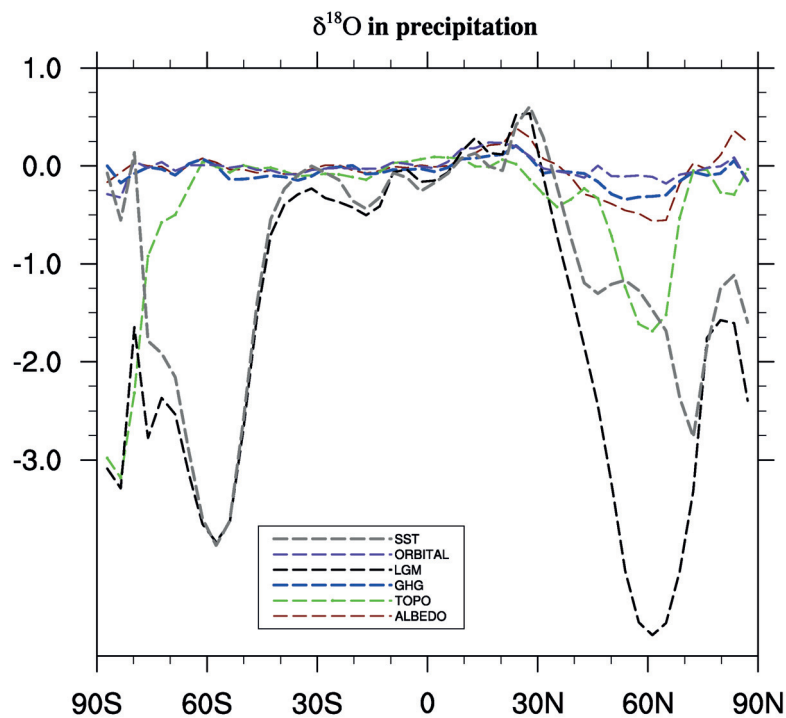
Figure 3.2: The difference of zonal mean δ^{18}O$_{\mathrm{precip}}$ (‰) of each experiment from the control run.

3.6 Annual mean spatial response to the different forcings

3.6.1 Global responses of $\delta^{18}O_{precip}$
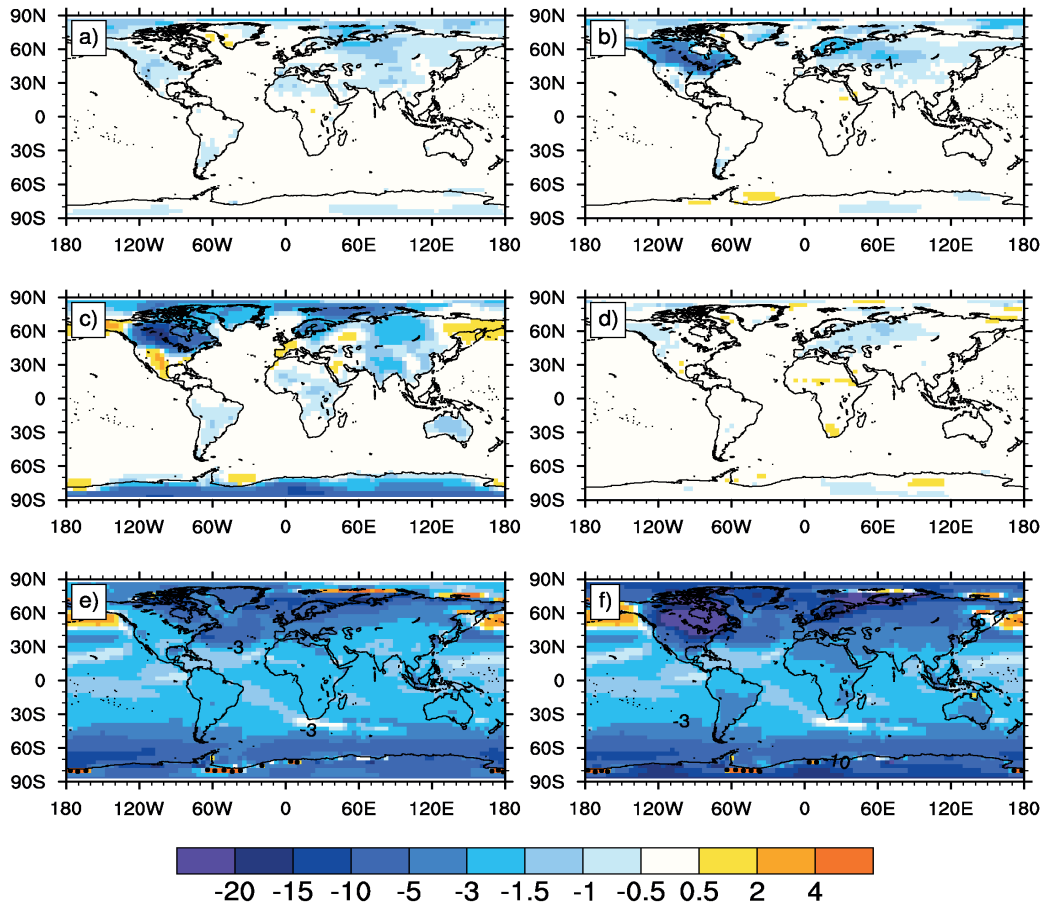
Figure 3.3: Annual mean difference of surface temperature (°C) of **(a)** GHG, **(b)** albedo, **(c)** topography, **(d)** orbital, **(e)** SST, and **(f)** LGM-combined experiments from the control run. Anomalies in the surface temperature at the margins of the Ross and Weddell seas in the SST and the LGM-combined experiments are stippled because the respective grid cells were erroneously defined as ocean.

The annual mean spatial responses in surface temperature, $\delta^{18}O_{precip}$ and precip-

itation are shown in figures 3.3, 3.4 and 3.5 respectively.

The temperature (Figure 3.3a) and precipitation (Figure 3.5a) responses to the direct GHG forcing were small and were only seen over land because the SST was prescribed. A reduced atmospheric CO_2 concentration in a coupled simulation would have directly affected the amount of outgoing longwave radiation and reduced the net downward heat flux at the ocean surface, thereby cooling the ocean surface. Globally, the $\delta^{18}O_{precip}$ response (Figure 3.4a) was small and regions of low temperature in the high latitudes were characterized by low $\delta^{18}O_{precip}$ values.

The effect of the albedo change was seen predominantly in the Northern Hemisphere as the increased albedo of the ice-covered grid cells (i.e., without topographic change due to ice sheets) caused a reduction in surface temperature by 1°C to 5°C (Figure 3.3b). $\delta^{18}O_{precip}$ followed the temperature pattern with lower $\delta^{18}O_{precip}$ values of 1.5‰ to 2‰ with a spatial slope of 0.67‰/°C (Figure 3.4b) over North America, and parts of Eurasia where the precipitation was also reduced compared to PI values (Figure 3.5b).

The ice-sheet topography experiment resulted in a strong cooling (approx. -15°C, Figure 3.3c) and reduction in precipitation (Figure 3.5c) in the regions of elevated orography, because the elevation change was about 2 km over the North American and Eurasian ice sheets and temperature decreases with altitude at a lapse rate of approximately 6.5 °C km-1. $\delta^{18}O_{precip}$ was depleted by 5‰ to 15‰ (Figure 3.4c) and the model predicted a spatial slope of $\delta^{18}O_{precip}$ vs. temperature of 0.61‰/°C over the North American ice sheets. The effect of changes in the orbital parameters on the simulated climate and $\delta^{18}O_{precip}$ was small (Figure 3.4d). Surface temperature was lowered by around 1°C over parts of North America and Europe (Figure 3.3d). Similar to the very weak surface temperature response, only small changes were seen in the precipitation with an increase in the range of $0.1 \ \mathrm{mm\,day^{-1}}$ to $1 \ \mathrm{mm\,day^{-1}}$ over parts of the globe (Figure 3.5d).
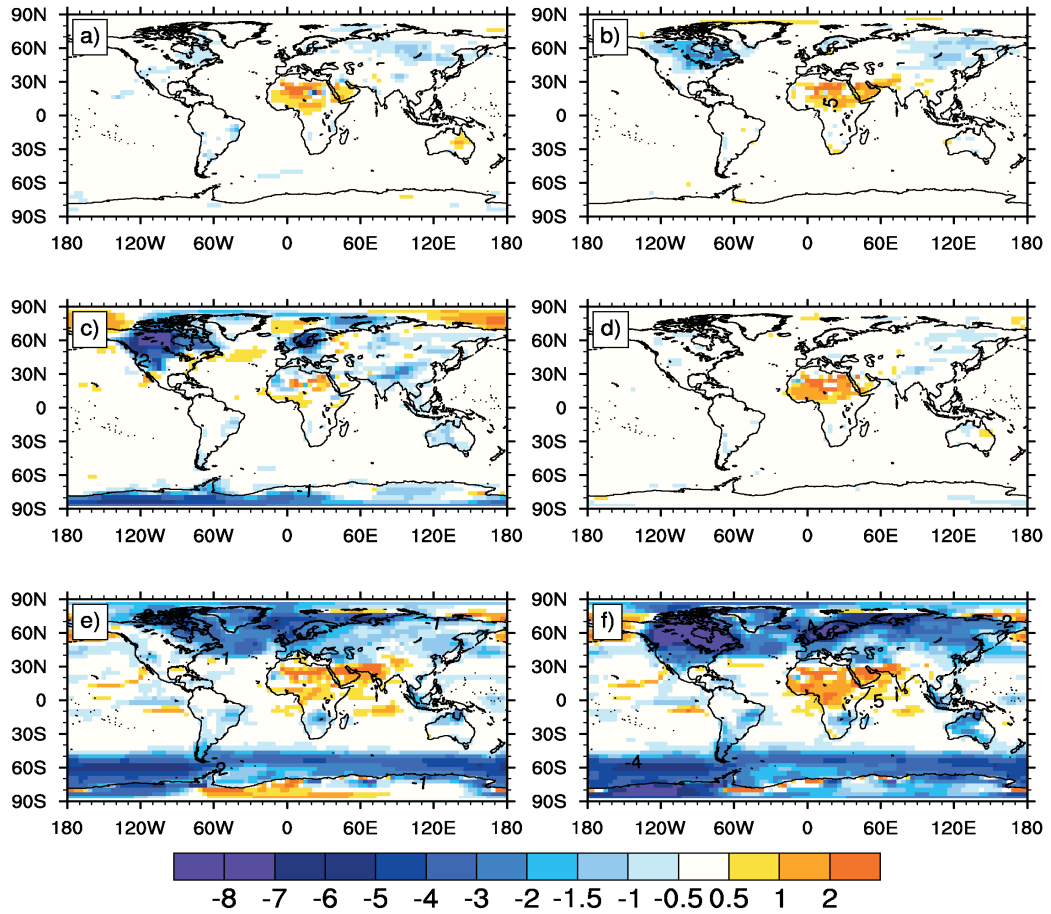
Figure 3.4: Annual mean difference of $\delta^{18}O_{\mathrm{precip}}$ (‰) of **(a)** GHG, **(b)** albedo, **(c)** topography, **(d)** orbital, **(e)** SST, and **(f)** LGM-combined experiments from the control run.

In the SST experiment, the surface temperature over the northern high latitudes and polar regions was reduced by more than 12°C (Figure 3.3e), a direct effect in response to the reduced SST. $\delta^{18}O_{\mathrm{precip}}$ was more depleted over the high latitudes with the reduced temperature and more enriched over the monsoonal regions, where a reduction in annual precipitation was simulated (Figure 3.4e). In the LGM-combined simulation the ice sheets caused strong anomalies in temperature (Figure 3.3f), $\delta^{18}O_{\mathrm{precip}}$ (Figure 3.4f) and also in precipitation (Figure 3.5f) over the North

42
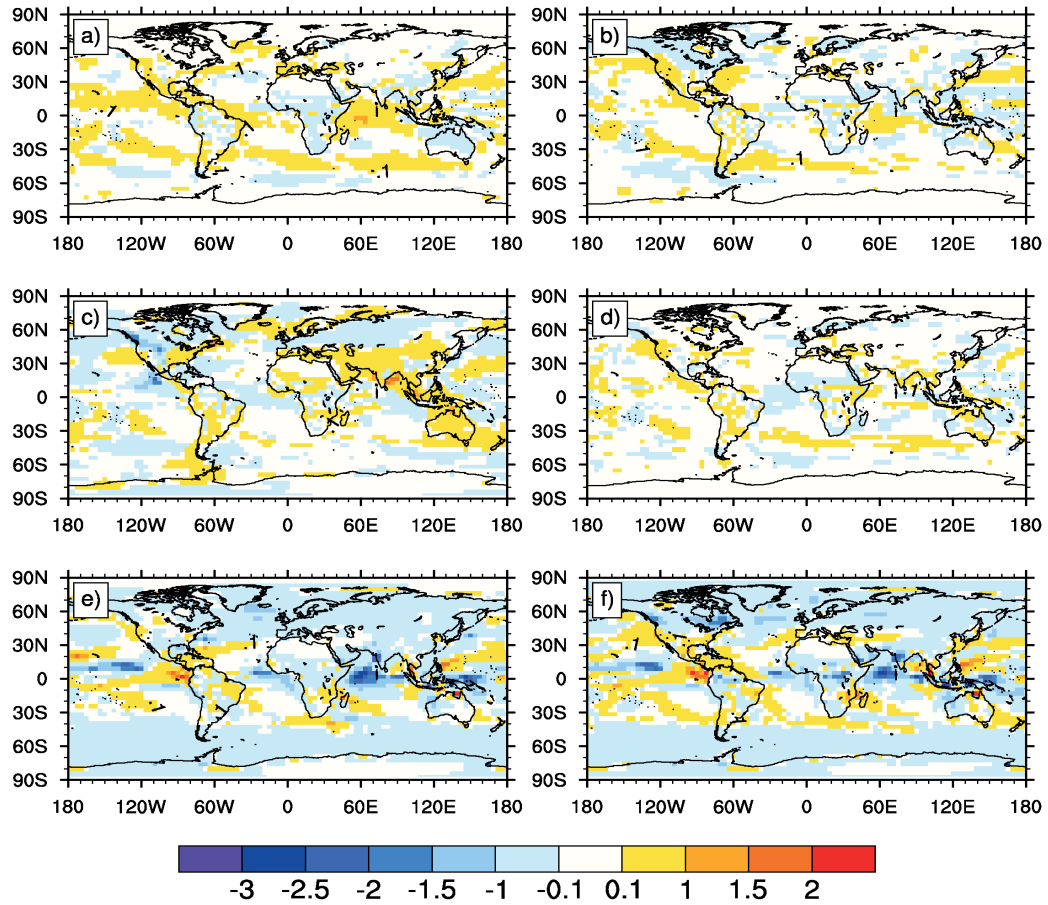
Figure 3.5: Annual mean difference of total precipitation $(\mathrm{mm\,day^{-1}})$ of **(a)** GHG, **(b)** albedo, **(c)** topography, **(d)** orbital, **(e)** SST, and **(f)** LGM-combined experiments from the control run.

American land mass and parts of the North Atlantic Ocean, because the atmosphere became drier, especially in high latitudes. A strong cooling in surface temperature and a similar pattern of reduction in $\delta^{18}O_{\mathrm{precip}}$ with a spatial slope of 0.52‰/°C over the expanded ice sheets were simulated, because of the colder and drier climate over them. Over the northern African continent and over the Indian subcontinent higher $\delta^{18}O_{\mathrm{precip}}$ values of 0.5‰ to 2‰ were simulated. The positive and negative anomalies in precipitation simulated over the tropics were similar to the response modeled in

the SST experiment, which points to a local response in precipitation to the changes in SST.

Table 3.5: Global annual mean of energy terms in the model for the different experiments.

Experiment	FSNT[a]	FLNT	SHFLX	LHFLX	FSNS	FLNS	RESSURF	RESTOM
PI	231.28	233.4	22.36	73.57	157.35	56.03	5.39	−2.12
GHG$_{(LGM)}$	230.76	235.54	22.72	74.55	156.91	56.89	2.75	−4.88
Albedo$_{(LGM)}$	230.19	233.09	22.4	73.37	156.26	55.81	4.68	−2.9
Topography$_{(LGM)}$	230.6	232.73	22.33	72.87	156.79	55.99	5.6	−2.13
Orbital$_{(LGM)}$	231.17	233.28	22.35	73.5	157.22	55.91	5.46	−2.11
SST$_{(LGM)}$	228.82	228.1	23.78	67.58	156.35	56.98	8.01	0.72
LGM-combined	226.32	228.59	23.86	67.35	154.28	57.83	5.24	−2.27

[a]All energy fluxes are given in units of $W\,m^{-2}$. FSNT: net solar flux at top of model (TOM), FLNT: outgoing longwave radiation at top of model, SHFLX: surface sensible heat flux, LHFLX: surface latent heat flux, FSNS: net solar flux at surface, FLNS: net longwave flux at surface, RESSURF: residual energy flux at the surface, and RESTOM: residual energy flux at the top of the model.

3.6.2 Regional mean responses of $\delta^{18}O_{precip}$

The annual-mean $\delta^{18}O_{precip}$ and the difference from the control experiment for North America, Eurasia, Greenland, North Africa, South Africa, northern and southern South America and Antarctica in each experiment are given in Table 3.6 (geographical regions defined by appropriate latitude-longitude boundaries). Over North Africa a strong increase in $\delta^{18}O_{precip}$ values was simulated in all the experiments compared to the control experiment, with the maximum response in the LGM-combined experiment (1.57‰). In South Africa, the depletion was most pronounced in the SST and LGM-combined experiments, and the results showed the dependence of $\delta^{18}O_{precip}$ on the SST change (a lower SST led to lower isotope values). Over Greenland, the mean value of $\delta^{18}O_{precip}$ was -22.3‰ in the LGM-combined experiment and the SST experiment produced the largest signal among all experiments with a depletion by 2.6‰. The geographical region covered by the Eurasian ice sheet was more depleted by 5.9‰ in the LGM-combined experiment, whereas the topography and SST simu-

lations produced a depletion by 2.1‰ and 2.7‰, respectively. Over the Laurentide ice sheet, the $\delta^{18}O_{precip}$ was lower by 10.3‰ in the LGM-combined simulation and the topography change produced a decrease of 3.3‰. Over Antarctica, an area-averaged mean depletion of 2.2‰ in the LGM-combined simulation was obtained, whereas the topography and the SST experiments produced $\delta^{18}O_{precip}$ values lower by about 1.2‰ each.

Table 3.6: Annual mean $\delta^{18}O_{precip}$ in ‰ as area averages for selected geographical regions (given in brackets, also a land mask dataset for LGM was used to select the regions in specific) in the different experiments. The difference from the control experiment is given in brackets.

Experiment	Laurentide ice sheets (30° N–80° N, 150° W–60° W)	Eurasian ice sheet (40° N–80° N, 0–90° E)	Greenland (60° N–88° N, 15° W–70° W)	N. Africa (9° N–25° N, 20° W–30° E)	S. Africa (14° S–38° S, 5° E–37° E)	N. South America (10° N–25° S, 80° W–30° W)	S. South America (28° S–60° S, 50° W–80° W)	Antarctica (68° S–89° S, 180° E–180° W)
PI	−13.84	−12.02	−20.12	−3.90	−6.38	−4.96	−5.01	−28.28
GHG$_{(LGM)}$	−14.08 (−0.24)	−12.37 (−0.35)	−20.23 (−0.11)	−2.84 (+1.06)	−6.48 (−0.09)	−5.18 (−0.21)	−5.40 (−0.38)	−28.28 (0.00)
Albedo$_{(LGM)}$	−14.96 (−1.11)	−12.14 (−0.12)	−20.19 (−0.07)	−2.94 (+0.96)	−6.44 (−0.05)	−5.00 (−0.03)	−5.16 (−0.14)	−28.32 (−0.04)
Topography$_{(LGM)}$	−17.17 (−3.33)	−14.13 (−2.11)	−20.53 (−0.41)	−3.67 (+0.22)	−6.66 (−0.28)	−5.09 (−0.12)	−5.36 (−0.34)	−29.49 (−1.21)
Orbital$_{(LGM)}$	−14.01 (−0.16)	−12.16 (−0.14)	−20.05 (+0.06)	−2.54 (+1.35)	−6.59 (−0.21)	−5.05 (−0.09)	−5.31 (−0.29)	−28.27 (+0.01)
SST$_{(LGM)}$	−15.34 (−1.50)	−14.79 (−2.77)	−22.72 (−2.6)	−2.99 (+0.91)	−7.28 (−0.89)	−5.53 (−0.57)	−6.19 (−1.17)	−29.52 (−1.24)
LGM-combined	−24.22 (−10.38)	−17.95 (−5.93)	−22.33 (−2.21)	−2.32 (+1.57)	−7.24 (−0.86)	−5.58 (−0.62)	−6.73 (−1.71)	−30.56 (−2.27)

3.6.3 The spatial relationship of $\delta^{18}O_{precip}$ to surface temperature and precipitation

In order to understand the relationship between annual mean $\delta^{18}O_{precip}$ and surface temperature under different climate states, a simple linear regression analysis was used to calculate the spatial slopes over Greenland and Antarctica (Figure 3.6a-d). Modelled annual mean values of surface temperature and $\delta^{18}O_{precip}$ for all model grid boxes in inner Greenland and Antarctica were used for the calculation. Over Greenland, the PI control run gave a spatial slope of 0.63‰/°C (Figure 3.6a). The slopes of the SST (0.58‰/°C), topography (0.60‰/°C) (not shown) and LGM-combined experiments (spatial slope of 0.54‰/°C, Figure 3.6b) deviated notably from the PI relationship.
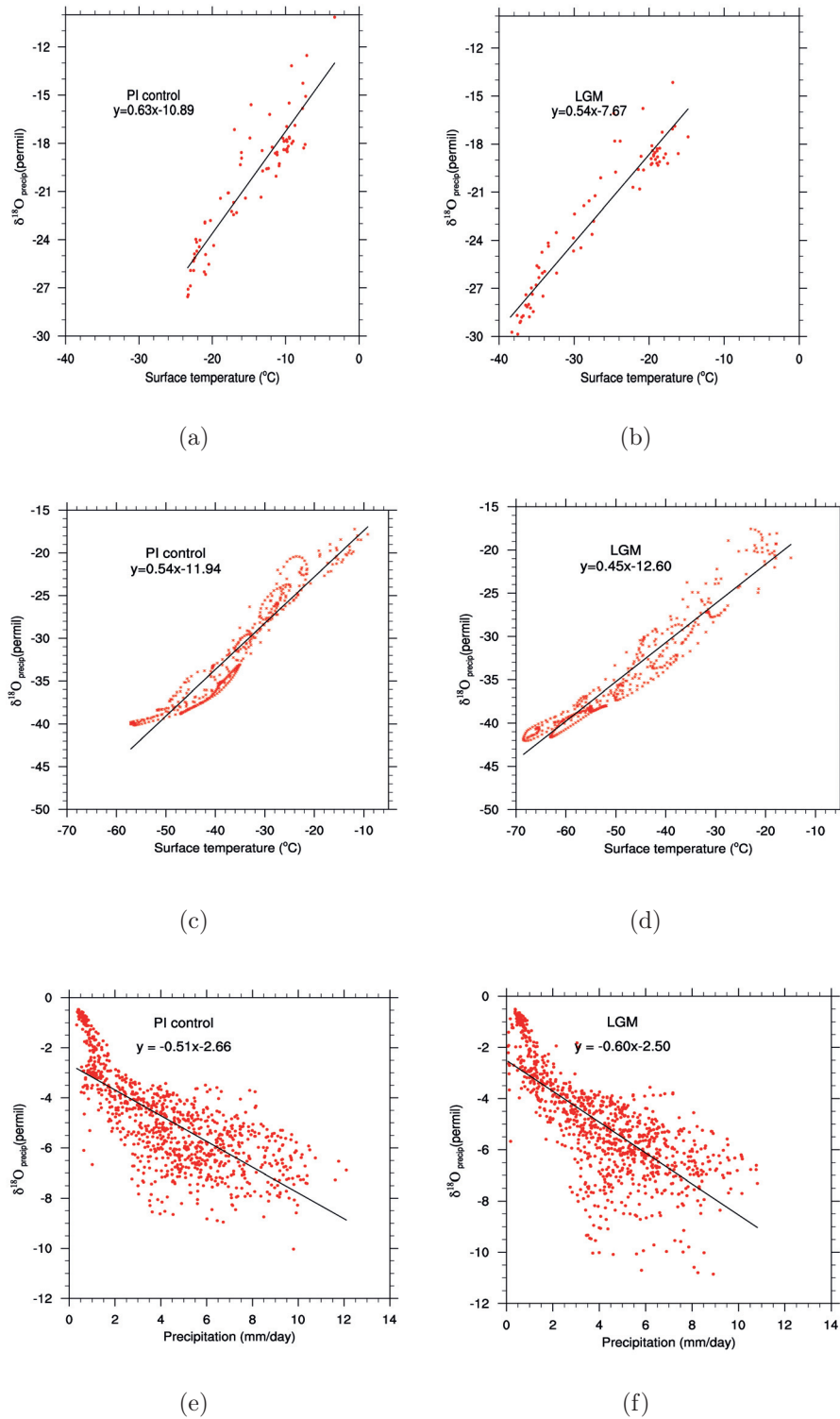
Figure 3.6: The relationship between $\delta^{18}O_{\text{precip}}$ (‰) and surface temperature (°C) is shown for Greenland (**a** and **b**) and Antarctica (**c** and **d**). The relationship between $\delta^{18}O_{\text{precip}}$ (‰) and precipitation (mm day^{-1}) is shown for the tropics (**e** and **f**). Left panels: PI control simulation, right panels: LGM-combined simulation.

Figures 3.6e and 3.6f show the relationship between the annual-mean precipitation and $\delta^{18}O_{precip}$, i.e., the amount effect over the tropics (from 20°S to 20°N) for the PI control and LGM-combined simulations. Both experiments showed lower $\delta^{18}O_{precip}$ values with an increase in the precipitation amount. This was also found for the other experiments (not shown). The modelled relation between total precipitation (P) and $\delta^{18}O_{precip}$ for the control experiment was $\delta^{18}O_{precip} = -0.51P-2.66‰$ (slope in ‰ per mm day^{-1}). The GHG, albedo, topography and orbital experiments produced minor deviations in the range of 0.01-0.02‰ per mm day^{-1} (not shown) from the spatial slope obtained for the control run. In contrast, spatial slopes of -0.60 and -0.58‰ per mm day^{-1} were found for the SST and LGM-combined experiments, respectively.

We used the results of our pre-industrial simulation to compare the spatial slope of $\delta^{18}O_{precip}$ and surface temperature over Antarctica with the observational surface Antarctic snow composition data (Masson-Delmotte et al., 2008), and the present-day model simulations by Sime et al. (2008). For this, we regridded the annual mean results onto a 50 km equal area grid (using only the continental grid cells as in Sime et al. 2008). The spatial relationships of $\delta^{18}O_{precip}$ to the surface temperature were calculated for the entire Antarctic, East Antarctic and the West Antarctic regions. These regions were defined as per Sime et al. (2008). We obtained a slope of 0.54‰/°C over the entire continent, where Masson-Delmotte et al. (2008) obtained 0.80‰/°C. The spatial slope estimated for East Antarctica was 0.55‰/°C, which is lower than the slope obtained from observations (Masson-Delmotte et al., 2008) and the modeled present day slope of 0.73‰/°C by Sime et al. (2008). The slope for the West Antarctic region was estimated as 0.59‰ °C-1, whereas Sime et al. (2008) obtained a value of 1.28‰/°C. Over the entire Antarctic, changes with respect to the control run were simulated in the topography (spatial slope of 0.48‰/°C), SST (spatial slope of 0.48‰/°C), and LGM-combined (spatial slope of 0.45‰/°C) experiments (Figure 3.6d). The albedo and GHG experiments yielded slopes that were identical to those

in the control simulation. The precipitation simulated by the model for the PI control run was found to be larger by 10 kg m^{-2} year^{-1} to 20 kg m^{-2} year^{-1} when compared to the observations (cf. Masson-Delmotte et al., 2011). The over-estimation of the surface temperature and the precipitation rate in the model over Antarctica may have contributed to the lack of depletion simulated by the model. The temporal $\delta^{18}O_{precip}$-surface temperature slope between the PI and LGM-combined simulations calculated for Greenland was 0.51‰/°C, which was about 19% smaller than the PI spatial slope. The temporal $\delta^{18}O_{precip}$-surface temperature slope between the PI and LGM-combined simulations for the entire Antarctic was 0.3‰/°C, which was 50% lower than the PI spatial slope. The temporal slope for the East Antarctic was 0.21‰/°C, which was 60% lower than the PI spatial slope over the region, whereas for the West Antarctic the temporal slope was 22% lower (0.46‰/°C) than the PI spatial slope over the region.

3.7 Seasonal signals in the sensitivity experiments

3.7.1 Seasonal cycle in control and LGM-combined climates

In order to address the seasonal variations of $\delta^{18}O_{precip}$ and the climate variables, the difference between boreal summer (June-August, JJA) and boreal winter (December-February, DJF) for surface temperature, $\delta^{18}O_{precip}$ and precipitation were analyzed for the PI and LGM-combined simulations.

First, we analyzed the seasonal amplitude (JJA minus DJF) for the PI control simulation (Figure 3.7). $\delta^{18}O_{precip}$ values were higher (by 2‰ to 14‰) in the boreal summer (Figure 3.7b) compared to the winter season in the Northern Hemisphere, notably over North America and Eurasia, which may be due to the higher summer temperature (Figure 3.7a). Lower values of $\delta^{18}O_{precip}$ were simulated in the northern tropics during the boreal summer compared to boreal winter. This could be related

to the amount effect, as suggested by the corresponding precipitation signature (Figure 3.7c). When contrasting the LGM-combined and PI seasonality (Figure 3.8), the
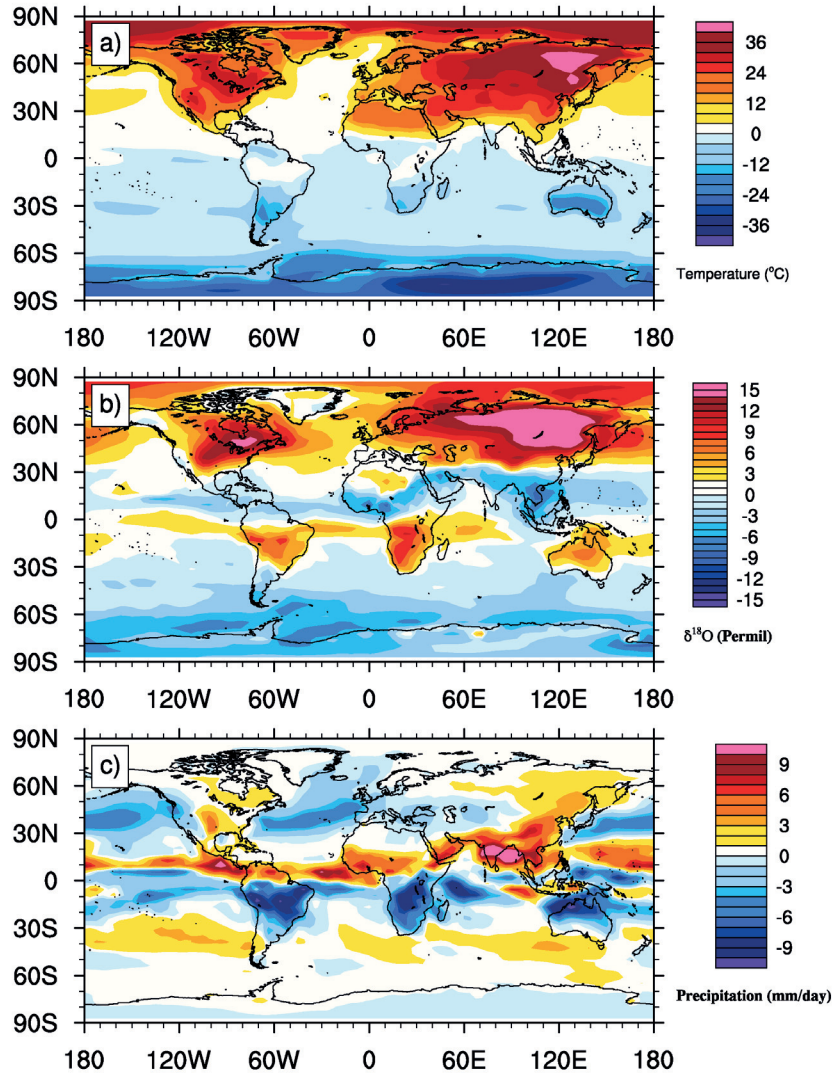
Figure 3.7: The JJA–DJF difference of **(a)** surface temperature (°C), **(b)** $\delta^{18}O_{precip}$ (‰), and **(c)** total precipitation (mm day^{-1}) of the control experiment.

amplitude of the seasonal cycle of surface temperature over the northern latitudes ($>30°$N), especially over Greenland, Eurasia and North America was stronger in the LGM-combined simulation (Figure 3.8a). For $\delta^{18}O_{precip}$, the strength of the seasonal cycle in the control climate was larger over the Laurentide ice-sheet, while over Eura-

sia, the LGM seasonal amplitude was stronger (Figure 3.8b). The seasonality of precipitation in the LGM climate was weaker as compared to the control climate over the monsoon regions and in higher latitudes. Over southern Africa and between 40°N and 50°N on the North American continent, the seasonal amplitude of precipitation was larger during the LGM (Figure 3.8c), possibly because of a reduced winter (DJF) precipitation in the LGM-combined simulation when compared to the PI.
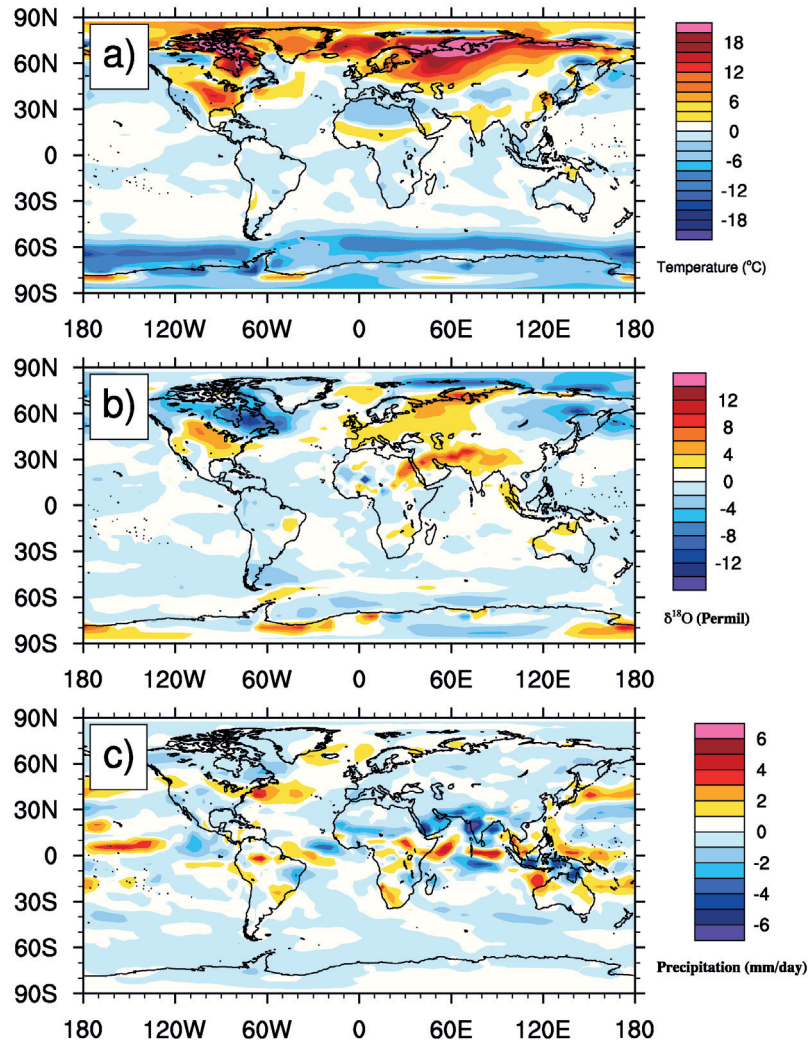
Figure 3.8: The difference of (JJA−DJF) in LGM-combined experiment from the (JJA−DJF) in the control run **(a)** surface temperature (°C), **(b)** $\delta^{18}O_{\text{precip}}$ (‰), and **(c)** total precipitation (mm day^{-1}).

3.7.2 Seasonal response in the experiments in comparison with PI

Atmospheric general circulation features such as monsoons or the seasonal migration of Intertropical Convergence Zone (ITCZ) are reflected in the distribution of $\delta^{18}O_{precip}$. The isotopic ratio of summer precipitation is much lower than that of winter precipitation and leads to lower summer $\delta^{18}O_{precip}$ values in connection with the precipitation amount, especially in the tropics (seasonality and amount effect of isotopes, Dansgaard, 1964).

Therefore, in this section, we analyze the seasonal response of $\delta^{18}O_{precip}$ in the individual experiments with respect to the PI control climate. The winter and summer anomalies of $\delta^{18}O_{precip}$ are shown in Figures 3.9 and 3.10, respectively. Lower
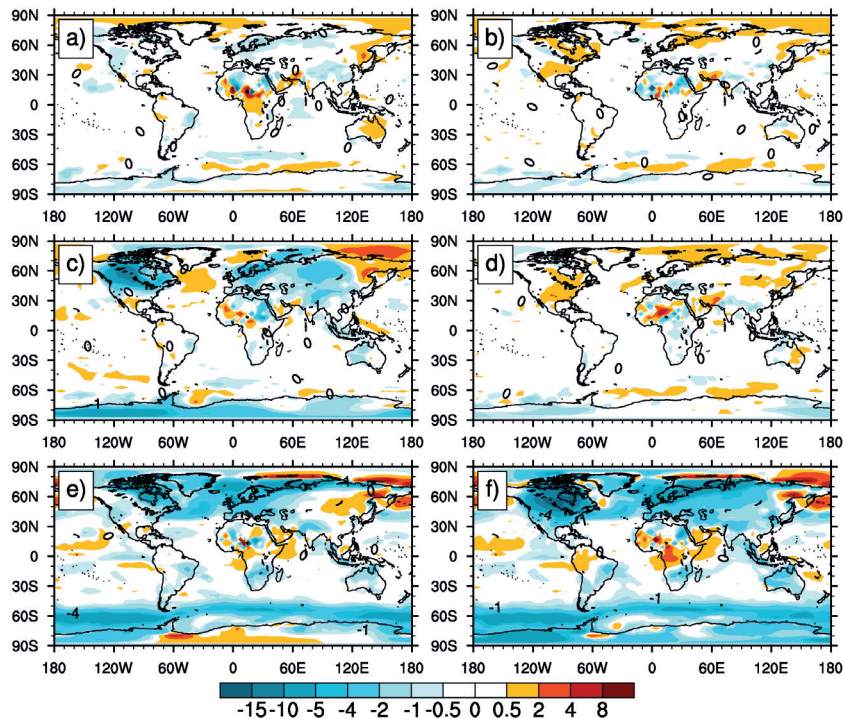
Figure 3.9: The anomalies of $\delta^{18}O_{precip}$ (‰) for **(a)** GHG, **(b)** albedo, **(c)** topography, **(d)** orbital, **(e)** SST, and **(f)** LGM-combined experiments from the control experiment for the boreal winter (DJF).

$\delta^{18}O_{\text{precip}}$ values were simulated in the Northern Hemisphere in the topography, SST and LGM-combined simulations in the DJF and JJA seasons (Figure 3.9 and Figure 3.10 respectively) when compared to the control simulation, which could be a result of the temperature effect due to the reduced SST and the changes in the atmospheric circulation brought about by the topography changes. In the DJF season, $\delta^{18}O_{\text{precip}}$
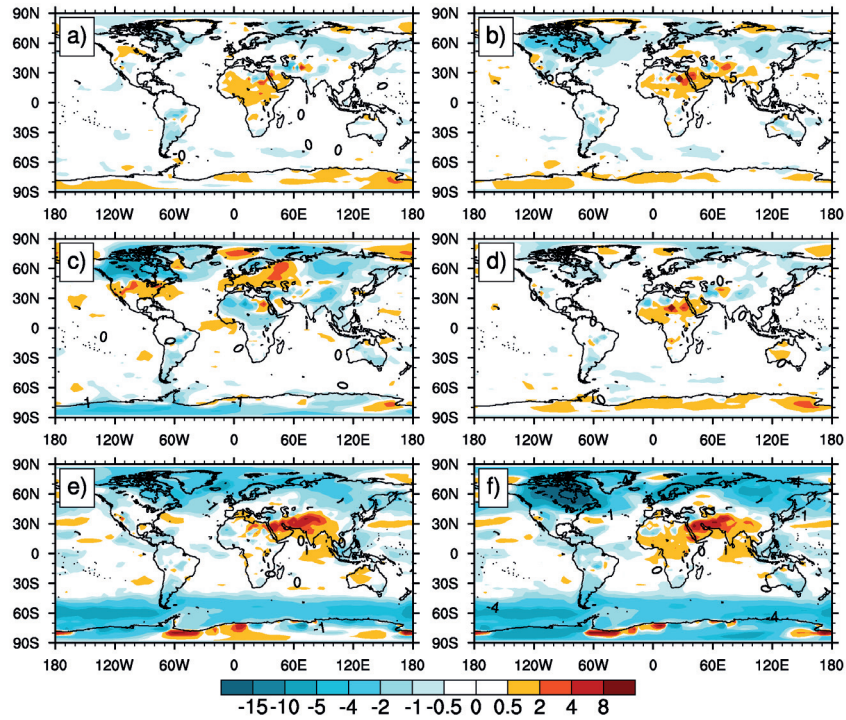
Figure 3.10: As Fig. 9, but for JJA season.

values were lowered by 5‰ to 10‰ over western Antarctica in the topography, LGM-combined and SST experiments. The albedo experiment produced summertime lower $\delta^{18}O_{\text{precip}}$ values over North America and the response was stronger than in winter. The topography experiment produced higher $\delta^{18}O_{\text{precip}}$ values in the south of the North American continent. Higher $\delta^{18}O_{\text{precip}}$ values were simulated over central Antarctica in the SST experiment, both in winter and summer. It should be noted that the direct influences of GHG forcing provided a minimal response in both winter and summer seasons over land. The higher $\delta^{18}O_{\text{precip}}$ values in the boreal summer in

the SST and LGM-combined simulations over Africa and South Asia were correlated with the reduced summer monsoon intensity (not shown) in these experiments.

3.7.3 Isotopic content of the atmospheric water vapor

The isotopic ratio in precipitation depends on the isotopic content of the atmospheric water vapor, which in turn changes with the atmospheric circulation. In the present study, the topography and LGM-combined experiments produced the greatest changes in the atmospheric circulation and seasonal distribution of the δ^{18}O content of the water vapor. Therefore, we focus on these experiments in the remainder of this section.

The isotopic content of water vapor at the 500 hPa level showed a wintertime depletion (Figure 3.11) over the ice sheets in the topography experiment compared to the control run. The 500 hPa geopotential height field showed a split over the Laurentide ice sheet in the flow due to the topography, in agreement with previous LGM modeling experiments (Otto-Bliesner et al., 2006a). A trough in the geopotential height field indicated enhanced storm activity over Eurasia and North Atlantic in the winter season of the LGM-combined simulation (Figure 3.11a), with a ridge over western North America and a trough over the east of the continent. The more westerly winds over central and northern Greenland in winter, also the remote moisture transport from North America with lower δ^{18}O values relative to a North Atlantic source caused lower δ^{18}O values in the water vapor over Greenland. In contrast, higher δ^{18}O values in water vapor were found over the North Pacific and over eastern Eurasia where southeasterly wind anomalies were simulated with respect to the PI experiment. Another feature of the 500 hPa winter circulation was enhanced transpolar winds from Eurasia to the northeastern part of the North American continent in the topography as well as in the LGM-combined experiment. Higher δ^{18}O values in winter over the central North Pacific in the topography experiment (Figure 3.11b
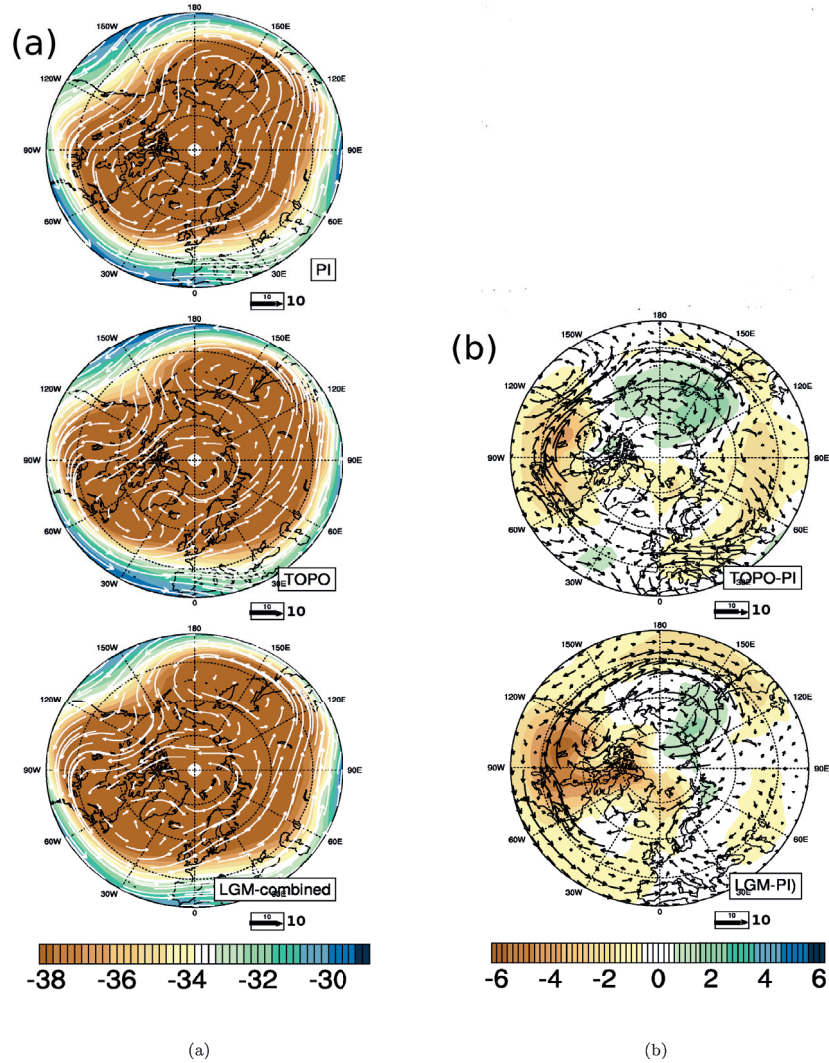
Figure 3.11: 500 hPa winter (DJF) circulation. Left panels: δ^{18}O (‰) in the vapor and wind vectors (m s^{-1}) overlaid for the PI, topography and LGM-combined experiments; right panels: the difference of the same from the PI control run.

(a)   (b)
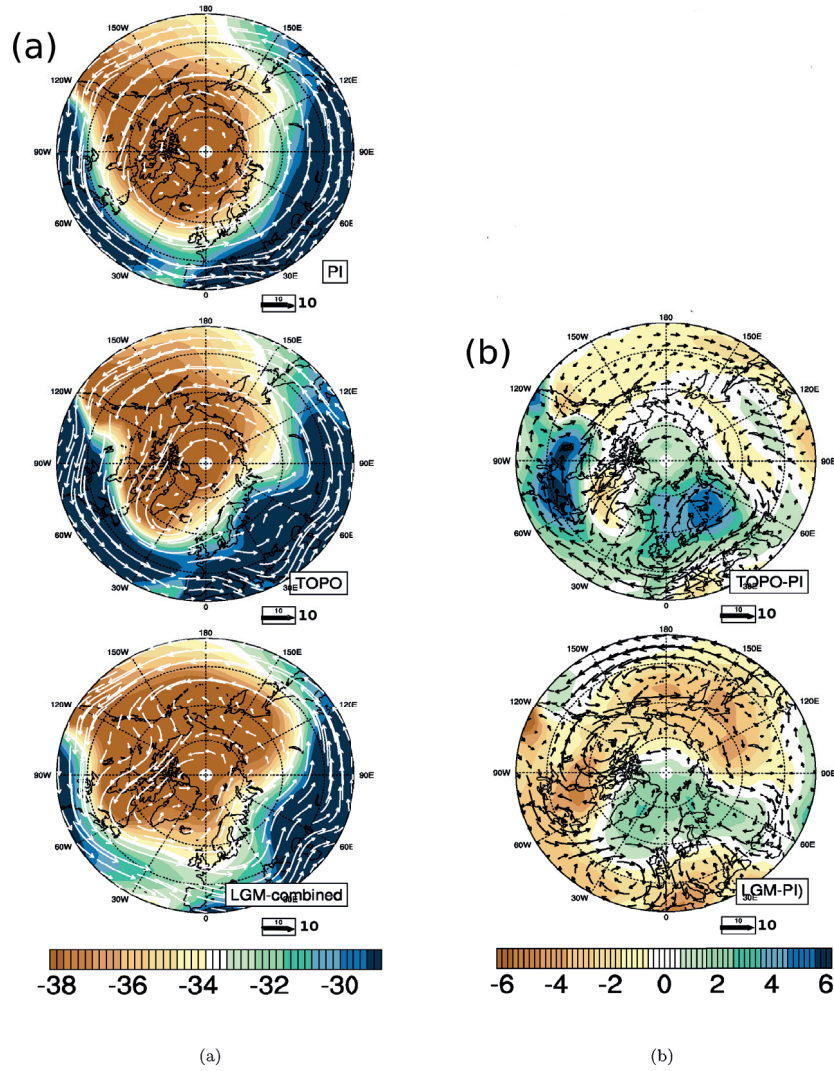
Figure 3.12: As Fig. 3.11, for JJA
season.

middle) were absent from the LGM-combined experiment (Figure 3.11b bottom).

In the summer season (Figure 3.12), higher δ^{18}O in water vapor were simulated over Greenland and north-western Eurasia, and lower δ^{18}O in water vapor were simulated over the Laurentide ice sheet in the LGM-combined experiment when compared with the control run (Figure 3.12b bottom). Higher δ^{18}O values in water vapor over Eurasia and over the Laurentide ice sheet were seen in the topography experiment. Also, the circulation from Eurasia and the North Atlantic to central and southern

Greenland was strengthened due to stronger eddy activity, along with a strengthening of the circumpolar winds (Figure 3.12b middle). The 500 hPa wintertime circulation responses over North America were similar in the LGM-combined and the topography simulations, whereas the summer circulation in the LGM-combined was distinct from the topography experiment. These differences in the summer circulation were reflected as opposite signals in the pattern of the $\delta^{18}O$ in vapor (higher $\delta^{18}O$ values in the topography experiment and lower $\delta^{18}O$ values in the LGM-combined experiment) over Northeast and central North America.

3.8 Discussion

To understand the changes in $\delta^{18}O_{\mathrm{precip}}$ between the PI and LGM, a sequential procedure was used to isolate the influence of the different LGM boundary conditions on climate. The experiments enable an examination of the dependence of the $\delta^{18}O_{\mathrm{precip}}$ distribution on different aspects of the atmospheric circulation and precipitation regime that result from the various climate forcing factors.

3.8.1 Simulated climates

The climate in our LGM-combined and PI control experiments was similar to results from existing coupled atmosphere-ocean model simulations (Otto-Bliesner et al., 2006a; Merkel et al., 2010). This was in line with the observation from fixed-SST atmospheric model studies by, e.g., Timbal et al. (1997) and Mahfouf et al. (1994) that an atmospheric GCM forced by SST anomalies from a coupled model run can reproduce the general features of the atmospheric response obtained by the coupled model. The specification of SST at the lower boundary of an atmospheric GCM has the advantage that the atmosphere equilibrates in a few months with the prescribed SSTs. However, prescribing SSTs led to an annual global energy imbalance at the top

of the model and the surface, and the largest effects were seen in the surface energy budgets. The surface temperature and precipitation patterns in the PI and LGM-combined simulations were nearly identical to those of the fully-coupled model, so we expect the simulations to produce consistent mean atmospheric states in response to the forcings, and the anomalies from the control climate to be robust. When compared to the PI simulation, the global annual mean latent heat flux is reduced in all the experiments except the GHG simulation, which in turn balances the decreased global annual mean precipitation.

A change in the albedo alters the absorption and reflection of solar radiation. The albedo effect of the ice sheets is more prominent in the boreal summer months than in the winter months, with a strong reduction of summer surface temperature over North America and Eurasia and a corresponding depletion of $\delta^{18}O_{precip}$. The surface temperature gradient between the ice sheets and the adjacent ice-free areas produced increased summer precipitation over the southern part of North America and the western North Atlantic as also noted by Manabe and Broccoli (1985). In the topography experiment a localized reduction of surface temperature and more depleted values of $\delta^{18}O_{precip}$ were simulated due to drier conditions over the elevated orography. The altitude effect contributed to the lower isotope ratios. The effects of the ice sheet topography were mainly confined to the Northern Hemisphere high latitudes, as an inter-hemispheric heat transport via ocean currents is missing in the experiments. The resulting cooling was much smaller than that obtained by Hewitt and Mitchell (1997), who use an atmospheric general circulation model coupled to a mixed layer ocean model. Qualitatively, our results for the topography experiment match those obtained by Pausata et al. (2011a) with a coupled atmosphere-ocean model, who also obtain a warming over southern North America and western Europe in response to the elevated orography, but on a larger scale.

The global mean temperature change of the orbital experiment was the small-

57

est among all the simulations, which was expected as the orbital parameters for the present day and the LGM are quite similar. The SST played a decisive role in the reduction of tropical surface air temperature and precipitation and consequently led to higher $\delta^{18}O_{\text{precip}}$ values in the SST experiment, which could thus be interpreted as a direct effect of the SST on the tropical climate. Pausata et al. (2011b) similarly find that changes in the Indian Ocean SST alone lead to a decrease in precipitation over the Indian Ocean and subcontinent, hence producing higher $\delta^{18}O_{\text{precip}}$ values over southern and eastern Asia. The global mean cooling brought about by the SST experiment accounted for 67% of the total temperature reduction in the LGM-combined experiment, which clearly demonstrated the importance of the ocean forcing. The precipitation decreased substantially in the LGM-combined simulation, particularly in the ITCZ and the monsoon regions as seen in previous studies Shin et al. (e.g., 2002). In summary, the experiments showed that the SST and topography changes brought about considerable changes in the annual-mean surface temperature and distribution of $\delta^{18}O_{\text{precip}}$. The SST experiment produced a global response, whereas the topography and ice-sheet albedo had more local effects on climate and hence the $\delta^{18}O_{\text{precip}}$ distribution.

3.8.2 Regional annual mean of $\delta^{18}O_{\textbf{precip}}$

From the regional annual means of $\delta^{18}O_{\text{precip}}$ over the different geographical regions (Table 3.6), we infer that each factor produced unique changes in the isotope signals over different regions. The albedo, topography and SST changes were the major factors influencing the annual mean $\delta^{18}O_{\text{precip}}$ over the Laurentide ice sheets. For Greenland and Antarctica, the reduction in SST and the change in topography were the dominant factors that led to more depleted values compared to the PI simulation. The topography and SST effects explained most of the LGM depletion over Antarctica. The regional annual mean of $\delta^{18}O_{\text{precip}}$ over the North American ice sheets for

the LGM-combined experiment is -24‰ (Table 3.6), which is less depleted compared to the approximate value of -31‰ derived for the Laurentide ice sheet (Duplessy et al., 2002). A lowering by 10‰ of $\delta^{18}O_{precip}$ values was produced over the Laurentide ice sheet in the LGM-combined experiment. The topography change alone brought about lower $\delta^{18}O_{precip}$ values of 3‰ over North America, while albedo and SST changes reduced $\delta^{18}O_{precip}$ by 1‰ each. The altitude effect (Dansgaard, 1964) in the topography experiment was evident from the difference to the ice-sheet albedo experiment. The mean value of -17‰ in the LGM-combined experiment over Eurasia was comparatively high with respect to the range of -16‰ to -40‰ proposed by (Duplessy et al., 2002). The annual-mean difference of -2.2‰ between the LGM-combined and PI experiments over Greenland (Table 3.6) was smaller than the difference of -6‰ to -8‰ in $\delta^{18}O_{precip}$ obtained from GRIP/GISP2 estimates (Werner et al., 2000 and references therein). The difference of $\delta^{18}O_{precip}$ between the LGM-combined and PI experiments over central Greenland of -2.67‰ was smaller than the difference of -4.1‰ modeled for the summit region by Werner et al. (2001). The difference in annual-mean surface temperature between the LGM-combined and PI experiments over central Greenland (-13.96°C) was smaller than the reconstructed value from the borehole thermometry (approximately -23°C; Cuffey and Clow 1997). Thus, the over-estimation of surface temperature over Greenland in the model could explain the heavier $\delta^{18}O_{precip}$ value. Over northern and southern South America, the annual-mean depletion was stronger in the SST and LGM-combined experiments compared to the control climate. Previous studies (Clapperton, 1993; Thompson et al., 2000) suggest a drier climate over South America during the LGM (25% of land classified as desert), with colder tropical oceans and weaker inflow of moisture from the ocean. The response of the $\delta^{18}O_{precip}$ to the LGM-combined and LGM-SST forcing hints at the influence of the Atlantic Ocean, Pacific Ocean and Caribbean Sea, which are the major sources of moisture for this continent (Rozanski and Araguás-Araguás, 1995). Sylvestre (2009) suggests

prevailing drier conditions in northern South America and a wetter southern part of the continent. The apparent shift in ITCZ and the wetter zones along with a less supply of moisture with higher $\delta^{18}O_{precip}$ composition from the ocean are expected to be the reason for more depleted values simulated in southern South America than in northern South America. Over North Africa, higher annual-mean $\delta^{18}O_{precip}$ values were simulated in all simulations in spite of small anomalies in precipitation, and the corresponding slopes in the precipitation-$\delta^{18}O_{precip}$ relationships for all the experiments were higher (by 0.1‰ mm day^{-1} to 0.2‰ mm day^{-1}) than for the PI experiment (-0.69‰ mm day^{-1}), except for the topography experiment. These changes were consistent with the amount effect, as was also reported by Risi et al. (2010c) for West Africa. There may be different reasons for the negative precipitation anomalies over West Africa in the individual experiments. It was found that the ice-sheet albedo in LGM is responsible for the changes in the subtropical trade wind pattern and a southward shift of the ITCZ (Chiang et al., 2003). However, the precipitation anomalies could also result from a poor representation of surface temperature and precipitation in our model over this region (Levis et al., 2004; Deser et al., 2005; Meehl et al., 2006). When compared the model results with observed data (GNIP; IAEA/WMO, 2006), it was found that the model in general underestimated $\delta^{18}O_{precip}$ in arid regions such as North Africa, thus a small reduction in precipitation could have caused an exaggerated increase in isotope ratios. Finally, the model is comparatively colder over North Africa, while it overestimates the precipitation in the southern parts when compared to observations. The simulated annual-mean anomaly of $\delta^{18}O_{precip}$ over Antarctica in the LGM-combined experiment agrees reasonably well with the reconstructed difference of 3‰ to 5‰ compared to the present-day value in the Vostok ice core (Lorius et al., 1985).

3.8.3 Spatial relationship of $\delta^{18}O_{precip}$ with surface temperature and precipitation

The $\delta^{18}O_{precip}$-surface temperature relationship simulated in the PI experiment over Greenland has a slope that is slightly smaller (by 0.06‰/°C) compared to observations (Johnsen et al., 1989, $\delta^{18}O=0.67$‰/°C T-13.7‰, T in °C) and results from the ECHAM3 (Werner et al., 2000) and the CAM2 (Lee et al., 2007) atmosphere models. In our LGM-combined experiment, the spatial slope was reduced by 0.09‰/°C over Greenland. Generally, the spatial slopes obtained for the control and LGM climates were similar, as in the results obtained by, for example, Jouzel et al. (1994). The slope of the $\delta^{18}O_{precip}$-surface temperature relationship over Antarctica in the PI simulation (0.54‰/°C) deviates from the observations by Dahe (1994), who derive a slope of 0.84‰/°C, and by Masson-Delmotte et al. (2008) ś result of 0.80‰/°C. The inability of isotope models to accurately simulate the present-day distribution of isotopes over the southern polar regions and the failure to reproduce the inland depletion was discussed in Werner et al. (2000) and Lee et al. (2007). The underestimation of isotopic depletion over Antarctica is suggested to be related to the representation of the cloud microphysics in these models and their representation of the transport of moisture inland (Masson-Delmotte et al., 2008). The reduced slope over Antarctica in our results points to less depletion of isotopes in precipitation with lower temperature in the model over the continent. The warm bias in our model over Antarctica could also be a contributing factor to the lack of the lowest $\delta^{18}O_{precip}$ values observed in polar snow. The tropical amount effect was evident in all our simulations and the slope obtained for the control run was comparable in magnitude with the slope derived from the observed values at the tropical marine stations selected from the GNIP data base (-0.55‰ per mm day^{-1}, Cole et al., 1999; Bony et al., 2008). Except for the SST and LGM-combined experiments, the changes in the $\delta^{18}O_{precip}$-precipitation relation-

ship were negligible, mostly due to the fixed SSTs. The spatial and temporal slopes for Greenland were relatively close when the difference between the LGM-combined and PI simulations was considered (the temporal slope differed by about 19% from the spatial slope). Temperature profiles from borehole thermometry (Cuffey et al., 1994; Jouzel et al., 1997) and temperature estimates from the thermal fractionation of gases (Severinghaus et al., 1998; Severinghaus and Brook, 1999) indicate that the temporal slope over Greenland was about half of the spatial slope. A modeling study by Werner et al. (2000), who obtain a temporal slope smaller by 60% than the spatial slope, attribute this change to the seasonality in glacial precipitation (strongly reduced winter precipitation) over Greenland. We suggest that the absence of a distinct seasonality in precipitation under PI as well as glacial conditions over Greenland in our results led to similar spatial and temporal slopes. The temporal slope obtained over East Antarctica was about half the spatial slope, as also seen in the modeling study by Lee et al. (2008). The reduced winter precipitation in the LGM and the changes in the glacial topography and consequent reduction in surface temperature in West Antarctica could have resulted in the change of the glacial-PI temporal slope. Lee et al. (2008) suggest that the value of the temporal slope is related to the temperature decrease over the Southern Ocean. Comparison of the temporal slopes with that obtained by the modeling studies of Werner et al. (2000) and Lee et al. (2008) suggests that the slopes obtained could be model-dependent.

3.8.4 Seasonal cycle of $\delta^{18}O_{\mathrm{precip}}$

As Jouzel et al. (1987) noted for the present-day climate, the seasonal cycle of $\delta^{18}O_{\mathrm{precip}}$ is divided at 30° of latitude, where the zero contour was also found in all our experiments (Figure 3.7b, Figure 3.8b). Observations show that poleward of this latitude the seasonal contrast is stronger and the maximum enrichment in the summer of the respective hemispheres is largest (Feng et al., 2009). These latitudes coin-

cide with regions of strong evaporation and little precipitation due to subsiding air masses. Furthermore, the precipitation in these latitudes is enriched in heavy isotopes because of the proximity to the source regions. It has been argued that the seasonality of isotopes between 20°S and 20°N reflects the atmospheric circulation and that the isotopic minima and maxima in the different seasons represent the positions of the ITCZ (Feng et al., 2009). The seasonal anomalies of $\delta^{18}O_{precip}$ in the simulations show that the influence of the climate factors varies with the seasons. The largest response in $\delta^{18}O_{precip}$ to the ice-sheet albedo was simulated in boreal summer. The higher summertime $\delta^{18}O_{precip}$ values produced over the tropical monsoon regions in the SST and LGM-combined simulations are also an evidence of the dominance of the rainy season on the annual signal and of the relative importance of SST in the distribution of $\delta^{18}O_{precip}$ over the region. The higher $\delta^{18}O_{precip}$ values simulated in the summer season of the LGM-combined experiment is in agreement with previous studies indicating a weaker southwest summer monsoon during the LGM (Manabe and Broccoli, 1985; Van Campo, 1986; Kutzbach and Guetter, 1986; Rind, 1987; Lautenschlager and Santer, 1991) and at the same time, the ITCZ likely shifted southward.

The absence of a strong seasonality in the precipitation rate over Antarctica found in our experiments was also reported in Cuffey and Clow (1997). A similar lack of definite seasonality in precipitation and in isotope distribution over Greenland was found in all the simulations. The SST experiment brought about the largest change in the $\delta^{18}O_{precip}$ distribution over Greenland, both in winter and summer, while the topography experiment produced more depleted $\delta^{18}O_{precip}$ values in summer, when compared to the control experiment.

3.8.5 Changes in the atmospheric circulation

It is suggested that the atmospheric circulation in the LGM was considerably different from the present-day configuration, owing to the elevated ice-sheet orography and in-

creased sea-ice in high latitudes (Broccoli and Manabe, 1987a; Shin et al., 2002; Otto-Bliesner et al., 2006a). Pausata et al. (2011a) conclude that the ice sheet topography in the LGM plays a dominant role in altering the large-scale atmospheric circulation, particularly over the North Atlantic Ocean. Distinct changes in the northern high-latitude circulation were indeed simulated in our topography and LGM-combined experiments with associated differences in the distribution of $\delta^{18}O$ in vapor. Previous studies (Charles et al., 1994; Werner et al., 2001) identify the near-by polar seas, the North Atlantic and North Pacific Oceans and the North American and Eurasian continents as the moisture source regions for glacial Greenland precipitation. When compared to modern conditions, the ice sheets caused a significant reduction of the contribution of moisture from North America, particularly the region covered by the ice-sheets. Werner et al. (2001) also find a southward shift of moisture transport from the North Atlantic and North America to Greenland. Kageyama and Valdes (2000) suggest that in Greenland, the winter precipitation during the LGM is lower because of the changes in atmospheric circulation and the southward deviation of the storm tracks due to the Laurentide ice-sheet, extended sea ice, and also because of the modified latitudinal SST gradient. The drier air mass advected over Greenland causes less precipitation during the winter season in the north. The drier air mass over the ridge in the 500 hPa geopotential height field (not shown) near the margin of the Laurentide ice sheet may have led to more depleted $\delta^{18}O$ in vapor values during winter in both the topography and LGM-combined simulations. The increased northerly flows and trans-polar advection of colder and drier air-masses at the 500 hPa level in the LGM-combined experiment would also have contributed to the drier conditions and more depleted $\delta^{18}O$ in vapor values during the DJF season. When comparing responses of $\delta^{18}O$ in vapor to the topography and the LGM-combined forcing, they are very similar over North America during DJF and opposite during JJA. This indicates that the ice-sheet albedo was the major controlling factor during

64

summer. Pausata et al. (2011a) also find a relatively larger effect of albedo on the upper tropospheric winds in summer. The enrichment of heavy isotope ratios in vapor in the mid-troposphere seen in the JJA season of the LGM-combined and topography simulations over Greenland could be attributed to the advection of enriched water vapor from the North Atlantic and Eurasia, which agrees with Charles et al. (1994), while the North Pacific source of moisture for northern Greenland was not evident in our results.

3.9 Conclusions

Our experiments allowed for an assessment of the effect of the individual climatic boundary conditions on the climate of the LGM, although a complete factor separation analysis (Stein and Alpert, 1993) was beyond the scope of this study. The focus was on the spatial pattern of the climate and corresponding isotopic response and to a lesser degree on its magnitude. We suppressed the feedbacks from the ocean and sea ice by using fixed SSTs derived from previous simulations of a coupled atmosphere-ocean model, which allowed the response to the LGM SST to be considered as a separate factor. This methodology had the advantage of largely isolating the effect of the individual forcing factors (particularly albedo, ice sheet topography and insolation changes) on the atmosphere without the response being dominated by the SST feedback. We note, however, that quantitative aspects of the response to the individual forcing factors in a fully coupled model are likely to be different from our results.

Our simulations indicate that the changes in topography due to the large continental ice sheets and the changes in SST were the two predominant factors determining the distribution of oxygen isotopes in precipitation. The altitude effect and the changes in atmospheric circulation brought about by the LGM topography led to a

depletion of $\delta^{18}O_{\text{precip}}$ in the high latitudes of the Northern Hemisphere. Overall, the albedo and topography of the ice-sheets have a local effect on the surface temperature and precipitation, and the distribution of $\delta^{18}O_{\text{precip}}$ appears to be influenced by these local changes in surface temperature. The lower SST was the dominant factor in reducing the precipitation in the tropical regions, which in turn led to higher $\delta^{18}O_{\text{precip}}$ values in summer. Treating the SST as a separate forcing factor helped to understand the isotopic response particularly in the tropics. The relationship between $\delta^{18}O_{\text{precip}}$ and surface temperature and $\delta^{18}O_{\text{precip}}$ and precipitation was rather insensitive to changes from PI to full LGM boundary conditions. A strong seasonality was lacking in the surface distribution of $\delta^{18}O_{\text{precip}}$ and precipitation over Greenland in all the simulations. The LGM-topography and LGM-combined simulations produced substantial changes in the tropospheric circulation. The changes in atmospheric circulation led to a drying and more depleted $\delta^{18}O$ in vapor in the LGM-combined simulation during boreal winter. In contrast, the summer circulation showed an enhanced southerly flow from the North Atlantic to Greenland with enriched vapor. The increased summertime southerly moisture transport from the North Atlantic to Greenland in the LGM-combined experiment hints that it could be a major source of moisture for Greenland during the LGM. The role of the North Atlantic SST in causing changes in the atmospheric circulation near Greenland could be small, as the 500 hPa anomalies in the $\delta^{18}O$ in vapor in the SST experiment were small and even opposite in sign when compared to the anomalies of the LGM-combined simulation. An isotopic seasonality related to the precipitation amount effect is found over the tropical monsoon regions in our LGM-combined and SST simulations, where the colder and drier Asian continent during the LGM caused a reduction of the land-sea temperature gradient and hence of the intensity of the SW monsoon. Future studies should include at least a mixed layer ocean model to account for the ocean-atmosphere feedback, as well as a possibility to tag the water vapor from different source regions.

3.10 Acknowledgments

Supplemetary Figure
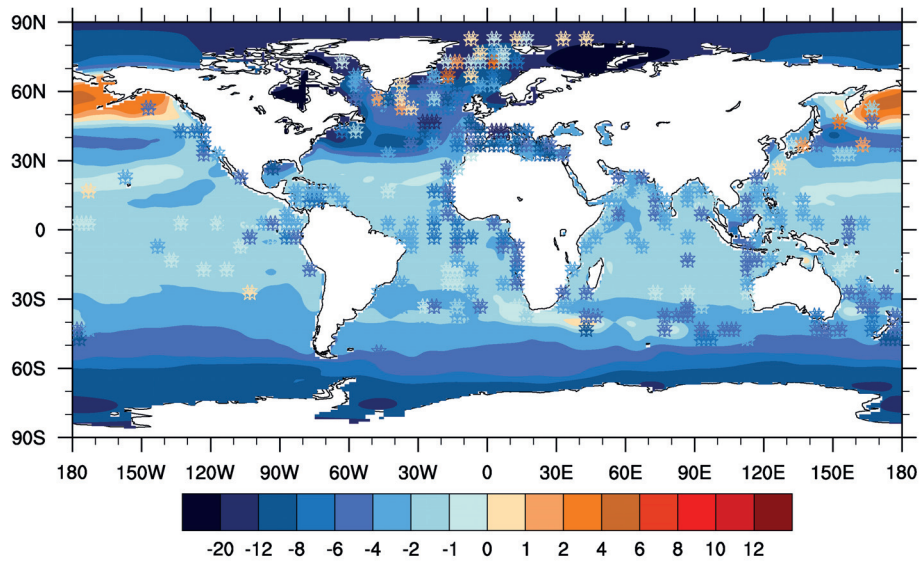
(Supplementary Figure 3.1): Annual mean SST anomaly (°C) for LGM minus PI from the coupled CCSM3.0 run (contours). LGM annual mean anomaly from the MARGO data (°C) is plotted as scatters over the contours with the same color scale.

Chapter IV

Hydrogen isotopes of meteoric water in Africa: Modeling and comparison to data

T. Tharammal, A. Paul, J. A. Collins, U. Merkel and S. Mulitza

4.1 Abstract

In this work we present the results of four different time slice experiments - pre-industrial (PI, approximately 1800 AD), mid-Holocene (6 ka BP), LGM (21 ka BP) and Heinrich Stadial-1 (HS1, 16 ka BP) - using an atmospheric general circulation model fitted with an isotope module. The goal of the study is to analyze the water isotope distribution over the African continent during these time periods. Model results for hydrogen isotope composition of precipitation (δD_{precip}) for these time periods are compared with δD data obtained from the stable hydrogen isotope composition of plant leaf-wax n-alkanes (δD_{wax}). The model results agree with δD_{wax} on the isotopic enrichment of precipitation during the LGM and HS1 and suggest that this was due to reduced summer monsoon intensity. Over the Sahel, the results agree on the increased precipitation and the depletion of isotope distribution during the mid-Holocene, thereby reflecting the amount effect and the relationship between δD_{wax} and precipitation intensity. In the southern subtropics, the model and data

show larger differences in magnitudes of depletion, which we interpret as changes in the remote effects on δD_{precip} during the different climate states.

4.2 Introduction

Tropical African climate is governed by the seasonal migration of the Intertropical Convergence Zone (ITCZ), a band of deep convection at the location of maximum insolation and moisture convergence. This causes northern and southern belts of monsoonal climates with rains in summer. The rainfall distribution over Africa depends on shifts in the large scale wind fields at different levels in the troposphere, sea-surface temperature (SST) variations (Giannini et al., 2003), atmospheric aerosols and changes in land surface boundary conditions (Nicholson, 2000a; Zhao et al., 2011). Equatorial Africa has a humid climate with two rainfall maxima per year. The northern and southern temperate regions of the continent are affected by the equatorward displacement of the mid-latitude westerlies during the respective winter season. The subtropical deserts (the Sahara in the Northern Hemisphere and the Namib coastal desert in South West Africa) are dominated by subtropical anticyclones throughout the year.

The seasonal rainfall over the Sahel is strongly influenced by variations of SST anomalies in the tropical Atlantic, central and east Pacific and the Indian Ocean (Lamb, 1978; Palmer, 1986; Hastenrath, 1990; Bader and Latif, 2003). Nicholson (2001) finds that the wet years in the Sahel are preceded by an anomalously warm tropical Atlantic. A model study by Rowell (2003) finds that Sahel rainfall is also related to SST anomalies in the Mediterranean Sea. The African easterly jet (AEJ) is an important wind structure over northern Africa prominent in summer and helps to generate and maintain the wave disturbances that modulate the rainfall field in North West Africa (Cook, 1999; Thorncroft and Blackburn, 1999; Nicholson, 2001). Since the AEJ is

associated with the divergence of moisture below the level of condensation, a strong jet is assumed to be connected with low precipitation over the western Sahel (Cook, 1999; Nicholson, 2001).

A prominent part of austral summer (December-February) rainfall over much of South Africa (SA) is derived from tropical-temperate trough systems that extend over continental SA and the adjacent SW Indian Ocean (Washington and Todd, 1999; Todd et al., 2004). A second convergence zone, the Congo Air Boundary (CAB), separates the on-land flow from the Atlantic and Indian Oceans, thereby dividing easterly trades and westerly monsoonal wind systems over Africa (Nicholson, 2000b).

Precipitation in eastern Africa is controlled by the position of two convergence zones, the ITCZ and the CAB and topography (Nicholson, 1996). Ummenhofer et al. (2009) find that positive SST anomalies in the western Indian ocean cause enhanced atmospheric moisture content. Consequently the westerly airflow gets strengthened over Central Africa and a strong anomalous convergence of moisture occurs over most of equatorial East Africa. Modeling studies (Latif et al., 1999; Friederichs and Paeth, 2006; Bader and Latif, 2011) also emphasize the relation between Indian ocean SST anomalies and precipitation over East Africa.

Three major time periods during the late Quaternary, i.e., the mid-Holocene (6 ka BP), Last Glacial Maximum (LGM, approximately 23-19 ka BP) and Heinrich stadial-1 (HS1, approximately 18-16 ka BP), present a fitting scenario to study the impact of changes in the atmospheric and oceanic boundary conditions on the continental climate and hydrological cycle over Africa in the past. Climate modeling studies suggest a generally drier climate over tropical Africa during LGM and HS1 (Braconnot et al., 2000; Mulitza et al., 2008) and a wetter climate during the mid-Holocene (Joussaume et al., 1999; Doherty et al., 2000; Texier and Noblet, 2000; Braconnot et al., 2000; Zhao et al., 2005) than the present day climate.

During the early to mid-Holocene, tropical Africa was wetter than today (Gasse,

2000), which is explained by the intensification and northward expansion of the African-Asian monsoon (Braconnot et al., 2007). A high Northern Hemisphere (NH) summer insolation in the early and mid-Holocene enhanced the thermal contrast between land and sea producing stronger summer monsoons (Prell and Kutzbach, 1987; Hewitt and Mitchell, 1996; deMenocal et al., 2000) as the continental surfaces respond faster to the seasonal cycle of insolation because of the low thermal capacity of the land. A multi-model analysis of the role of the ocean in the African monsoon during the mid-Holocene (Zhao et al., 2005) finds that the dipole (higher temperature to the north of 5°N and lower temperature to the south) in late summer SST anomalies in the tropical Atlantic increases the length of the African summer monsoon and precipitation over the Sahel. The Paleo Climate Modeling Intercomparison Project (PMIP) (Braconnot et al., 2000) finds that the ITCZ in the north only experienced small northward or southward shifts between the LGM and mid-Holocene periods. The modeling study by Kutzbach et al. (1996) asserts the need to include not only orbital forcing but also the vegetation feedback in modeling the mid-Holocene climate. During PMIP2, this has been addressed for the first time using comprehensive climate models (Braconnot et al., 2007).

Heinrich Events were six millennial-timescale, abrupt cool episodes during the late Pleistocene around the North Atlantic as a result of massive ice-berg discharge to the ocean (Heinrich, 1988; Broecker et al., 1992; Hemming, 2004). The Heinrich Events, which are identified as H1 through H6 from the youngest to the oldest, were followed by strong SST and salinity reductions in the North Atlantic (Bond et al., 1992; Vidal et al., 1997), which is assumed to have caused the slow-down of the Atlantic meridional overturning circulation (McManus et al., 2004; Brady and Otto-Bliesner, 2011). Climate models and proxies also show that the monsoon circulation was altered during the Heinrich events (Pausata et al., 2011b; Stager et al., 2011).

During the LGM, paleo-proxy records indicate generally dry conditions in both

hemispheres (Shi et al., 1998; Prentice and Jolly, 2000; Wu et al., 2007), while from orbital forcing increased summer precipitation in the southern tropics is predicted. Reduced SSTs in the tropics (MARGO, 2009) might have played a significant role in the tropical climate by reducing the evaporative flux (Gasse (2000) and references therein). Proxy studies suggest a dry central equatorial Africa during the LGM (Schefuß et al., 2005; Tierney et al., 2008). A study by Schefuß et al. (2005) using plant wax hydrogen isotope data and an alkenone-based SST reconstruction finds that precipitation in Central Africa during the past 20,000 years was mainly controlled by the difference in sea surface temperatures between the tropics and subtropics of the South Atlantic Ocean, which opposes the assumption that the moisture availability in Central Africa was determined by the position of the ITCZ alone. In southeastern Africa, a climate reconstruction by Schefuß et al. (2011) suggests that remote atmospheric forcing by cold events in the northern high latitudes is a major driver of hydro-climatology, in contrast to the Indian ocean SST variability proposed by Stager et al. (2011).

Stable isotopes of water in precipitation can be used to track the hydrological cycle because of the dependance of water isotopes on equilibrium and kinetic fractionation associated with the phase transitions of water. The isotope ratio is represented as δ value in ‰ with $\delta = (R_{SAMPLE}/R_{VSMOW}-1) \times 1000$, where R_{SAMPLE} is the ratio of the heavier isotope to the lighter isotope of the sample and $R_{VSMOW} = 155.76 \times 10^{-3}$ ‰ is the hydrogen isotopic ratio of Vienna Standard Mean Ocean Water. The fractionation of the stable isotopes of hydrogen and oxygen is strongly influenced by climate (Dansgaard, 1964). Rainfall amount, moisture source, altitude, distance from the coast, and humidity are the major factors influencing the stable isotope ratios of water in precipitation in the tropics (Dansgaard, 1964; Rozanski et al., 1993; Gonfiantini et al., 2001).

In the monsoon domains, the ratio of isotopes in precipitation is mostly related to

73

the amount of precipitation (amount effect; Dansgaard, 1964; Rozanski et al., 1993; Dettman et al., 2001; Lee and Fung, 2008; Risi et al., 2008b). Vuille et al. (2003) suggest that the amount effect is caused by the small-scale vertical convection associated with precipitation in the tropics. As the condensation proceeds, the heavier isotopes are preferentially removed and the relative abundance of the heavier isotopes in the water vapor decreases. Since the total amount of precipitation increases with the increase in the convective nature of a particular rainfall event, the isotopic composition of the precipitation gets more depleted. This effect can be amplified by the fact that isotopic exchange with water vapor and evaporative enrichment of raindrops are both greatly reduced with heavy rains (Dansgaard, 1964). Contrary to Vuille et al. (2003), Risi et al. (2008a) conclude that the predominant processes leading to the amount effect in the tropics are related to the fall and reevaporation of the precipitation, rather than processes occurring during the ascent of air parcels. They further find that the fractionation process during rain fall contributes the most to the amount effect in regimes of weak precipitation, and the injection of vapor from the unsaturated downdraft is predominant in regimes of strong precipitation.

Another factor that affects the isotope ratios over land is continentality, also referred to as the distance-from-coast effect. As oceanic air masses move inland and lose water through precipitation, the remaining atmospheric water vapor becomes progressively depleted in heavy isotopes and when the air mass reaches an orographic obstacle, the altitude effect (Gonfiantini et al., 2001) will increase the depletion of this air mass. A modeling study by Herold and Lohmann (2009) suggests that the continentality was dominant in determining the east-west gradient of the isotopic rainfall composition in Africa during the Eemian period.

The isotopic composition of precipitation over a region is also influenced by changes in the source of moisture due to the changes in atmospheric circulation and the seasonality of precipitation (Lewis et al., 2010; Pausata et al., 2011b). Also the

extent of condensation and fractionation undergone by the air parcel along its advection from the source may increase with the distance to the destination, leading to lower isotope values in precipitation derived from more distantly sourced vapor. Model and observational studies have analyzed the variability of isotopes in eastern Africa (Levin et al., 2009; Lewis et al., 2010; Tierney et al., 2011a). Observations (Levin et al., 2009) indicate that the comparatively high observed values of hydrogen isotope composition (δD_{precip}) over eastern equatorial Africa are caused by the enriched moisture originating from the Congo Basin. As such, the CAB serves as an isotopic divide that separates two distinct moisture sources to the region - the Indian Ocean, a relatively depleted moisture source and the recycled, enriched continental moisture (Levin et al., 2009). Likewise, a modeling study by Lewis et al. (2010) concludes that around Lake Tanganyika (eastern Africa) during the HS1, the shift from an Indian Ocean dominated source to a strongly continental and Atlantic-influenced source contributed to the isotope variability through changes in the degree of pre-fractionation and the relative enrichment of the nonfractionating (e.g., during transpiration) continental moisture source. Similarly, Tierney et al. (2011a) argue that the negative δD proxy data anomalies from lake Challa in tropical eastern Africa signify the intensity of the East African monsoon circulation rather than the local amount effect.

It has been shown that the compound-specific stable hydrogen isotope composition (δD values) of sedimentary *n*-alkanes (originating from the epicuticular wax layer of terrestrial plants) can be used for reconstructing past changes in the tropical hydrological cycle (Sauer et al., 2001; Schefuß et al., 2005; Collins et al., 2011; Tierney et al., 2011a). The plant waxes get enriched in deuterium with increased evapo-transpiration, also the soil water gets enriched with the heavier isotope under arid conditions. Thus, the δD values derived from plant waxes correspond to the evaporation-precipitation balance and can be used as a proxy for past changes in

the hydrological cycle. In this study, we modeled the isotope ratios of precipitation using an atmospheric general circulation model. We focus on three past time slices (mid-Holocene, LGM, HS1) to assess the distribution of isotopes over Africa for these time periods with respect to a pre-industrial control run (PI, approximately 1800 AD) and compare our model derived precipitation δD values with leaf-wax δD values. Furthermore, we analyze the climate factors influencing the δD values in the model.

4.3 Numerical modeling setup and experiments

Four time slice experiments for the pre-industrial, mid-Holocene, Last Glacial Maximum and Heinrich Stadial-1 were carried out using the Community Atmospheric Model CAM3.0 (Collins et al., 2006), equipped with stable isotope tracers of water (Noone and Sturm, 2010; Sturm et al., 2010), referred to hereafter as IsoCAM. The model has 26 hybrid levels in the vertical and a horizontal resolution of approximately 3.75° in both latitude and longitude, corresponding to a spectral truncation of T31. The CAM3.0 model is coupled to the Community Land Model, CLM (Bonan et al., 2002). Over land, the isotope ratios are calculated by a simple bucket model as formulated by Manabe (1969) but the fractionation during evapo-transpiration and the effect of different vegetation types on the isotope ratios are excluded. The stable isotopes of water are traced through the hydrological cycle by the same transport processes as for normal water (Noone and Sturm, 2010), with the isotopes fractionating with every phase change.

The boundary conditions (orbital parameters, SST, greenhouse gas (GHG) concentrations, topography, ice-sheets) for each experiment were set according to the PMIP2 protocol (Braconnot et al., 2007). As for control run, a pre-industrial simulation (PI) was conducted with the boundary conditions set as per the PMIP2 protocol. The GHG concentrations and orbital years used for each of the experiments are listed

in Table 4.1. The SST and sea ice datasets for the PI, HS1 and LGM experiments were taken from fully coupled CCSM3.0 simulations (Merkel et al., 2010). The ice sheet extent and topography for the LGM experiment were taken from the ICE-5G ice-sheet topography data by Peltier (2004). The coastlines for the LGM and HS1 experiments were also taken from the ICE-5G reconstruction, and represent a lowering of sea level by 120 m (Fairbanks, 1989). The HS1 simulation uses the same boundary conditions as the LGM simulation in terms of the orbital parameters, GHG concentrations and surface properties. The coupled simulation for HS1 was conducted under the LGM boundary conditions and with a permanent freshwater anomaly of 0.2 Sv distributed over the whole Greenland-Iceland-Norwegian Seas (north of about 65°N) that was not compensated for elsewhere (Merkel et al., 2010). The mid-Holocene simulation was initialized and forced with the SST and sea ice concentration derived from a fully coupled CCSM3.0 run for the mid-Holocene period (Bette Otto-Bliesner, personal communication). The orbital parameters of the mid-Holocene experiment were set to 6 ka BP values, while those for the LGM and HS1 simulations were set to the 21 ka BP values (Berger, 1978).

Table 4.1: The Boundary conditions for each of the experiments

Boundary conditions	Pre-industrial	mid-Holocene	HS1	LGM
CO_2 (ppmv)	280	280	185	185
CH_4 (ppbv)	760	650	350	350
N_2O (ppbv)	270	270	200	200
Orbital parameters (year)	1950	6 ka BP	21 ka BP	21 ka BP
$\delta^{18}O$ surface enrichment (permil)	0.5	0.5	0.88	1.0
δD surface enrichment (permil)	4	4	7.05	8

The initial ocean surface isotope distributions for the LGM and the HS1 simulations were corrected based on the sea level record of Lambeck and Chappell (2001) to incorporate the effect of ice-volume change during these time periods. The LGM simulation was different from the LGM-combined simulation in Tharammal et al. (2013) as the present study incorporates the ice-volume effect on the sea surface composition

of isotopes. The sea surface enrichment of water isotopes was set to 1‰ for δ^{18}O and 8‰ for δD in the LGM simulation. For the HS1 simulation a sea surface enrichment of 0.83‰ for δ^{18}O and 7.3‰ for δD was applied. All simulations were conducted for 35 model years and the last 10 years of each simulation were used for the analysis.

4.4 Results

4.4.1 Comparison to modern observations
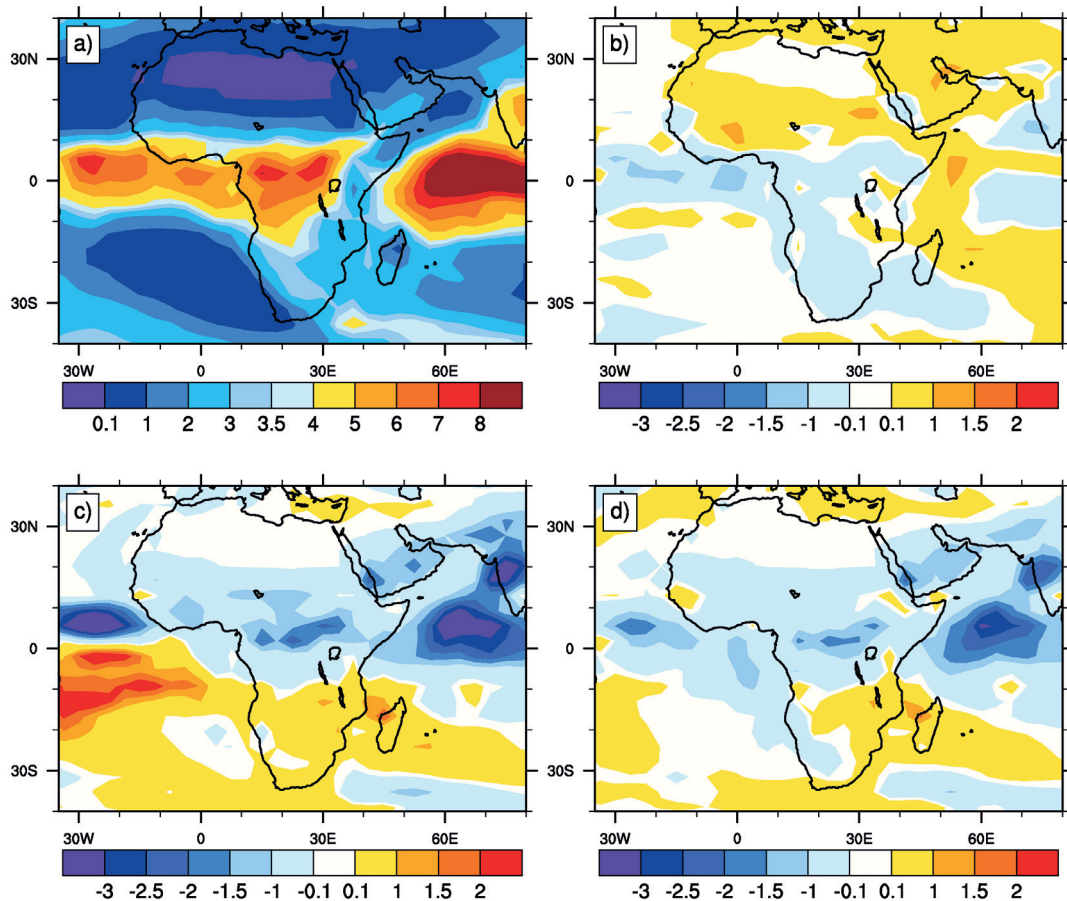
Figure 4.1: Annual mean total precipitation (mm day^{-1}) in Africa. a) Pre-industrial, b),c) and d) respectively are the anomalies of mid-Holocene, HS1 and LGM simulations from the pre-industrial simulation.

The annual mean surface temperature in the PI simulation was found to be lower

than in the observations (CRU data, Rayner et al. 2003) in northern Africa (north of 10°N) by 2°C to 4°C, while in South West Africa (28°S-12°S, 5°E-20°E), the surface temperatures were higher by 1°C to 3°C (not shown). The model in general simulated the precipitation over Africa considerably well for the PI period (Figure 4.1a) but the precipitation over North West (4°N-25°N, 20°W-7°W) and southern Africa (south of 10°S) as well as over the eastern coastal regions were higher by 1-3 mm day^{-1} when compared to the observed modern precipitation (based on the CPC Merged Analysis of Precipitation - CMAP data, Xie and Arkin, 1997, not shown).
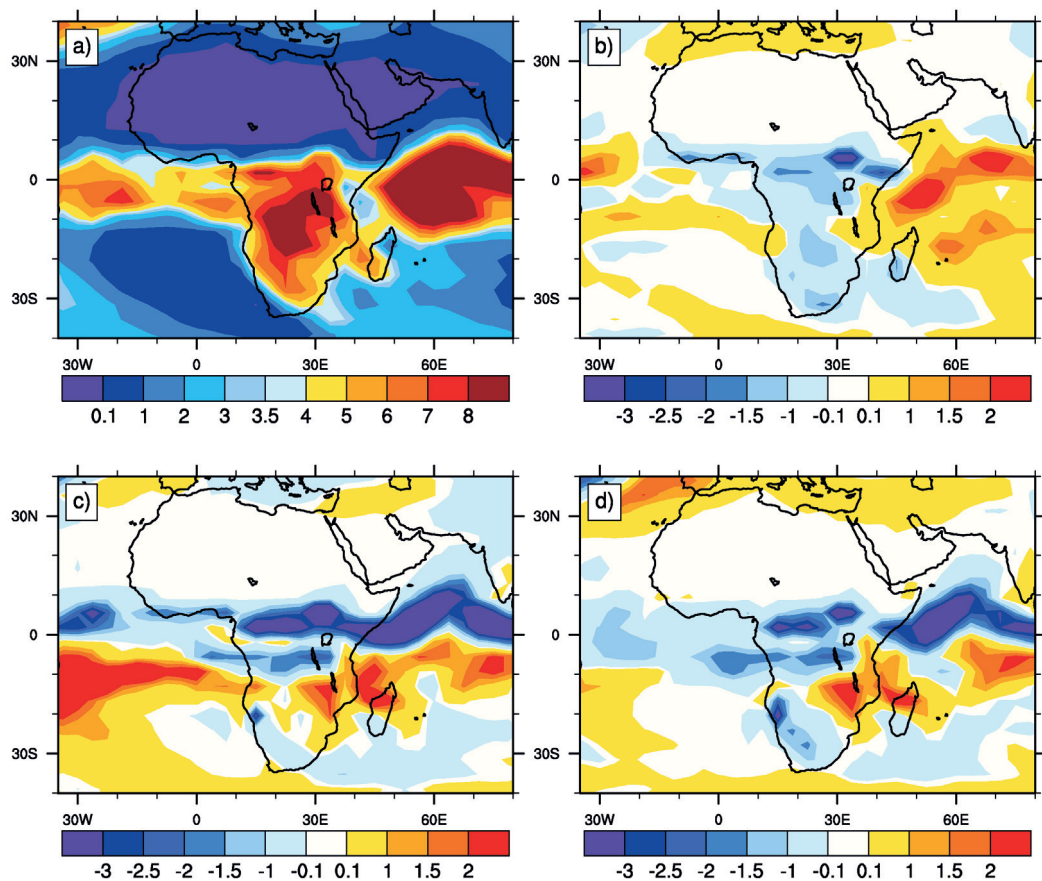
Figure 4.2: Total precipitation (mm day^{-1}) in DJF season in Africa. a) Pre-industrial, b),c) and d) are the anomalies of mid-Holocene, HS1 and LGM simulations from the pre-industrial simulation, respectively.

The precipitation over South West Africa was in good agreement with the observations. The model results for the pre-industrial control run were compared with

the GNIP data for the modern isotope distribution interpolated over Africa (Bowen, 2003). The annual mean δD in precipitation (δD_{precip}, Figure 4.4a) in South West Africa, also large parts of the subtropics and over the Horn of Africa was higher when compared with the observations. Over North West Africa and in the northern subtropics the simulated δD_{precip} values and observations were comparable in magnitude (not shown). The seasonal δD_{precip} pattern in the model for PI (Figures 4.5a, 4.6a) showed lower δD_{precip} values in the summer (rainy season - JJA in Northern Hemisphere) and higher δD_{precip} values in the winter (dry season - DJF in Northern Hemisphere) of the respective hemispheres.
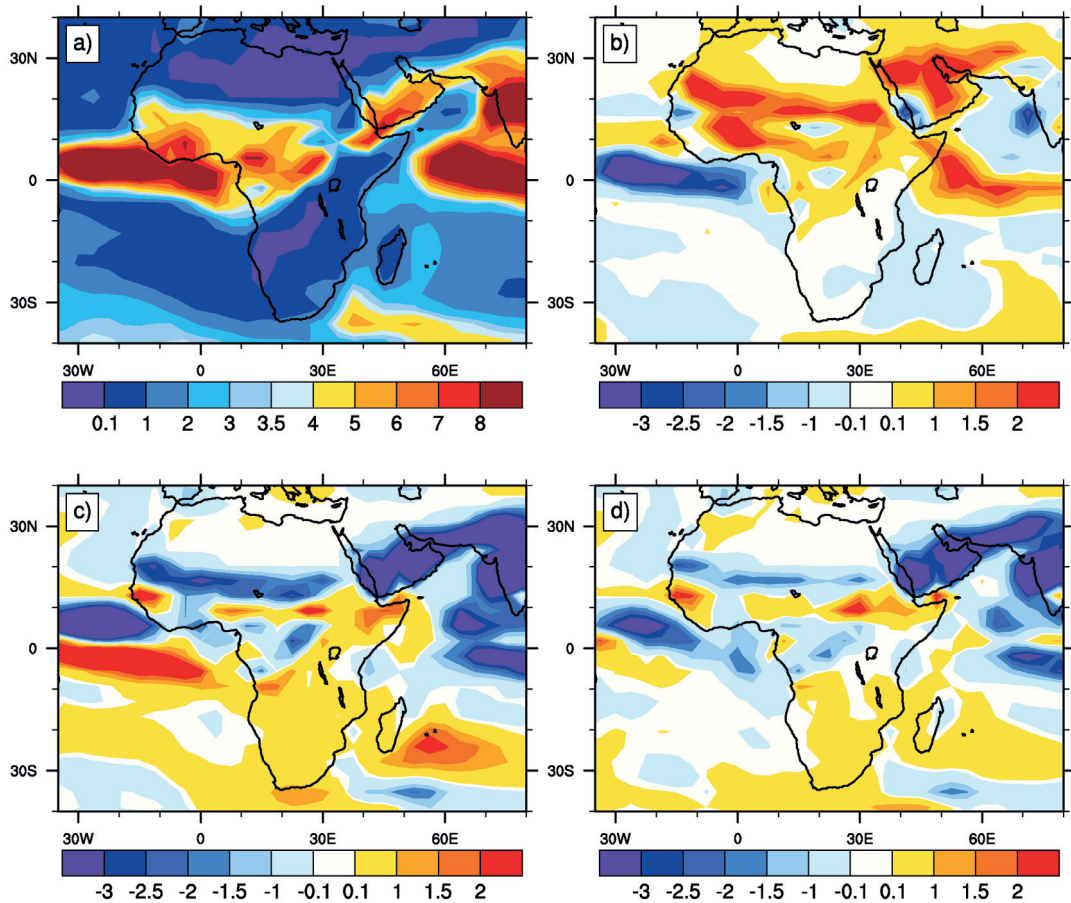
Figure 4.3: Total precipitation (mm day^{-1}) in JJA season in Africa. a) Pre-industrial, b),c) and d) are the anomalies of mid-Holocene, HS1 and LGM simulations from the pre-industrial simulation, respectively.

4.4.2 Spatial anomalies of $\delta D_{\mathbf{precip}}$

The annual and seasonal results of the $\delta D_{\mathrm{precip}}$ values, surface temperature and pre-cipitation simulated in the mid-Holocene, HS1 and LGM simulations were analyzed with reference to the corresponding climate in the PI.
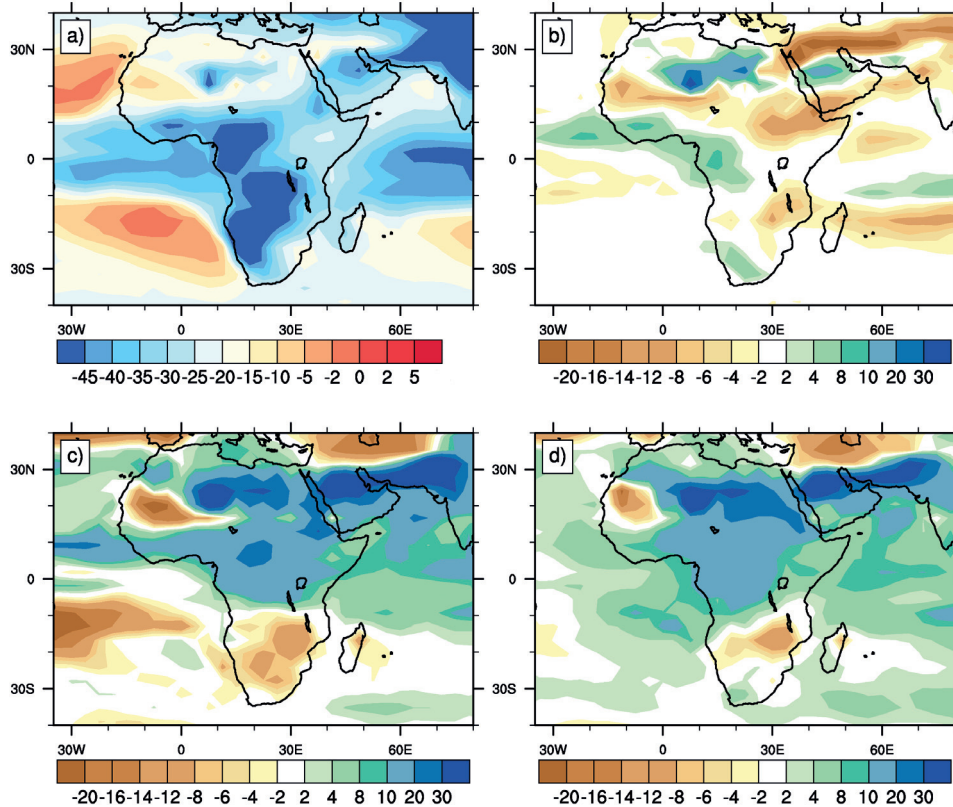
Figure 4.4: Annual mean $\delta D_{\mathrm{precip}}$ (‰) in Africa. a) Pre-industrial, b),c) and d) are the anomalies of mid-Holocene, HS1 and LGM simulations from the pre-industrial simulation, respectively.

In the mid-Holocene, the annual mean $\delta D_{\mathrm{precip}}$ values were lower in northern Africa (Figure 4.4b) when compared to the PI and were related to an enhanced convective activity in northern Africa as diagnosed from the outgoing longwave radiation (OLR) at the top of the atmosphere (not shown) and increased annual precipitation (Figure 4.1b, about 1 mm day^{-1}) over these regions. Reduced annual convective activity

was simulated over Central Africa (15°S-5°N, 5°E-30°E), South Africa and equatorial West Africa, where the annual precipitation was also reduced. During the DJF season, higher δD_{precip} values were simulated in North West and Central Africa (Figure 4.5b).

The winter precipitation (Figure 4.2b) was reduced by 1-2 mm day^{-1} to the south of 10 °N compared to the control run. In the JJA season, δD_{precip} values were reduced by 5‰ to 15‰ (Figure 4.6b) in comparison to the PI in the northern latitudes, similar to the annual mean (Figure 4.4b).
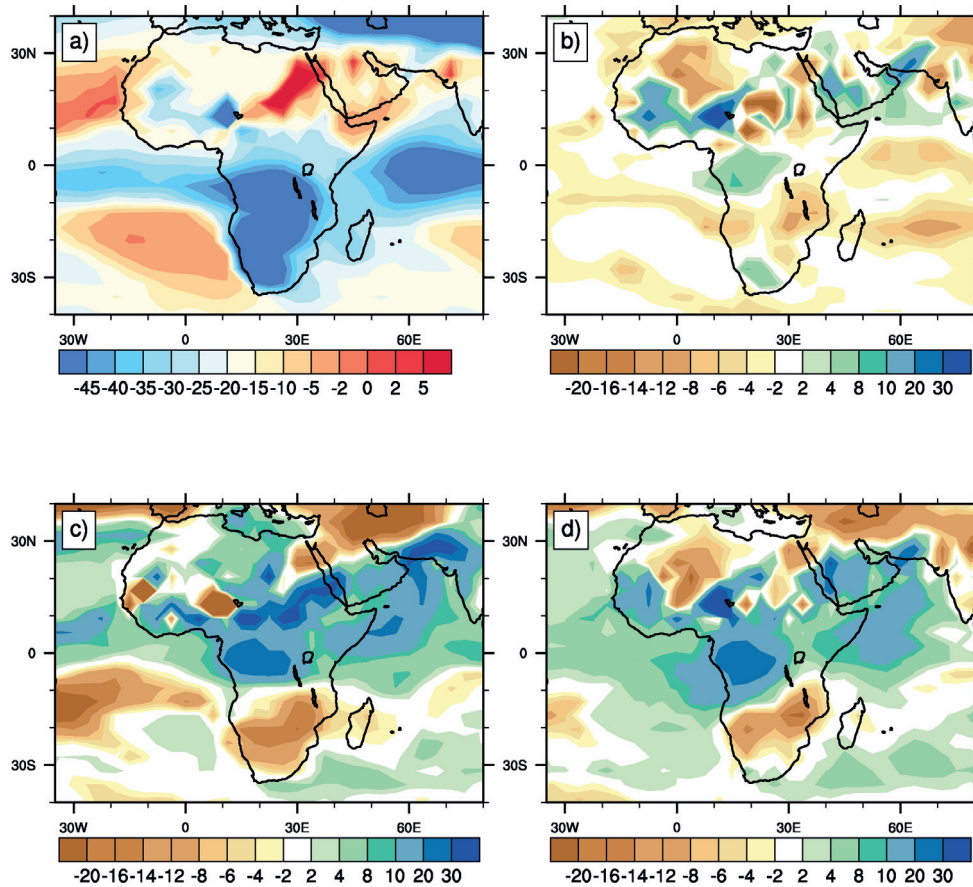
Figure 4.5: As Figure 4.4, but for DJF season.

The boreal summer (JJA) precipitation was also increased over northern and equatorial Africa, as well as Arabia with anomalies exceeding 2 mm day^{-1} (Figure 4.3b). The simulated anomalies of δD_{precip} were higher in the Guinea coastal (0°-

10°N) region in both the seasons and in the annual mean when compared to the PI (Figures 4.4b, 4.5b and 4.6b).
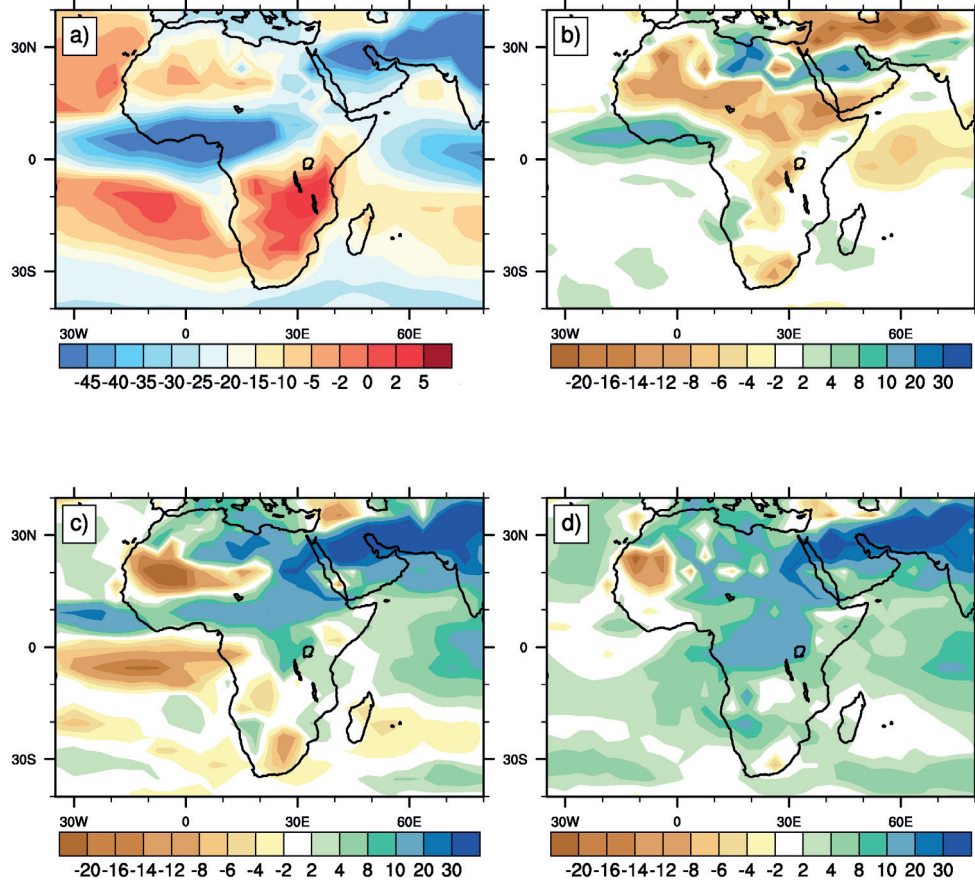
Figure 4.6: As Figure 4.5, but for JJA season.

In the HS1 and LGM simulations (Figures 4.4c and 4.4d), higher annual mean δD_{precip} values (by 10‰ to 30‰) were simulated in northern Africa and lower δD_{precip} values (by 5‰ to 10‰) in southern Africa.

Over southwestern Africa, a reduction in precipitation over the coastal regions between 15°S-30°S did not produce an enrichment over the region during the LGM (Figures 4.1d, 4.4d). In southeastern Africa, lower δD_{precip} anomalies were seen in the regions with positive annual mean precipitation anomalies during both the LGM and HS1 (Figures 4.1c and 4.1d). The major difference between the HS1 and LGM

simulations was a reduction in the annual convection and a reduced precipitation by approximately 1 mm day^{-1} between 5°N and 20°N in the HS1 simulation when compared to the LGM. This was associated with higher isotope ratios in the north when compared to the LGM. In southwestern Africa, the annual mean precipitation was increased during HS1 when compared to the LGM, which was reflected in the lower isotope ratios in HS1. Lower δD_{precip} values in the DJF season of the LGM and HS1 (Figures 4.5c, 4.5d) in southern Africa may be associated with increased austral summer precipitation in the east.

In the JJA season of the HS1 and LGM simulations, higher δD_{precip} anomalies (Figures 4.6c, 4.6d) were simulated in North East and Central Africa, and lower δD_{precip} anomalies were simulated over the northwestern regions between the latitudes of 10°N and 20°N.

4.4.3 Spatial and temporal relationship between δD_{precip} and precipitation

To confirm the links between the precipitation amount and δD_{precip}, a cross correlation analysis at lag 0 was performed using the annual mean data from the last twenty years of the simulation for each experiment. The results of the analysis conducted between annual mean precipitation and annual mean δD_{precip} are shown in Figure 4.7. In North West Africa, a strong inverse correlation between the precipitation and the δD_{precip}, that was significant at the 90% confidence level based on a Student's t-test was evident in the experiments except for HS1; also an inverse correlation between the variables was seen along the eastern coastal regions, which could be interpreted as the amount effect. An inverse correlation between the relative humidity in the lower atmosphere (integrated from the surface to the 700 hPa level) and δD_{precip} was seen over North West Africa in all the simulations (not shown).

The annual mean spatial (the relationship between δD_{precip} and precipitation over
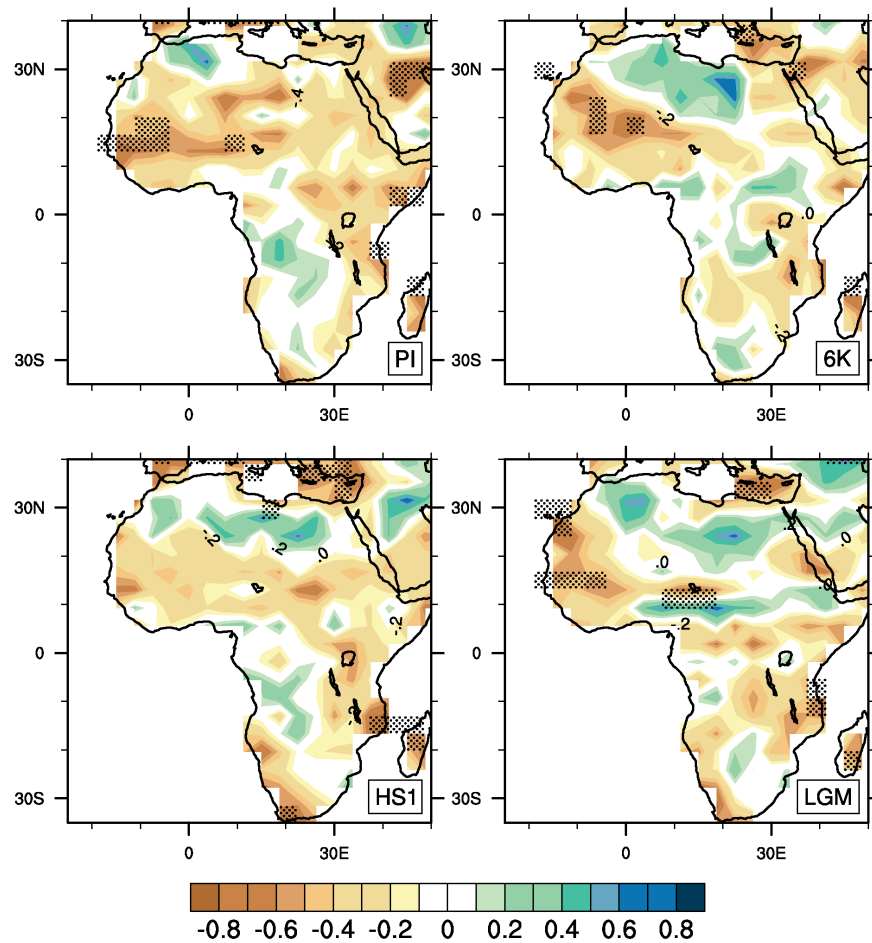
Figure 4.7: Correlation between annual mean δD_{precip} (‰) and annual mean precipitation (mm day^{-1}) in Africa for Pre-industrial, mid-Holocene, HS1 and LGM simulations, respectively. Stippling indicates significant results (p <0.1, Student's t test).

a region) and temporal slopes (the relationship of δD_{precip} with precipitation at a single geographical location through different climates over time) between δD_{precip} and precipitation amount obtained for North West, Central and South Africa are shown in Table 4.2. In North West Africa, the spatial slopes suggested lower δD_{precip} values with an increase in precipitation (amount effect). The temporal and spatial slopes obtained for the HS1 simulation for North West Africa showed similar values (spatial slope 7 % less than the temporal slope, table 4.2), which was nevertheless less than the slopes obtained for the mid-Holocene. In Central Africa, the spatial analysis showed

Table 4.2: Spatial slope between annual mean δD_{precip} and annual mean precipitation amount in the North West (4°N-25°N, 20°W-7°W), Central (15°S-5°N, 5°E-30°E) and South West (28°S-12°S, 5°E-20°E) Africa, in ‰ mm^{-1} day. The temporal slopes (in ‰ mm^{-1} day) calculated for the individual simulations with respect to the control run are given in brackets.

Region	PI	mid-Holocene	HS1	LGM
North West	-5.20±0.53	-4.38±0.41 (-3.09±1.5)	-2.45±0.78 (-2.64±2.9)	-4.03±0.56 (-0.42±3.6)
Central	-0.16±0.85	0.89±0.86 (-3.06±2.13)	4.85±2.04 (-8.56±1.14)	1.99±1.47 (-6.68 ±1.11)
South West	-10.91±2.38	-11.76±2.48 (0.37±3.38)	-9.96±2.56 (3.15±3.10)	-10.70±2.97 (-1.36±3.19)

the lack of a strong relationship between the annual mean δD_{precip} and the annual mean precipitation for the simulations, whereas, the spatial slopes calculated for the JJA season over the region for the three time slices showed a stronger relationship between the δD_{precip} and summer precipitation. Additionally, for the HS1 and LGM climates the temporal slopes showed a stronger relationship between the changes in precipitation amount and changes in the δD_{precip} values with respect to the control run. For South West Africa, the annual spatial slopes obtained were larger compared to the annual spatial slopes obtained for North West Africa, whereas the temporal slopes over the region were more variable than the spatial slopes obtained for all the simulations. It should also be noted that the magnitude of precipitation anomalies for both the HS1 and LGM simulations over South West Africa was smaller when compared to Central and North West Africa. The differences between the spatial and the temporal slopes between the three past climate states may also be related to changes in the seasonality of precipitation, distance from the source and to changes in the monsoon intensity.

4.4.4 Changes in the atmospheric circulation and moisture transport in the simulations

The atmospheric circulation patterns were analyzed in order to assess the variability of the isotope ratios in water vapor with the changes in the atmospheric flow in the individual simulations. The moisture supply for moderate or heavy precipitation is mostly derived from transport, and thus from the convergence of low-level moisture (e.g., Trenberth, 1999; Trenberth et al., 2003). In such regions, the isotopic ratio of precipitation is expected to have a relatively higher contribution from the transported atmospheric moisture than from the local evaporation (Lee et al., 2009). The changes in atmospheric circulation at the 850 hPa level in terms of moisture transport and its convergence are examined in this section, to understand the variability in moisture transport and δD in vapor (δD$_{vapor}$). Furthermore, the anomalies in atmospheric circulation at 600 hPa were analyzed (not shown) to understand the variabilities in the AEJ and related variations in the δD$_{vapor}$ of the individual simulations.

The low-level atmospheric flow patterns in the JJA season of the control run show the major features of the summer circulation, i.e., the easterly trade winds, westerly monsoon flow over Indian Ocean, Indian subcontinent and the Somali jet (Figure 4.8a). The moisture convergence over the CAB and ITCZ are evident in the results (Figure 4.9a).

In the mid-Holocene simulation, the westerly moisture transport from the Atlantic Ocean to the northern coastal regions between 5°N and 10°N was strongly enhanced in the JJA season when compared to the PI, further increasing the moisture convergence over the Gulf of Guinea and NW Africa (Figure 4.9b).

Dominant easterly and northeasterly moisture transport from the equatorial Indian ocean led to an enhanced moisture convergence over equatorial eastern coastal regions. In the mid-Holocene simulation, isotope ratios over North West Africa were
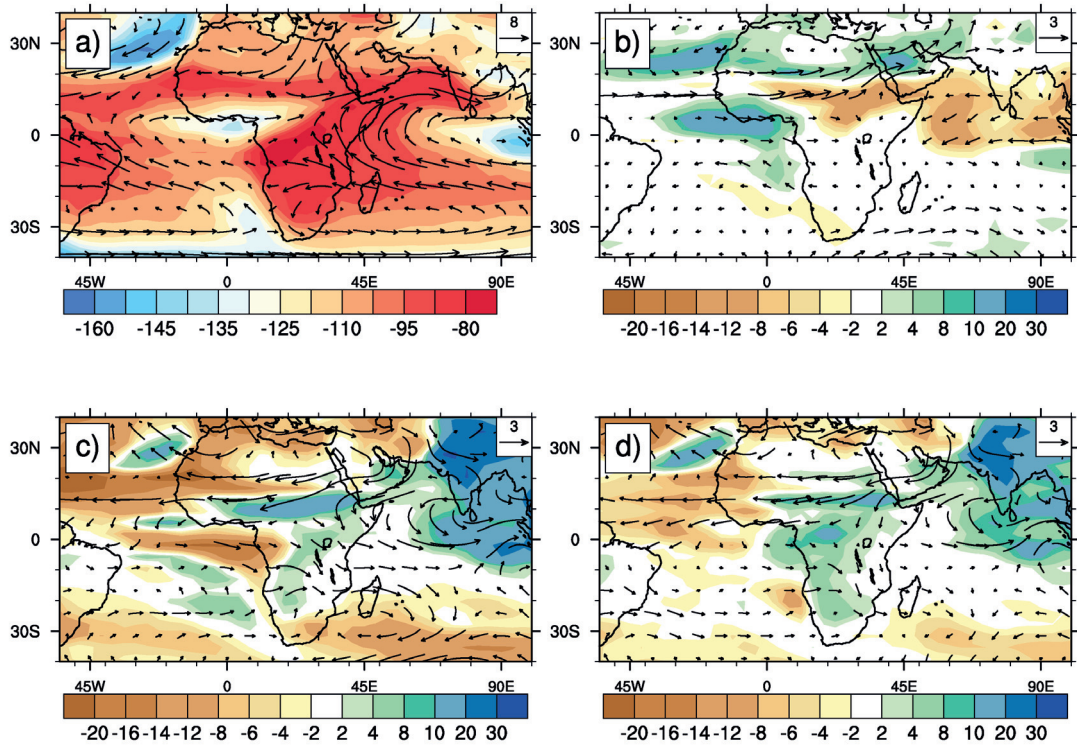
Figure 4.8: Wind (vectors, in m s^{-1}) and δD (contours-shading, in ‰) at 850 hPa level in the JJA season in Africa. a) Pre-industrial, b), c) and d) are the anomalies of mid-Holocene, HS1 and LGM simulations from the pre-industrial simulation, respectively. The wind vectors overlaid in the figure (a) are absolute values, vectors over (b), (c), (d) are anomalies from the PI.

rather high in the water vapor of oceanic origin (by the enhancement of low level westerlies in the 15°N-20°N latitude band) (Figure 4.8b). A weakening of the AEJ was simulated in the JJA season of the mid-Holocene (as seen in the 600 hPa level winds; not shown), and consequently a weaker easterly outflow of moisture increased the moisture content in the region. In addition, the increase in convective activity over northern Africa contributed to the lower δD$_{vapor}$ values seen in the 600 hPa (not shown) level over the region.

In the HS1 and LGM simulations during the JJA season, the moisture transport was dominantly northeasterly in northern Africa and the Sahel as the trade winds strengthened (Figures 4.9c and 4.9d). Furthermore, an increased moisture conver-

gence was seen over North West Africa (Figures 4.9c and 4.9d). The δD_{vapor} was lower in North West Africa in both the HS1 and LGM simulations (Figures 4.8c and 4.8d), where the moisture transport anomalies were dominantly easterly and of land origin. The lower isotope values in the vapor indicate enhanced fractionation during the transport from the northwestern Indian Ocean and reduced contribution from evapo-transpired water from the land. Likewise, increased moisture convergence was simulated in the eastern African coastal regions with increasingly northwesterly moisture transport anomalies and weaker easterly moisture transport from the southern Indian ocean when compared to the PI.
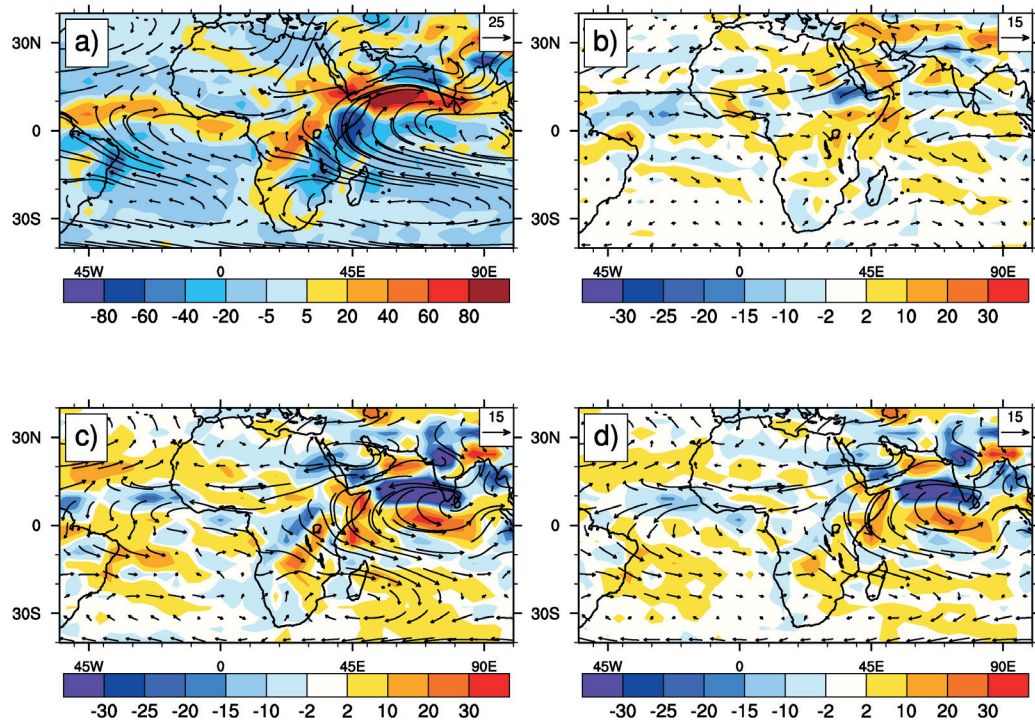
Figure 4.9: Moisture transport (vectors, in g kg^{-1} m s^{-1}) and moisture transport convergence (contours-shading, in $\times$ 10^{-6} g/kg/s) at 850 hPa level in the JJA season in Africa. a) Pre-industrial, b), c) and d) are the anomalies of mid-Holocene, HS1 and LGM simulations from the pre-industrial simulation, respectively. The moisture transport vectors overlaid in the figure (a) are absolute values, vectors over (b), (c), (d) are anomalies from the PI.

In the HS1 and LGM simulations, a reduced moisture convergence was simulated over Central Africa and in the CAB in the JJA season (Figures 4.9c and 4.9d) and the response was more pronounced in the HS1 simulation. This could be because of the reduced easterly moisture transport from the Indian ocean feeding the CAB and the lower SST of the tropical northern Atlantic during the HS1 that led to reduced evaporation thereby moisture content in the air. The extra-tropical westerlies were strengthened over the southern Atlantic ocean and South West Africa, and the moisture convergence in particular for the HS1 simulation, was reduced along the southwestern coast. The reduced moisture transport from the southwestern Indian Ocean and lower δD_{vapor} values over the southern Atlantic (Figure 4.8c) correspond partly to a depleted δD_{vapor} over southeastern Africa in the HS1 simulation.

In the HS1 and LGM simulations, the strength of the AEJ was greatly enhanced (not shown), and the magnitude of easterly moisture transport was increased by 8 g kg^{-1} m s^{-1} to 10 g kg^{-1} m s^{-1} in LGM and 2 g kg^{-1} m s^{-1} to 6 g kg^{-1} m s^{-1} in the HS1, thereby intensifying the transport of moisture from northeastern Africa to the west. Over the Sahel, the moisture convergence at the mid-tropospheric levels was reduced, leading to a drier atmosphere over the Sahel during these time periods.

4.4.5 Comparison of simulated δD_{precip} with leaf-wax δD data

Leaf-wax δD (δD_{wax}) data from 9 cores off Africa (Collins et al., 2013) were compared with the model results. Corrections for vegetation types and ice-volume were applied to the leaf-wax data chosen for the comparison. The corrected δD_{wax} will be denoted by δD_{vc} from now onwards in the paper. The continental catchment areas of leaf-wax bearing material for each core was estimated based on modern-day transport pathways (Collins et al., 2013). Table 4.3 shows the core sites and the catchment area selected for the estimation of δD_{precip} corresponding to each core.

Area-weighted catchment means of different variables (surface temperature, total
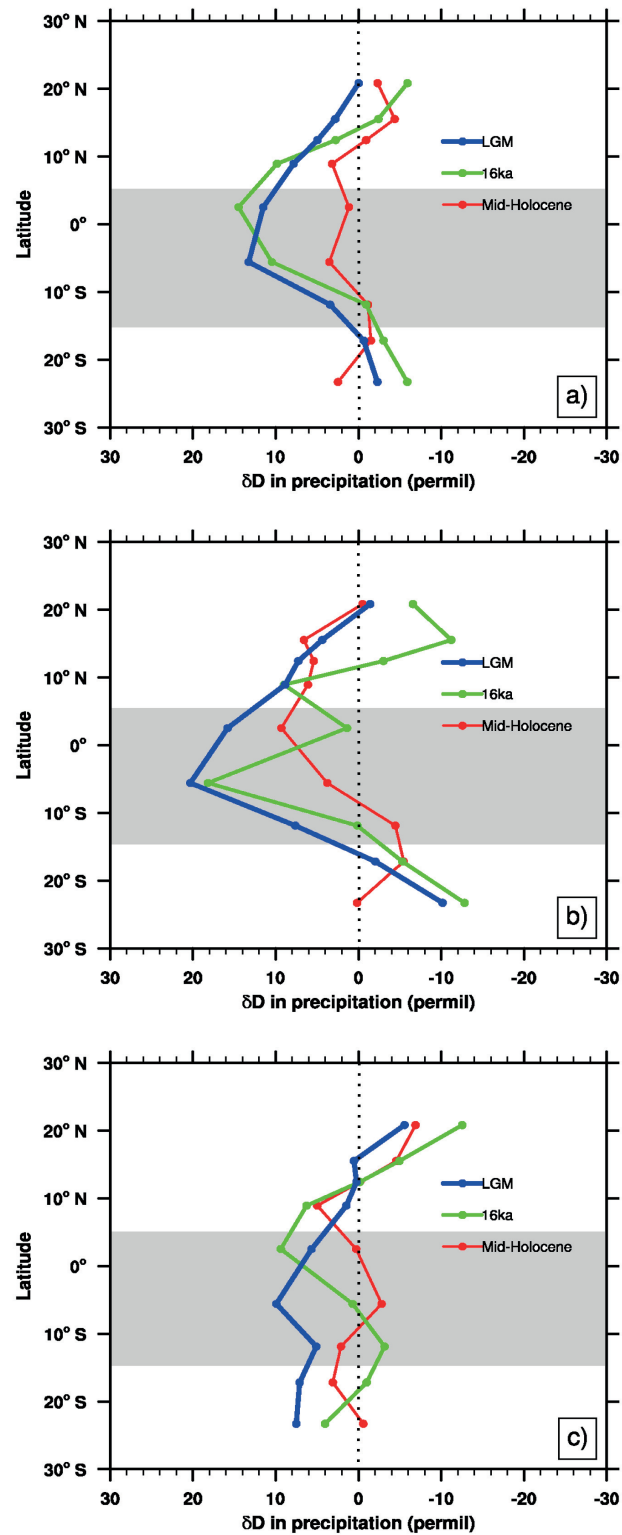
Figure 4.10: Anomalies of catchment mean $\delta D_{\mathrm{precip}}$ (permil) for the LGM, HS1 and mid-Holocene simulations from the PI control run. a) Annul mean, b) DJF seasonal mean, c) JJA seasonal mean.

91

precipitation and δD_{precip}) were calculated from the model results. The annual and seasonal mean anomalies of model-simulated δD_{precip} of the mid-Holocene, HS1 and the LGM simulations from the PI control run are illustrated in Figure 4.10.

The model-simulated annual mean δD_{precip} values for Central and southern Africa (catchment means 5-9) for the PI were highly depleted in comparison with the late Holocene δD_{vc} (not shown). This could be associated with the positive precipitation bias in the model. Nonetheless, the δD_{precip} values simulated around the core locations in North West Africa were similar to the late Holocene δD_{vc}.

Table 4.3: Core locations and catchment basins chosen for the calculations

Core no.	Latitude	Longitude	Area coordinates for the catchment basins
1	20.8	-18.6	25°N-15°S, West coast-5°E
2	15.5	-17.9	20°N-10°S, West coast-5°E
3	12.4	-18.1	17°N-7°S, West coast-5°E
4	8.9	-15.0	14°N-4°S, West coast-5°E
5	2.5	9.4	15.0°N-2.5°S,10°W-20°E
6	-5.6	11.2	5.0°N-10.0°S, West coast-30°E
7	-11.9	13.4	7°S-17°S, West coast-20°E
8	-17.2	11.0	15.0°S-25.0°S, West coast-20°E
9	-23.3	12.4	18.0°S-28.0°S, West coast-20°E

For the mid-Holocene, the leaf-wax isotope anomalies were negative at all the cores (Collins et al., 2013), whereas the catchment basin means of annual mean δD_{precip} in the model showed that the anomalies from the PI were negative for the cores 1,2,3,7 and 8, while positive anomalies were simulated for the catchment basins corresponding to Central (cores 4,5,6) and South West Africa (core 9) (Figure 4.10a). The δD_{vc} anomalies for Central Africa were more comparable to the simulated JJA season anomalies.

For the LGM and HS1 periods, the annual mean model results and δD_{vc} showed positive anomalies in the isotope ratios in the catchment means for basins 2,3,5 and 6 (North West and Central Africa), and the model data was 2‰ to 5‰ greater than δD_{vc}. The leaf-wax data and the simulated anomalies agree on the lower isotope

ratios in South West Africa. However, the depletion produced in the model was less (1‰ to 2‰) when compared to the leaf-wax data (5‰ and 20‰ respectively for the cores 8 and 9). For both HS1 and the LGM, the anomalies inferred from δD_{vc} in southwestern Africa were closer to the simulated anomalies in δD_{precip} of December-January-February (Figure 4.10b) than the anomalies in the annual mean.

4.5 Discussion

4.5.1 δD_{precip} distribution during mid-Holocene

The model successfully simulated the proposed increase in annual precipitation over northern Africa during mid-Holocene as seen in other modeling studies (Kutzbach and Liu, 1997; Joussaume et al., 1999; Braconnot et al., 2000; Otto-Bliesner et al., 2006a) and paleoclimatic archives (Gasse, 2000). Increased summer precipitation in northern Africa and reduced precipitation in the DJF season over tropical and southern Africa were reflected in the annual mean precipitation of the mid-Holocene simulation, where the southern parts showed negative anomalies in the annual precipitation with respect to the PI. The increase in North Atlantic SST in the boreal summer season and related circulation changes also contributed to this simulated change in precipitation. The enhanced lower troposphere westerlies and southwesterlies over northern Africa accelerated the moisture advection from the Atlantic Ocean to northern Africa and the Arabian Peninsula. The model predicted a northward shift in the monsoon extent over Africa (over 20°N). The summer anomalies in precipitation and δD_{precip} for the mid-Holocene were dominant in the spatial distribution of annually averaged δD_{precip} over northern Africa.

Enhanced zonal moisture transport during the boreal summer and increased precipitation over Central Africa and the Arabian Peninsula led to depleted isotope values over these regions due to the isotopic amount effect. The higher annual mean δD_{precip}

values simulated along coastal western Africa could be related to the increase in the relatively enriched moist maritime air flux into inland areas, while a depletion was simulated elsewhere and in northeastern Africa. This was also reported in the study by Herold and Lohmann (2009). They attribute this simulated enrichment in the west and depletion in the east to a shorter time interval from the source (evaporation from the Atlantic), which leads to fewer precipitation events and therefore to less isotopic depletion of the water vapor that reaches the coastal regions. The reason for the isotopic depletion in North West Africa seen in the summer and annual mean distribution of δD_{precip} in the mid-Holocene may be the combined result of continentality and the amount effect (Dansgaard 1964).

The weakened AEJ and increased northeasterly moisture transport from a relatively enriched Mediterranean Sea increased the moisture content in the northern subtropics. This led to a more enriched δD_{precip} seen both in the JJA and annual-mean distribution over the subtropical desert even though the precipitation rate increased (by 0.5-1 mm day^{-1}) and there was a positive correlation between the isotope ratio and precipitation (Figure 4.7b) over the region. The rain re-evaporation (Risi et al., 2010a) near the arid regions in the north also might have contributed to this enrichment. We expect that if a dynamic vegetation model was included, it would enable a positive precipitation feedback. This could improve the simulation of Holocene precipitation over North Africa, and lead to more realistic δD_{precip} values.

4.5.2 δD_{precip} distribution during HS1 and LGM

The model simulated a weaker hydrological cycle with a reduction in annual-mean and summer precipitation in the LGM and HS1 simulations as also seen in fully-coupled modeling studies (Kim et al., 2002; Otto-Bliesner et al., 2006a; Merkel et al., 2010). The presence of large ice sheets in the high latitudes of the Northern Hemisphere and reduced GHG levels led to a cooling of the tropical SST (Bush and Philander,

1998; Weaver et al., 1998; Webb et al., 1997), thus weakening the summer monsoon circulation in these coupled simulations. The predicted reduction of precipitation intensity over tropical and northern Africa are in agreement with the climate proxy records (Yan and Petit-Maire, 1994; Gasse, 2000; Prentice and Jolly, 2000). The monsoonal low-level (850 hPa) cross-equatorial flow off the east coast of Africa and low-level westerlies along the South Asian coastal region were strongly reduced in magnitude in the JJA season of the HS1 and LGM simulations (Figures 4.8c and 4.8d). The differences between each of these experiments and the PI simulation in the circulation and precipitation patterns were also reflected in the δD_{precip} distribution.

During the LGM, the lower land-ocean temperature contrast and subsequent reduction in summer monsoon precipitation over North West and Central Africa produced considerably higher δD_{precip} values than in the control run due to the isotopic amount effect. This is consistent with the finding by Risi et al. (2010b) that weak convective systems produce an isotopically enriched precipitation in dry environments associated with a strong reevaporation of the falling rain. Past precipitation records infer a dry Central and North Africa during the LGM (Gasse, 2000). The enrichment of isotopes over Africa and Asia during the LGM was also reported in previous isotope modeling studies (Jouzel et al., 2000; Hoffmann and Heimann, 1997). Amount of precipitation and δD_{precip} were inversely correlated in the northern tropical latitudes, especially in North West Africa. In the southwestern coastal regions of Africa, the drier and colder continent simulated during the LGM between 13°and 21°S was in agreement with the proxy study by Shi et al. (1998). The absence of a definite linear relationship between the precipitation amount and δD_{precip} over this region in the annual-mean as well as during the wet season may suggest climate controls other than the local amount effect on the δD_{precip} in both the LGM and HS1 simulations.

For the HS1 experiment, a weak anomalous divergence over the tropical southeastern Atlantic (Figure 4.9c) and an increase in precipitation during local winter (JJA,

Figure 4.3c) over southern Africa may be associated with increased mid-tropospheric westerly moisture transport from the South Atlantic, which was warmer than during the LGM. In addition, an enhanced annual convective activity and annual precipitation over a warmer South Atlantic would have contributed to the lower isotopic ratios over South West Africa when compared to the LGM (Figures 4.4c, 4.4d). Again, the seasonal distribution of isotopes in southern Africa during the LGM and HS1 suggests similar signals in both the eastern and western coastal regions. Lewis et al. (2010) also find increased annual precipitation in southern Africa in response to freshwater hosing of the northern Atlantic.

4.5.3 Local and remote controls on the isotope composition

The δD_{precip} in a region is controlled both by local and non-local (remote) processes. Our results suggest that enhanced convection and an increased intensity of summer precipitation led to more negative values of δD_{precip} in North West Africa during the mid-Holocene. An enhanced convective activity leads to more cloud convergence, and since the δD in vapor decreases with altitude, condensate that forms at slightly higher altitude thus will be more depleted (Risi et al., 2008a). In general, the regions of increased convective activity were strongly linked to lower isotope values, as also noted by Risi et al. (2010b). In the LGM and HS1 simulations, a dry and isotopically more enriched water vapor and more enriched rainfall over Central Africa were due to a reduced moisture transport into the Congo basin and a reduced moisture convergence over the CAB, which was in agreement with the findings of Schefuß et al. (2005).

The moisture transport from the western Indian Ocean to East Africa (approximately 10°N-12°S, 30°E-45°E) in both seasons was reduced in the HS1 and LGM simulations, and the anomalies in the moisture transport were mostly westerly or southwesterly. However, the mechanism suggested by present-day studies (Ummenhofer et al., 2009) and proxy-data studies for the HS1 (Tierney et al., 2011b) relates

warm Indian Ocean SST anomalies to such anomalous moisture convergence over East Africa, as they propose that enhanced moisture transport may lead to increased convergence in eastern Africa. The atmospheric dynamics for a wet eastern Africa was similar to the findings of d'Abreton and Tyson (1995).

The increased northwesterly and continental origin westerly moisture transport anomalies possibly contributed to the enhanced moisture convergence over the eastern coasts and led to a lower moisture convergence over the CAB during the LGM and HS1. Reduced evaporation-precipitation rates in the southwestern Indian Ocean in both the simulations ruled out the possibility of an enhanced supply of moisture from the Indian Ocean. Alternatively, modern observations of isotopes in precipitation suggest that the enriched moisture originating from the Congo basin contributes to relatively high observed isotope ratios over eastern equatorial Africa (Levin et al., 2009). Likewise, our results suggest that the enhanced moisture transport from the relatively enriched water vapor over Central Africa and northwestern Arabian Sea to the equatorial eastern coastal regions during the LGM and HS1 (Figures 4.8c, 4.8d) led to the higher $\delta D_{\mathrm{precip}}$ over this region. The lower annual mean and austral summer (DJF) $\delta D_{\mathrm{precip}}$ values for southeast Africa, however were consistent with the local amount effect and in accordance with previous proxy studies that interpret δD_{wax} from the east as a proxy for precipitation intensity (Tierney et al., 2008; Schefuß et al., 2011).

The lower isotope values simulated over South West Africa for the LGM inspite of the reduction in annual mean precipitation (Figures 4.1d and 4.4d) and austral summer precipitation (DJF, Figures 4.2d and 4.5d) indicate the influence of the easterly monsoon strength on the $\delta D_{\mathrm{precip}}$ distribution in this region. For the HS1, in addition to the weaker monsoon, an anomalous westerly/southwesterly moisture transport that brought water vapor with lower isotope ratios from the tropical South Atlantic contributed to the lower isotopic ratios in southwestern Africa when compared to the

LGM.

In general, pronounced anomalies in δD_{vapor} in the mid and lower troposphere, which were either equal or stronger than the anomalies in δD_{precip}, point to the dependence of the isotope ratios on the large-scale atmospheric circulation and variabilities in the advection of moisture.

4.5.4 Model-Data comparison

Generally, the model and the data agree on the enrichment of δD_{precip} in the LGM and the HS1, whereas in the mid-Holocene the model deviates from δD_{vc}, particularly in Central Africa. The increased precipitation bias reported by Yeager et al. (2006) in the standalone CAM3.0 over the African continent and Indian Ocean (Richter and Rasch, 2008) may have contributed to lower isotope ratios in the model when compared to the late Holocene δD_{vc}. The depletion of δD_{vc} in all the core sites during the mid-Holocene was interpreted to be due to an increase in local wet season intensity or increased distance to the moisture source in northern and Central Africa (Collins et al., 2013). Lower δD_{precip} values associated with the simulated enhancement of moisture advection from the North Atlantic and the increased annual-mean precipitation in North West Africa agree with this observation. Contrary to the inference from the proxy data, a reduction in the annual precipitation and a related enrichment was simulated in Central Africa. In addition, the temporal slope between δD_{precip} and precipitation amount suggests a local amount effect. However, the lower δD_{vc} seen in Central Africa compares better to the JJA seasonal anomalies in the model. This could imply that the proxy data records the wet season intensity as suggested in Collins et al. (2013).

The temporal and spatial slopes obtained for the mid-Holocene are consistent with the proposed amount effect in West Africa (Risi et al., 2008a,b). Higher δD_{precip} anomalies when compared to the δD_{vc} anomalies could partially be a result of the lack

of an ocean feedback and thereby a reduced amount of precipitation, partially because of the enhanced advection of relatively enriched moisture from the North Atlantic ocean. The simulated decrease in the annual mean precipitation in the mid-Holocene in southern Africa, except for the southeastern continent was also predicted by other model studies (Tierney et al., 2011a). This could be due to a weaker seasonality of insolation (by 5%) in the Southern Hemisphere during the mid-Holocene, due to the precessional cycle (Berger, 1978). The lack of dynamic vegetation in the model might have reduced the vegetation-climate feedbacks for the mid-Holocene as suggested by other modeling studies (Kutzbach et al., 1996; Shin et al., 2006).

For the LGM, Collins et al. (2013) propose a reduced wet season intensity in West and Central Africa and they interpret the negative δD_{vc} anomaly in South West Africa as an increase in rainout over South East Africa. The model also simulated an increase in the annual precipitation over South East Africa, with the moisture originating from the CAB, but the model results did not show a clear southward suppression of the ITCZ as also suggested by Braconnot et al. (2000). Modeling studies by Kim et al. (2007) and Tierney et al. (2011a) also find an increase in precipitation in South East Africa during the LGM.

Our analysis indicates that δD_{vc} is in fact recording the rainy season, and hence contains a seasonal bias in the signal assuming that the precipitation bias in the model over the region is steady and that the anomalies are robust. Although the addition of water isotope tracers enables model-proxy comparisons, a quantitative comparison of the model results and proxy data would require the model to consistently reproduce the modern precipitation over the region.

4.6 Conclusions

A comprehensive perception of the stable isotope distribution over the African continent is key to a better understanding of the climate change through time over the region, by improving the interpretations of paleo-proxy records. In the present study, we used an isotope-enabled atmospheric general circulation model to simulate the hydrogen isotopes in meteoric precipitation over Africa for the past climate periods - the mid-Holocene, LGM and HS1. Our results indicate that variations of δD_{precip} over Africa were dependent on the precipitation amount and changes in the monsoon intensity. Major variations in annual-mean δD_{precip} were mainly caused by summertime changes in the precipitation amount and possible changes in the isotopic composition of water vapor. Enhanced atmospheric convection and increased summer precipitation during the mid-Holocene produced lower isotope values over northern Africa. We suggest that during HS1 and the LGM, the negative δD_{precip} anomalies over southern Africa were associated with enhanced moisture convergence over East Africa, which in turn was partly due to the changes in the monsoonal circulation and deep convection that led to positive rainfall anomalies. The shift of moisture source to Central Africa and humid Congo Air Boundary from the easterly monsoon circulation led to higher isotope ratios over north and equatorial East Africa. The δD_{precip} and δD_{vc} distributions agree on the higher isotope values over northern Africa associated with lower monsoon intensity. The magnitude of the anomalies derived from the δD_{vc} differ from the model simulated values, but a qualitative comparison between the proxy data and δD_{precip} was feasible. The difference between the spatial and temporal slopes obtained between the climates suggests that the amount effect over a region varies with the changes in climates and that the δD_{precip} values may depend on the shift in sources of the water vapor delivered to the region and on the changes in atmospheric circulation. The results further suggest that the proxy data may be biased towards

the rainy season in the respective hemispheres.

4.7 Acknowledgements

Chapter V

Stable isotopes of water in an atmospheric model: Major features and model evaluation with observations

T. Tharammal, K. Weigel, A. Paul, D. Noone and R. A. Scheepmaker

Abstract

In this study, we modeled the present-day global distribution of stable isotopes of water using an atmospheric general circulation model - IsoCAM. Model results for the isotopes in precipitation were compared against available observations from the Global Network of Isotopes in Precipitation (GNIP). The simulated isotopic composition of water vapor was compared with total column averaged hydrogen isotopic composition of water vapor from the Scanning Imaging Absorption Spectrometer for Atmospheric Cartography (SCIAMACHY). When compared to the observations, the model captures the major effects in the distribution of isotopes in precipitation, such as latitudinal gradients. Overestimations of the surface temperature over the polar regions and of precipitation over the tropics caused major model-data differences. The model satisfactorily simulates the annual mean distribution of total column mean isotopes in vapor, but was found to overestimate the depletion over the convective

regimes, which possibly led to a reversed seasonality over some of the land regions when compared to the SCIAMACHY data. A moist bias in the model possibly contributed to the discrepancies.

5.1 Introduction

The saturation vapor pressure and molecular diffusivity of the isotope species are different from the normal water molecule. Therefore, the fractionation occurring during the phase transitions of water (between vapor, liquid and ice) in the hydrological cycle causes variations of water isotopes in atmospheric water vapor and precipitation (Dansgaard, 1964). The equilibrium fractionation is a temperature dependent process (Majoube, 1970) where a stronger fractionation occurs in a colder temperature and each phase change imprints a certain isotope ratio in the natural reservoirs of water. The fractionation coefficient α defines the degree of enrichment/depletion and is inversely dependent on the surface temperature, a property used in the isotope paleo-thermometry (Dansgaard, 1964; Craig and Gordon, 1965). The lighter molecule is preferentially evaporated and heavier isotopes are preferentially condensed, making the remaining water vapor depleted in the heavy isotope content by a Rayleigh process. The fraction of the vapor remaining in an airmass determines the isotopic composition of precipitation from that airmass (Rozanski et al., 1982).

The stable isotope composition of the water vapor is influenced also by the processes of advection of moisture from remote sources, mixing of atmospheric vapor and evaporation, where each source has its unique isotopic composition (Clark and Fritz, 1997). The major contributor to the isotopes in vapor are oceans, and evaporation over them increases the ratio of heavier isotopes in vapor as, in general, evaporated moisture has a higher isotopic composition than the ambient atmospheric vapor (Merlivat and Jouzel, 1979). During the ascent of the atmospheric watermass

during convection, and subsequent condensation at the lower temperatures at higher tropospheric levels, the remaining vapor gets successively depleted. A progressive depletion of the heavier isotopes in vapor is predicted with the reduction in specific humidity with increasing altitude owing to the Rayleigh distillation (Dansgaard, 1964). Water masses become depleted in the heavier isotopes due to rainouts as they move across the continents and this causes the hydrogen isotopic composition of water vapor over high latitudes and inland of the land-masses to be relatively depleted with the heavy isotopes. Over the higher latitudes, the isotope composition of precipitation gets depleted in the heavier isotopes with decreasing temperature (the so-called "temperature effect", Dansgaard, 1964).

General circulation models (GCMs) fitted with water isotope tracers in their hydrological cycle have been used to simulate the isotopic distribution for the past and present climates. The isotopes of water are incorporated in these models in such a way that the hydrological cycle for the normal prognostic water is duplicated for the isotopologues with isotopic fractionation during the phase changes (Noone and Sturm, 2010). The hydrogen and oxygen isotopic composition of water is expressed as deviations (denoted with δ values in ‰) from the Vienna Standard Mean Ocean Water. For hydrogen isotopes, $\delta D = (R_{SAMPLE}/R_{VSMOW}-1) \times 1000‰$, where R is the ratio of heavier isotope (^2H or 'D') to the ligher isotope (^1H). Apart from the Rayleigh processes, Field et al. (2010) find that postcondensation exchange (PCE) depletes vapor of heavy isotopes, and has differential effects on the isotopic composition of precipitation. They further conclude that during heavy rainfalls, PCE tends to deplete vapor and precipitation of heavy isotopes via atmospheric moisture recycling. Modeling studies by Risi et al. (2008a), Noone and Sturm (2010), and Lee et al. (2008) recognize PCE as the most important factor explaining the "amount effect" (observed inverse relationship between the ratio of heavier isotopes in precipitation and the amount of precipitation over the tropics). Risi et al. (2008a) explain

the amount effect as linked to reevaporation of the falling rain. As hypothesized by Dansgaard (1964), the amount effect is linked to 'fractionation during the rain fall associated with rain reevaporation and diffusive exchanges with the surrounding vapor in the regimes of weak precipitation and the injection of vapor from the unsaturated downdraft driven by rain reevaporation into the subcloud layer in the regimes of strong precipitation' (Risi et al., 2008a). Stewart (1975) suggests that the raindrops are enriched in heavy isotopes when they evaporate at low relative humidity. Lee et al. (2008) conclude that during heavy rains, the larger rain drops take longer to equilibrate with the ambient vapor, and that the isotopic composition of the lower atmosphere becomes depleted as a result of the interaction with these raindrops, where the degree of depletion of isotopes in vapor grows with higher precipitation rates.

Comparisons of the modeled distributions of water isotope ratios in water vapor and in precipitation with observations will help to understand the hydrology and physical processes associated with the fractionation and the isotopic composition of the water cycle and to assess the performance of the models in simulating the global isotope distribution. The Global Network of Isotopes in Precipitation (GNIP), a survey network organized by the International Atomic Energy Agency (IAEA) with the World Meteorological Organization (WMO), has been collecting isotope samples in rain water across the world, and the data are effectively utilized for the studies of hydrological cycle and water resources (Rozanski et al., 1993; Araguás-Araguás et al., 2000). A drawback of the GNIP data is the non-uniformity of the sampling stations and low availability of data over large parts of the oceans. Advancement of satellite spectrometry enable the analysis of the hydrogen isotopic composition of water vapor (δD_{vapor}) (Frankenberg et al., 2009; Worden et al., 2007), which has important applications in understanding the sources of continental precipitation (Rahn, 2007; Berkelhammer et al., 2012b,a). Measurement of isotopes in water vapor is predominant over the sampling of the isotopes in precipitation in terms of availability of

data during the non-rainy seasons and over the deserts. Ground-based networks of spectrometers (e.g. the Total Carbon Column Observing Network (TCCON), Wunch et al., 2011) also have been available since recent times, which, combined with the satellite observations, are effectively used to assess the performance of atmospheric general circulation models in simulating the water isotope composition in the vapor (Risi et al. 2010c, 2012a,b; Yoshimura et al. 2011; Lee et al. 2012). Risi et al. (2012b) find that the combined evaluation of relative humidity and the water vapor isotopic composition facilitate the discrimination of most likely reasons for the moist biases in the GCMs. In this study, we focus on the comparison of the present-day isotope distribution in the model with observational data in both the precipitation and atmospheric water vapor and to distinguish the model-data differences. The seasonality of isotopes in total column water vapor and the seasonal variability of precipitable water over different geographical regions were discussed in detail. On the basis of latest scientific research mentioned above, we investigate how the version of the model that we used for analysis - NCAR Community Atmosphere Model CAM3.0 (Collins et al., 2004, 2006) fitted with water isotope tracers (Noone 2003, referred to as IsoCAM hereafter) compare with the SWING2 model results analyzed in Risi et al. (2012b), since our model differ in the formulations of physics, dynamics and isotopic schemes from the models discussed in their study.

5.2 The model and experiments

5.2.1 The model

The model used for the analysis - IsoCAM - is based on an earlier isotope scheme of Noone and Simmonds (2002), modified with a more advanced treatment of surface exchange and cloud processes to make use of the multiple water phases predicted by CAM3.0 (Noone and Sturm, 2010; Sturm et al., 2010). The spatial resolution

employed in our experiments corresponds to a spectral truncation of T31 and 26 hybrid levels in the vertical. The related Gaussian grid has a spatial resolution of approximately 3.75°(48 grid points in latitude and 96 grid points in longitude). The stable isotope ratios of water in the hydrological cycle of IsoCAM are transported through the atmosphere by the same processes (advection, moist convection, evapotranspiration etc.) used to transport normal water (Noone and Sturm, 2010) and undergo fractionation associated with the phase changes of water. The atmospheric model is coupled to a land model (Community Land Model - CLM, Bonan et al., 2002) at the same resolution as the atmospheric model. The land surface isotope scheme in IsoCAM is limited to a simple bucket model, wherein no distinction is made between bare soil evaporation and transpiration, and evapotranspiration is considered non-fractionating (Manabe, 1969; Noone and Simmonds, 2002). Isotopic composition of the ocean surface was fixed with a constant value of 0.5‰ for δ^{18}O and 4‰ for δD (Craig and Gordon, 1965; Hoffmann et al., 1998). IsoCAM uses a semi-Lagrangian formulation for the water vapor and tracer transport (Williamson and Olson, 1994), without the application of a mass-fixer, and has been found to be sufficiently accurate for conserving isotopic ratios during advection to low temperature environments (Noone and Simmonds, 2002).

The model was run for a total of 20 years in the standard Atmospheric Model Intercomparison Project (AMIP, Gates et al., 1999) style forced with observed sea surface temperature (SST) from the melded HadISST/Reynolds climatology for 1979-2001 (Hurrell et al., 2008). The greenhouse gases concentration, orbital parameters and surface properties of the land model are set to the modern values.

5.2.2   Observational data

GNIP data

To assess the stable isotope composition of precipitation in the model results, we used the long-term annual mean hydrogen isotopic composition of precipitation (δD_{precip}) data from the GNIP database (IAEA/WMO, 2006). The GNIP data span across the records dating back from the 1960's to present day and comprise of the meteorological data from around 800 stations, globally. For the comparison to the model results, the GNIP data were regridded to the model grid. In addition, we added to this data the δD_{precip} data over Antarctica from Masson-Delmotte et al. (2008).

SCIAMACHY

We compared the model results with the satellite δD_{vapor} and total precipitable water products from the Scanning Imaging Absorption Spectrometer for Atmospheric Cartography (SCIAMACHY, Frankenberg et al., 2009) onboard the European Space Agency (ESA)'s Environmental Research Satellite (ENVISAT). SCIAMACHY measures spectra from the UV to the short-wave infrared (2.3 micron). For the δD_{vapor} retrieval a spectral window between 2355-2375 nm is used, which makes the retrieval sensitive to the entire atmospheric column. However, as the scale height of water vapor is small, the lower atmosphere (0-2 km) contributes most strongly to the SCIAMACHY HDO/H_2O retrieval. SCIAMACHY has a spatial footprint of 120 km to 30 km. We used the monthly and annual averages of the years from 2003 to 2005 (published in Frankenberg et al., 2009). The systematic correction of -20‰ in the SCIAMACHY data (Frankenberg et al., 2009; Risi et al., 2012a; Lee et al., 2012) was removed from the data before the comparison with the model results. The data were regridded to the T31 model grid, and the grid cells with more than fifteen points of retrieved δD_{vapor} data were used for taking the mean. The average of the three

years of SCIAMACHY data was used for the comparison to the annual mean total column (weighted by the specific humidity) δD_{vapor} data from the model results. For comparing the seasonal variability in the model, we subjected the SCIAMACHY data to further cloud filtering, by excluding those retrievals from the analysis which had a precipitable water column differing more that 15% from the prior column or which had a cloud fraction exceeding 10%.

5.3 Results

5.3.1 Hydrogen isotope composition in precipitation: Comparison to the GNIP data

The global distributions of annual mean δD_{precip} from the model and the GNIP long term annual mean are shown in Figure 5.1. The modeled δD_{precip} captures the major features of the GNIP observations. The observations and model results show relatively low δD_{precip} values around the polar regions where the "temperature effect" plays the major factor in the distribution of the isotopes, and high values were seen in the subtropics. The lowest δD_{precip} values were found over Antarctica, where the model overestimated the values when compared to the data from Masson-Delmotte et al. (2008). The present-day spatial slope over Antarctica between the surface temperature and δD_{precip} was 4.58‰ $°C^{-1}$, while the slope calculated for the data was 6.34‰ $°C^{-1}$. The polar and subtropical regions where the modeled δD_{precip} values were more enriched than the GNIP results, had a positive surface temperature bias in the model when compared to modern observations (Figure 5.2a; CRU data, Rayner et al. 2003), which possibly led to higher isotope values in these regions.

The δD_{precip} values over the monsoon regions were depleted with the increase in the precipitation intensity ("amount effect"). The spatial slope calculated between the
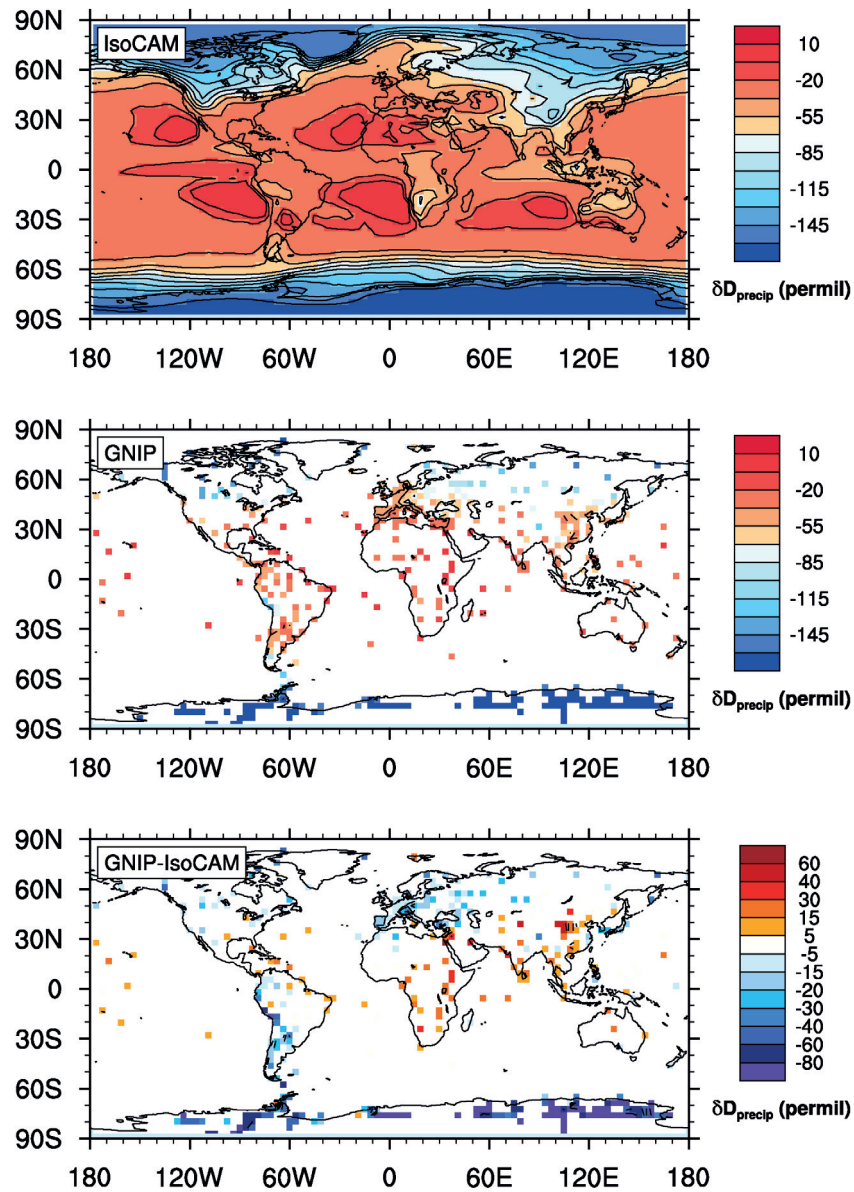
Figure 5.1: The δD in precipitation in (‰). Top: δD$_{precip}$ in IsoCAM, values over Antarctica are from Delmotte et al., 2008, Middle: Long term annual mean GNIP data for δD$_{precip}$, Bottom: The difference between the both (GNIP-IsoCAM).

total precipitation and the δD_{precip} between 20°S-20°N, for all the model grid points was -3.74‰ mm^{-1} day. Continentality, or the "distance from coast effect" where lower δD_{precip} would be observed in the inland regions, was seen over Eurasia in both the data and the model results. In the tropics, especially over Africa and the Indian subcontinent, the simulated δD_{precip} was lower than the GNIP data by 10‰ to 40‰, where the modeled annual mean precipitation exceeded the observed modern precipitation (based on the CPC Merged Analysis of Precipitation - CMAP data, Xie and Arkin, 1997, Figure 5.2b).

(a)

(b)
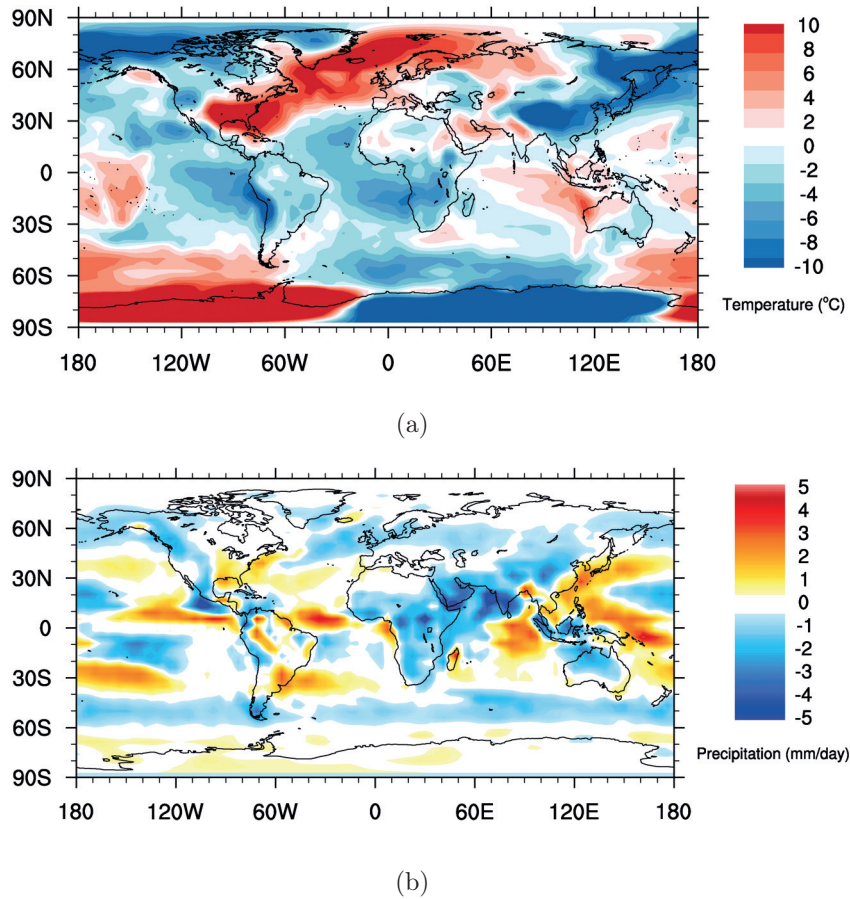
Figure 5.2: The difference of (a) surface temperature in °C, (b) total precipitation in mm day^{-1}, of IsoCAM from the observations (CRU data for the surface temperature, CMAP data for precipitation respectively), given as (observations-IsoCAM).

Above 30°N, the modeled values were higher than the GNIP data by 10‰ to 40‰.

During the boreal summer, modeled δD_{precip} values were higher when compared to the winter in latitudes above 30°N and towards the poles, and the magnitude of the seasonal amplitude varies between 10‰ to 60‰ (not shown). Between the equator and 20°N the δD_{precip} showed lower values in the boreal summer (not shown), especially over North West Africa and the Indian subcontinent where an excessive precipitation during the summer was simulated.

5.3.2 Comparison of model results with satellite data

The total column annual mean of the hydrogen isotope ratio in vapor (δD_{vapor}) of SCIAMACHY for the years 2003-2005 and simulated present-day results of total column annual mean of δD_{vapor} from IsoCAM are shown in Figure 5.3.

The calculated RMSE was 35‰. For both the satellite data and the model results, higher δD_{vapor} values were seen over the lower latitudes similar to those in precipitation, and the values decreased towards the poles. The zonal mean of δD_{vapor} from the model (Figure 5.4a) showed a positive offset of 30‰ to 60‰ from the SCIAMACHY data and both the model and the satellite data showed a decrease in δD_{vapor} values with increasing latitudes ("latitude effect"). Between the latitudes 20°N to 20°S, the differences in the zonal means were in the range of 10‰ to 30‰, and the differences increased further in the subtropics. The spatial distribution of δD_{vapor} had a close relation to the evaporation from the source regions, especially in the subtropics where the higher surface temperature increases the evaporation rate thereby increasing the ratio of heavier isotopes in the water vapor. Over Central Africa, northern South America and southern Asia, simulated δD_{vapor} values were lower than the SCIAMACHY data by 10‰ to 40‰. These regions were identified as moisture sinks in the model, with negative "evaporation minus precipitation, (E-P)" values (not shown), and lie in the intertropical convergence zone (ITCZ). Over these regions δD_{vapor} depends also on the local (E-P) balance.
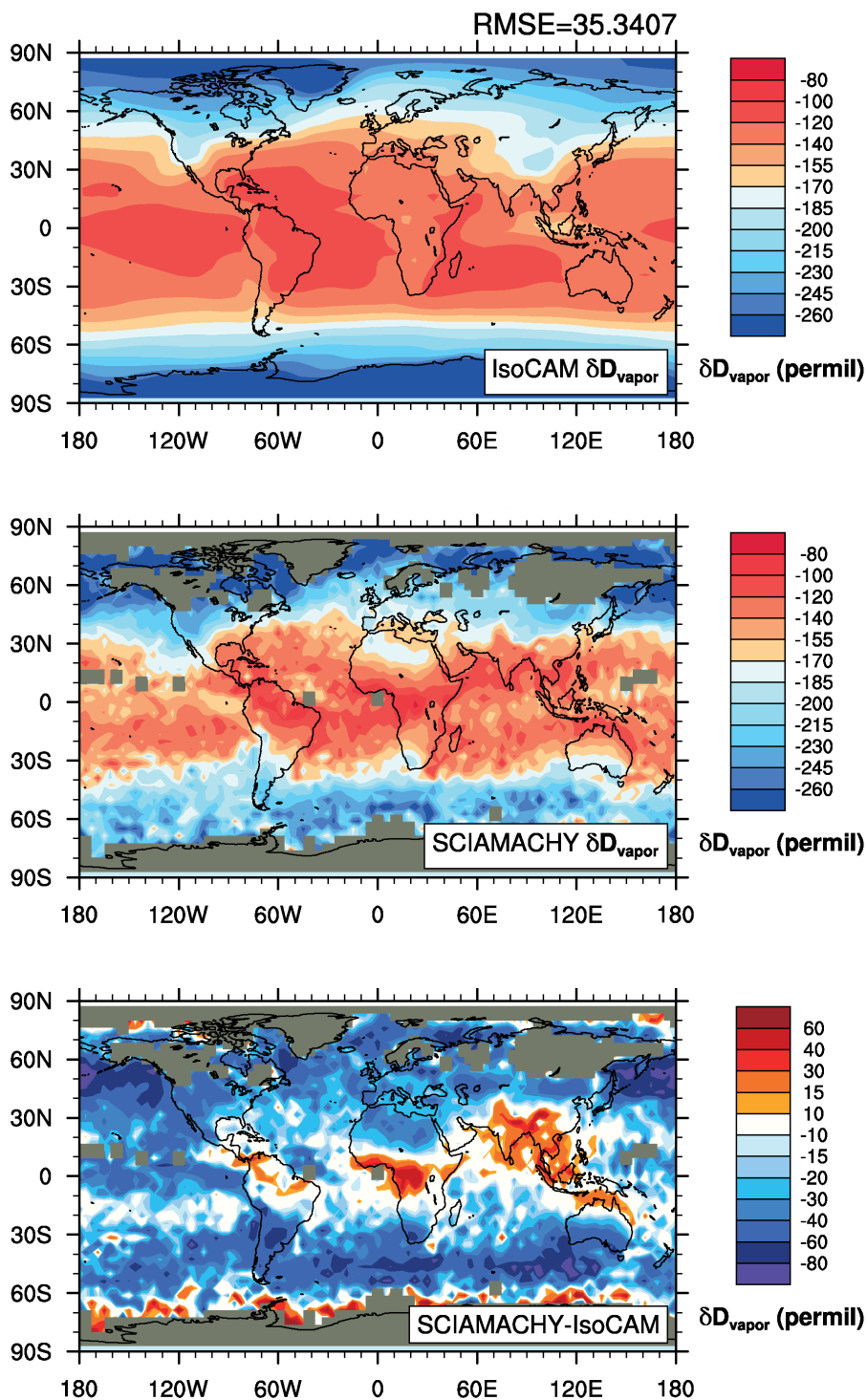
Figure 5.3: Total column annual mean δD_{vapor} in (‰). Top: Total column mean δD_{vapor} in IsoCAM, middle: SCIAMACHY(mean of the years 2003-2005) results for δD_{vapor}, bottom: difference of (SCIAMACHY-IsoCAM)

(a)   (b)
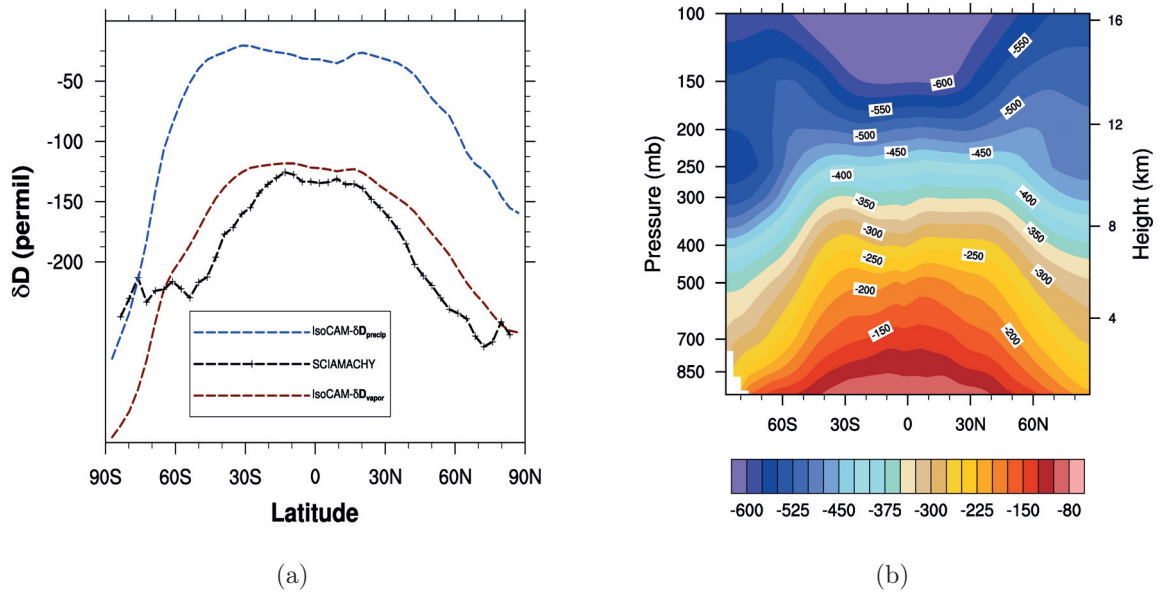
Figure 5.4: Zonal means of annual δD in (‰) in vapor and in precipitation. Left: Total column mean δD$_{vapor}$ and δD$_{precip}$ from IsoCAM results and total column mean SCIAMACHY results for δD$_{vapor}$ averaged over 2003-2005. Right: δD$_{vapor}$ in ‰ at different pressure-height levels from IsoCAM, zonally averaged.

In the subtropics and generally in the latitudes above 30° in both the hemispheres the δD$_{vapor}$ in the model is higher (by around 30‰-40‰) than the satellite data. The vertical distribution of δD$_{vapor}$ (Figure 5.4b) showed that the δD$_{vapor}$ values decreases with height and latitude, as δD$_{vapor}$ is largely determined by the water content and temperature in the different vertical levels.

5.3.2.1 Correlation of δD$_{vapor}$ with total column precipitable water

Figure 5.5 shows the correlation between the annual means of total column mean δD$_{vapor}$ with total column mean precipitable water simulated by the model. Between the 20°N to 20°S latitudes, the total column precipitable water was negatively correlated with the total column δD$_{vapor}$. The tropical ocean regions showed a significant negative correlation between the precipitable water and δD$_{vapor}$. Likewise, over the land regions - North West and Central Africa, northern South America and Australia - significant negative correlations between the δD$_{vapor}$ and total column precipitable
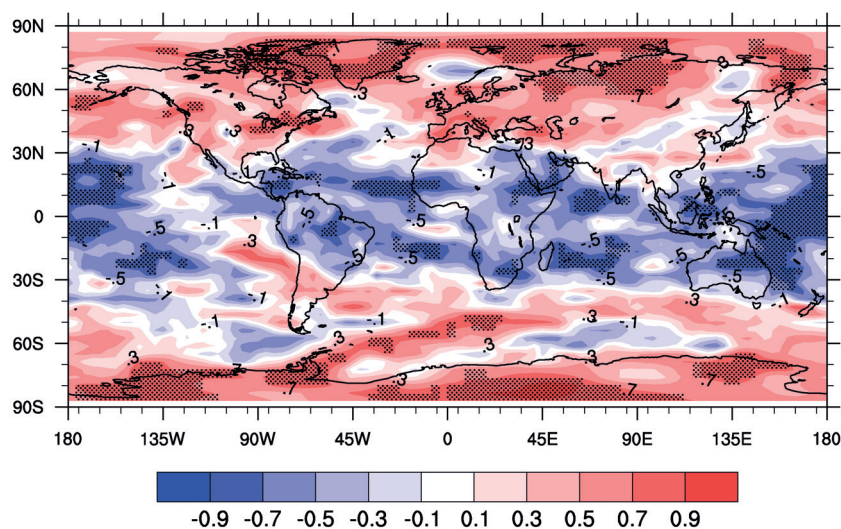
Figure 5.5: Correlation of total column mean δD_{vapor} (annual mean) in (‰) with total column mean precipitable water (annual mean) from the model. Stippling indicates significant results at p <0.05 (using Student's t test).

water were simulated. It may be noted that regions with larger negative correlations coincide with the regions of total column moisture convergence and convection in the results, where the contributions from different vapor sources are important with the local evaporation. Positive correlations were simulated over the mid- and high latitudes (over 30°) particularly over Eurasia and northern North America.

5.3.3   Seasonal cycles of δD_{vapor} and precipitable water

In the SCIAMACHY data, δD_{vapor} was generally more enriched during the local summer season than in winter in each of the hemispheres. Likewise, during the boreal summer (JJA), the total column mean δD_{vapor} in the model results were higher than during the boreal winter (DJF) (DJF-JJA; Figure 5.6) over the mid- and high latitudes. However, the modeled seasonal variations of δD_{vapor} over some regions did not match with the SCIAMACHY observations. Notable of these regions were southeast Asia including the Indian subcontinent (10°N-35°N, 70°E-90°E), Australia (10°S-45°S, 110°E-155°E), and southern Africa (14°S-14°S,5°E-37°E), where a reversed sea-

116

sonality was simulated compared to the SCIAMACHY results (Figure 5.6a). We analyzed the seasonal cycles of δD_{vapor} and column mean precipitable water separately over these regions, along with North West Africa (9°N-25°N, 20°W-30°E) and northern South America (10°N-25°S, 30°E-80°E), regions where the model and the data agreed on the seasonality (Figure 5.7). In these selected regions, we compare the averaged SCIAMACHY data from the gridcells after correcting for the cloud fraction as described in section 5.2.

Additionally, a reverse seasonality was seen in the vertical profile of seasonal variations (DJF-JJA, Figure 5.6b) in the upper troposphere reaching from around 500 hPa to 200 hPa in the 0°- 15°N latitude related to the deep convection zones, and in the near surface vapor (from 10°N to 30°N), probably due a Rayleigh-type rainout process during the wet season, which depletes the water vapor. In the latitudes of 30°and above the δD_{vapor} values are generally higher during the summer of the respective hemispheres.

Among the selected regions, highest δD_{vapor} values were seen over northern South America (Figure 5.7a, 5.7b) in both the SCIAMACHY data and the IsoCAM seasonal cycle and a maximum over the region was recorded during the austral winter season (JJA), with a lower precipitable water measurement over the region in this season (Figure 5.7c, 7d). The simulated δD_{vapor}, precipitable water patterns and their seasonal variability over the region were in reasonable agreement with the SCIA-MACHY observations, even though the model overestimated the precipitable water over the N. S America by 1-3 g cm^{-2}. Sturm et al. (2007) find that the partial reequi-libration of falling raindrops with the vapor and non-fractionating evaporation from the land surface contribute to the higher isotope values over the region during the winter season.

Over North West Africa between 10°N and approximately 25°N, δD_{vapor} was de-creased in DJF when compared to the boreal summer season, both in the model
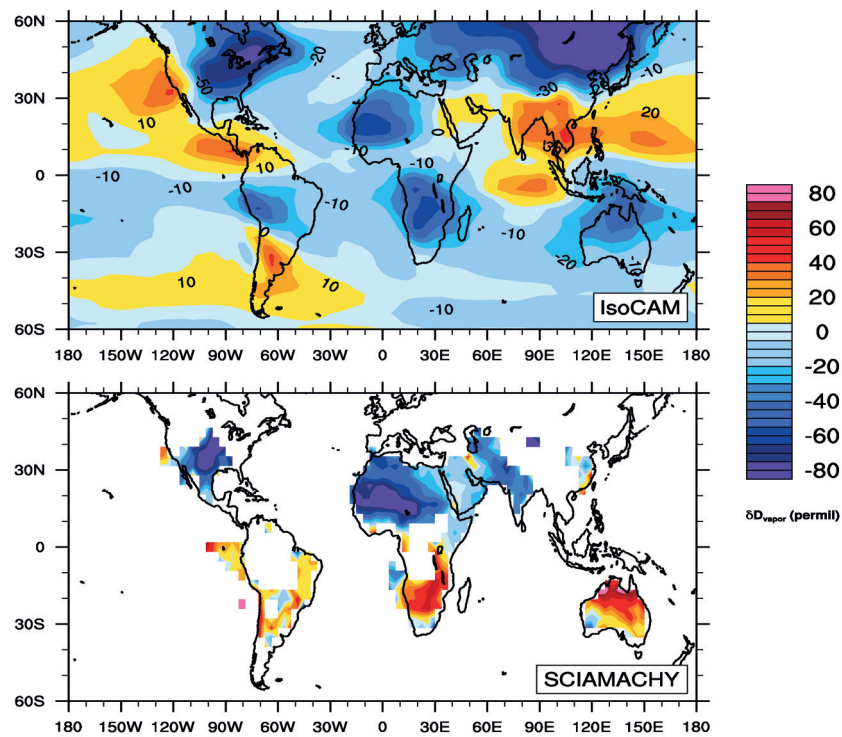
(a)
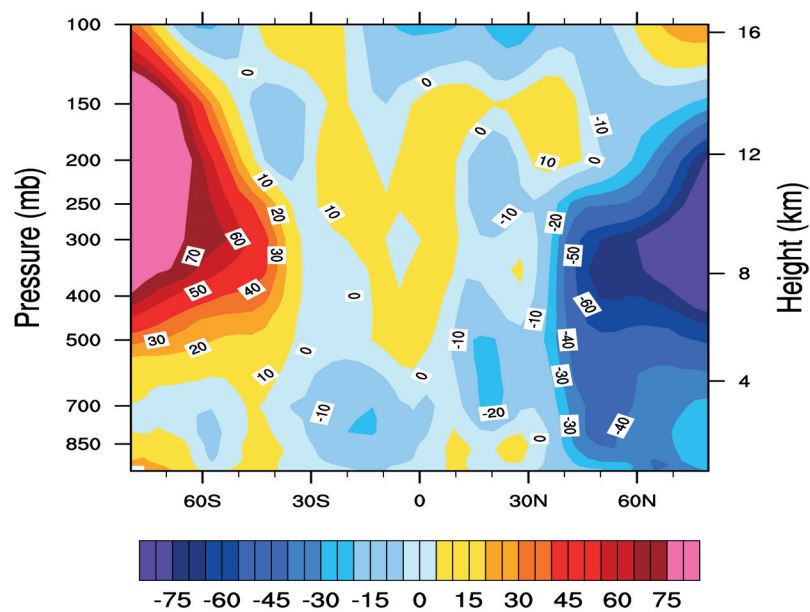
(b)

Figure 5.6: Seasonal variation (DJF-JJA) of total column δD_{vapor} in (‰). (a) Top: IsoCAM, Bottom: SCIAMACHY, (b) same as (a), for IsoCAM results, on the vertical pressure-height levels.

and the SCIAMACHY data. The seasonal amplitude (DJF-JJA) in the model was approximately 20‰ to 40‰, while the amplitude was larger (50‰ to 80‰) for the satellite data, and this could be due to the overestimation of δD_{vapor} values (by 30‰ to 50‰ over the desert) in the DJF season by the model (Figure 5.7a, 5.7b). In addition, the model overestimated the precipitable water over northern Africa during both the seasons, in JJA by $\sim$1-2 g cm^{-2} and in DJF by $\sim$0.5-1 g cm^{-2} (Figure 5.7c).

Over southern Africa, the model and the satellite data differed in the sign of the seasonal amplitudes, where the model results showed lower δD_{vapor} values during the DJF when compared to the JJA season, in contrast to the SCIAMACHY data wherein the δD_{vapor} values during DJF were higher than the JJA. Furthermore, the model exaggerated the depletion over this region in the DJF season by 20‰-30‰ when compared to the satellite data, and the comparison of the model results with CMAP precipitation data showed that the model over-estimated the DJF (austral summer) precipitation over the region by 3 to 4 mm day^{-1}.

For the Indian subcontinent, a reverse seasonality was simulated, similar to that in southern Africa as the model produced positive anomalies of " DJF-JJA " δD_{vapor} (+10‰ to +30‰) whereas the SCIAMACHY data showed negative anomalies in the range of -10‰ to -30‰. In both the model and the SCIAMACHY data, the δD_{vapor} values decreased on the onset of summer monsoon (June, Figure 5.7a, 5.7b), and the model overestimated the depletion by approximately 20‰ to 30‰ for this particular month. The model and the data showed similar δD_{vapor} values for the July and August means, but during the December, January and February months the model under-estimated the depletion when compared to the SCIAMACHY results. The total precipitable water over the Indian subcontinent during JJA was 2 g cm^{-2} to 3 g cm^{-2} higher in the IsoCAM than the SCIAMACHY data, and during DJF the model simulated an excess of precipitable water, by approximately 1 g cm^{-2} compared to the satellite data. Likewise, the precipitation over the region was highly overestimated in
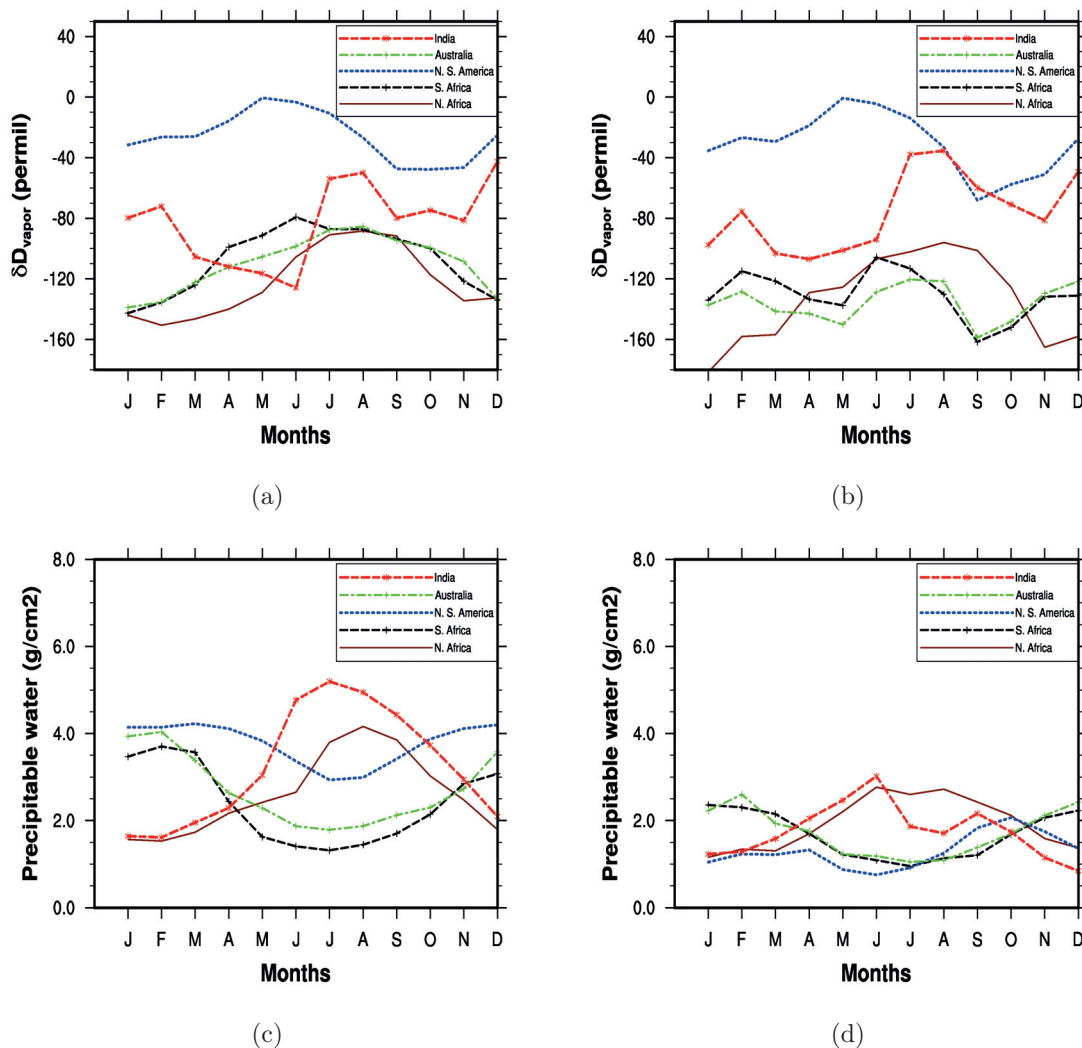
Figure 5.7: The regional monthly means of total column δD_{vapor} in (‰) for (a) Iso-CAM, (b) SCIAMACHY. The values were corrected for cloud fraction >0.1. (c) and (d) are total column precipitable water (total atmospheric water vapor above the Earth's surface) from the IsoCAM and total column precipitable water from the SCIAMACHY, respectively.

the JJA season when compared to the CMAP observations, while the precipitation during the DJF season was slightly underestimated by the model.

Over Australia, another region where the "DJF-JJA" anomalies were negative, the model overestimated the δD_{vapor} values during the austral winter (JJA) season (by approximately 30‰) when compared to the SCIAMACHY data. Furthermore, the

120

model overestimated the precipitable water over Australia by 1-3 g cm^{-2}. However, both in the model and SCIAMACHY results the seasonal difference (DJF-JJA) of precipitable water over the region had the same sign, though quantitatively overestimating the moisture, which may cause the seasonal bias of the δD_{vapor} in the lower troposphere.

5.4 Discussion

5.4.1 δD_{precip} in the model

The major features of the global distribution of water isotopes are well simulated by the model. The comparison with the GNIP data showed that the model was capable of simulating the temperature dependence of isotopes in precipitation in the higher latitudes and the variation of the isotope values with the amount of precipitation in the tropics and the seasonality as studied by Dansgaard (1964). The model successfully reproduced the relationship of the δD_{precip} with the local temperature ("temperature effect", Dansgaard, 1964) for temperatures below 15°C. The depletion over the higher latitudes was underestimated in the model when compared to observations, and this was partly because of a warm bias in the model over the high latitudes. For instance, over Antarctica, the modeled δD_{precip} values were higher than the observations (Masson-Delmotte et al., 2008). This bias over Antarctica was also simulated in other models (Lee et al., 2007; Masson-Delmotte et al., 2008) and is suggested to be partly due to insufficient cloud parameterizations in the models. The model also captured the relationship between the precipitation amount and the δD_{precip} in the tropics. The lower values of δD_{precip} over the tropical monsoonal regimes were closely related to excessive precipitation simulated in these regions during the summer monsoon when compared to the CMAP observation, since the isotopic depletion of water vapor and rainout increases in heavy precipitation events (Vuille et al., 2005).

5.4.2 Comparison of δD_{vapor} with the satellite data

The systematic shift of 20‰ in the SCIAMACHY data (Frankenberg et al., 2009; Risi et al., 2012a; Lee et al., 2012) was accounted for in the data before the comparison with the model results. Despite of this, an additional offset of -20‰ to -50‰ (Figure 5.4a) from the model results was found in the comparison. In this work we focus on possible reasons for the observed differences caused by the model. However, there are also indications of systematic biases in this SCIAMACHY data set as discussed by Scheepmaker et al. (2013).

A reason for this offset could be the more positive values of δD_{vapor} simulated in the model over the subtropics, especially over the land, which was also seen in the δD_{precip} (Figure 5.1c). The correlation coefficient between the total column precipitable water and δD_{vapor} were >0.7 in many regions in the subtropics and over the tropics.
The model simulates the seasonality of δD_{vapor} reasonably well. The model captures the lower δD_{vapor} values over North West Africa during the JJA season compared to the DJF season as observed by Risi et al. (2010c) and was in accordance with the SCIAMACHY results. When compared to the SCIAMACHY data, the model underestimated the seasonality of total column δD_{vapor} over North West Africa as also observed in other GCMs (Risi et al., 2010c; Yoshimura et al., 2011), possibly because of a moist bias in the model, especially during the winter months. However, it should be noted that sensitivity studies by Risi et al. (2010c) suggest that biases in relative humidity or precipitable water may not be always associated with the biases in the isotopes. On the contrary, Frankenberg et al. (2009) put forward the idea that the subsiding branch of the Hadley circulation is drier and hence more depleted in HDO than in the models, and that the underestimated seasonality could be related to the lower variability in total column precipitable water. From our results, it is not very obvious why the model under-estimated the seasonal amplitude when compared

to the satellite data.

Over the low latitudes, δD_{vapor} values during the summer wet season were lower because the vapor gets continuously depleted in heavy isotopes with heavy rainfall, whereas during the dry winter season, the water vapor gets only slightly depleted. The classical explanation of this low δD_{vapor} during the heavy rains in the summer monsoon season as proposed by Dansgaard (1964) is of the preferential condensation of heavier isotopes in the clouds that leads to depletion in the remaining vapor. Furthermore, Rozanski et al. (1993) observed that in heavy rains, the δD_{vapor} and the isotopic composition of precipitation decrease with time due to the continuous isotopic exchange with falling raindrops.

The vertical profile of zonal mean distribution of the seasonal δD_{vapor} difference (Figure 5.6b) implies that these biases were more regional and confined more to the tropics and subtropics in both the hemispheres, but are significant while interpreting the seasonality resolved by the model. Because of the frequent ascending motions in summer (Risi et al., 2012b), IsoCAM simulated higher δD_{vapor} values in the upper troposphere during this season. However, it is not immediately evident why a reversed seasonality was seen in the 30°S - 15°N in the mid- to upper troposphere. Since the Indian monsoon regime is mostly affected by two monsoon seasons per year, the South West (June-September) and North East monsoon (October-January) systems, the misrepresented seasonality of δD_{vapor} in the model may indicate biases in simulating the moisture distributions over this region, as the various sources of moisture in different seasons may also affect the isotope values in the vapor through mixing. For instance, Risi et al. (2012b) suggest that the misrepresentations of the processes in the model, vis. mixing between different air masses, detrainment of condensate, rainfall evaporation, can lead to different biases in the humidity and δD_{vapor}. Besides, the seasonality (DJF-JJA) in the δD_{precip} showed the same sign as that of δD_{vapor}, albeit with different magnitudes. This shows that the isotope values in precipitation were

related to the isotope values in vapor, especially in the lower troposphere. Likewise, a lower winter (DJF) precipitation over most of the land regions in the tropics and subtropical regions when compared to the CMAP observations may have contributed to the relatively enriched winter months in the model when compared to the SCIA-MACHY data. It is known that rain reevaporation during the winter months may also contribute to the enrichment in the light showers (Risi et al., 2012a).

On the other hand, the excessive convective precipitation during the summer months enhances the surface evaporation (Zhang and Mu, 2005), which, in turn, moistens the lower troposphere thereby increasing the moisture bias in the model, even though the seasonal distribution of the precipitable water was well represented in IsoCAM. Furthermore, this intense convective precipitation during the wet season (JJA) which leads to increased isotopic depletion in the vapor may also be associated with the reversed seasonality simulated over Indian subcontinent when compared to the satellite data. Hack et al. (2006) report this precipitation bias in the uncoupled CAM3.0 over most of the Pacific basin, western Indian Ocean, Arabian Sea, and central Africa. Overestimation of precipitable water over the region throughout the year, and especially during the monsoon onset in the month of June, could cause the very low δD_{vapor} during that month. Likewise, the study by Zhang and Mu (2005) recognizes that the deficiencies in the convective parameterizations in the CAM3.0 cause upward motions extending throughout the troposphere and that the positive feedback loop between convection and surface evaporation in the model causes spurious precipitation in the monsoon regions. We suggest that this increased continental rain recycling in the model could lead to further depletion of the heavier isotopes in vapor over these regions (Worden et al., 2007), in addition to the increased convection. Field et al. (2010) also find that the reverse isotopic seasonality in the Asian Monsoon region can be attributed to post condensation exchange, which depletes water vapor and precipitation of heavy isotopes through intensive upstream moisture recycling.

The regions that show the reverse isotopic seasonality in the Southern Hemisphere - northern Australia and southern Africa - have their respective rainy months during the DJF season. Similar to the Indian subcontinent, these regions also showed a systematic overestimation of precipitable water when compared to the SCIAMACHY data, though the seasonal differences in both the observations and the model results had the same sign. According to Brown et al. (2008), convection and condensation are equally important in determining the DJF-JJA value of δD_{vapor} during north Australia's wet season. However, in the rainy season (during the DJF) the model simulated more excessive convective precipitation (>4 mm day^{-1}) over the northern Australia than the CMAP observed precipitation, as also seen in the coupled CCSM3.0 model (Meehl et al., 2006). We suggest that an increased convective activity and condensation in the model during the wet season and reduced precipitation during the winter months when compared to the observations contributed to this reversed seasonality of the δD_{vapor} when compared to the SCIAMACHY data, despite proper seasonal redistribution of precipitable water over the region. For instance, sensitivity studies by Risi et al. (2012b) identify that a moist bias caused by halving the precipitation efficiency in the convective scheme of the LMDZ produces a reversed seasonality in the deep tropics due to very low δD_{vapor} in the convective regions through large scale condensation. Their study also find that a moisture bias in LMDZ produced by an excessive diffusion in the vertical advection scheme produces a lower or even reverse seasonality in the subtropics, as we see in IsoCAM. However, due to inter-model differences in the numerical schemes for the estimation of physical processes and model dynamics, it is not possible to assume the same deficiencies cause the biases in IsoCAM. Sensitivity experiments similar to those carried out by Risi et al. (2012b) combined with testing the model results against observed isotopic data from different tropospheric levels would be required for a thorough understanding of the mechanisms behind the biases in the seasonal isotopic variability in the

model.

5.5 Conclusions

Using observational datasets of isotopes in precipitation and isotopes in water vapor, we assessed the results from the atmospheric model fitted with a water isotope module. The model in general produced the large-scale patterns of the isotopic distribution both in the precipitation and in the total column water vapor. The model overestimated the $\delta D_{\mathrm{precip}}$ over the polar regions due to the warm bias in the model. Convectively active regions over the tropics were characterized by low values of isotopes in both the total column water vapor and in precipitation. The amount effect over the monsoon regions was overestimated in the model, and the total column precipitable water and $\delta D_{\mathrm{vapor}}$ were inversely related over the tropics. The model satisfactorily simulated the seasonal variations observed by SCIAMACHY over most of the oceanic regions and latitudes above 30° in both the hemispheres, while a reverse seasonality when compared to the SCIAMACHY data was simulated over some of the land regions. The model deficiencies in properly simulating the convective precipitation over the tropics and the excessive precipitable water in the troposphere possibly caused the discrepancies between SCIAMACHY and the IsoCAM in the seasonal cycle of total column $\delta D_{\mathrm{vapor}}$ values over the Indian subcontinent and southern Africa.

5.6 Acknowledgements

Chapter VI

Discussions and summary

The main aim of this study was to investigate the environmental factors - both remote and local - that trigger changes in the isotopic distribution in the water cycle and to compare the modeled isotopic distributions in the different time slice experiments of the past with selected proxy records. IsoCAM - the NCAR CAM3.0 atmospheric GCM fitted with an isotope module in its hydrological cycle - was used to conduct these experiments and diagnose the results of the sensitivity and paleo-climate time-slice studies. Efforts were taken to validate the present-day results to compare with the most-recently available observational satellite and station data, thereby facilitating the understanding of the robustness as well as the possible biases in the results.

6.1 Environmental factors exerting maximum influence on $\delta^{18}O_{\mathbf{precip}}$

In the first part of the thesis (Chapter 3), the boundary conditions influencing the global $\delta^{18}O_{precip}$ during the Last Glacial Maximum (LGM, 21 ka) were investigated. The LGM is an important time period concerning the paleoclimate studies as the boundary conditions and climate responses to them are relatively well known (Braconnot et al., 2007; IPCC, 2007). It differs from the present-day climate in terms of

the surface albedo and topography changes due to the presence of ice-sheets, lower green-house gas concentrations and lower SST. The study finds that the change in topography due to the presence of ice sheets over North America (mainly the Laurentide ice sheet) and changes in SST were the predominant factors that influenced the $\delta^{18}O_{precip}$. The results underline the importance of the altitude effect (cf. section 1.2) and the changes in atmospheric circulation due to the change in topography that brings significant lowering of $\delta^{18}O_{precip}$ over the elevated ice sheet topography in the sensitivity experiments. To sum up, the albedo and topography of the ice-sheets have a local effect on the surface temperature and precipitation, and the distribution of $\delta^{18}O_{precip}$ appears to be influenced by these local changes in surface temperature. These two factors also bring changes to the seasonality of the isotope distribution in the northern hemisphere due to the changes in the atmospheric circulation and changes in the seasonal temperature. The effect of reduced GHG concentrations on the climate was reflected in the reduced LGM SST. The higher summertime $\delta^{18}O_{precip}$ values produced over the tropical monsoon regions in the SST and LGM-combined simulations are also an evidence of the dominance of the rainy season in the annual signal and of the relative importance of SST in the distribution of $\delta^{18}O_{precip}$ over the region. A weak monsoon and reduced rain-out, thereby a lesser fractionation of the water vapor from the source to the monsoonal regimes over South East Asia, might also contribute to this higher $\delta^{18}O_{precip}$ values. Pausata et al. (2011b) similarly find that changes in the Indian Ocean SST alone lead to a decrease in precipitation over the Indian Ocean and subcontinent, hence producing higher $\delta^{18}O_{precip}$ values over southern and eastern Asia.

In summary, when compared to modern conditions, the ice sheets caused a significant reduction in the contribution of moisture from North America. Over Greenland, the absence of a distinct seasonality in precipitation in the results under PI as well as glacial conditions due to a possible bias in the model led to similar spatial and

temporal slopes in the LGM-combined and PI simulations. Nevertheless, the major inter-model differences in the temporal slopes over Antarctica and Greenland (cf. Werner et al., 2001) suggest a model-dependence of the calculations of the slopes, which assert the need for further inter-model comparisons.

6.2 Time slice experiments to compare the proxy archives

In the second part of this thesis, the spatial distribution of hydrogen isotopes in Africa during three important past climate periods - the Last Glacial Maximum (LGM, 21 ka), Heinrich Stadial-1 (HS1, 16-18 ka) and the mid-Holocene (6 ka) - was investigated. Tropical African climate is closely related to the Inter-Tropical Convergence Zone (ITCZ) and the tropical rainbelt, the intensity and location of which supposedly varied with the climate-changes in the high latitudes (Gasse, 2000) and the sea-surface temperature (SST) variations in the Northern Atlantic and Indian Ocean (deMenocal et al., 2000). Stable isotopes of hydrogen derived from plant leaf waxes have been used as a proxy to reconstruct the past climates over Africa, as the hydrogen isotopic composition of meteoric water and relative humidity influence the δD_{wax} (Sauer et al., 2001; Collins et al., 2013). In turn, in the monsoon domains, the ratio of isotopes in precipitation is mostly related to the amount of precipitation (Risi et al., 2008a). Accordingly, the results suggest that enhanced convection and an increased summer precipitation led to more negative values of δD_{precip} in North West Africa during the mid-Holocene. A weakened monsoonal precipitation, thereby lower fractionation and a reduced transport of moisture from the southwestern Indian ocean during the LGM and HS1 plausibly contributed to the higher isotope values over eastern Africa. The anomalies of δD_{precip} over south western Africa related more to the changes in the moisture advection from the South Atlantic Ocean, which was colder during both the

LGM and HS1, than to the local (continental) effects (i.e. rainfall recycling) on the isotopes. From the results, it is very likely that the changes in the isotope values of the sources of moisture, and increased seasonality with the reduced summer monsoon along with the changes in local precipitation, indeed caused to the changes in the isotope distribution over Africa during the LGM and HS1. The results indicate that the changes in moisture sources during the LGM and HS1 caused variations in the isotopic distribution over Central Africa, as also seen in the water hosing experiments by Lewis et al. (2010). The distributions of δD_{precip} and δD_{wax} values agree on the higher isotope values over northern Africa associated with lower monsoon intensity. The magnitude of the anomalies derived from δD_{wax} differ from the simulated values, but a qualitative comparison between the proxy data and δD_{precip} was feasible. The difference between the spatial and temporal slopes obtained between the climates suggests that δD_{precip} values may depend on the shift in sources of the water vapor delivered to the region and on the changes in atmospheric circulation. Water tagging experiments as used in Lewis et al. (2010) would be helpful to differentiate the source effects on δD_{precip}.

6.3 Model performance in reproducing the features of present-day water isotope distribution

The model results were compared with the observations of the isotopes in precipitation and with total column averaged δD_{vapor} from the Scanning Imaging Absorption Spectrometer for Atmospheric Cartography (SCIAMACHY). The model indeed reproduced the large-scale patterns of the isotopic distribution both in the precipitation and in the total column water vapor, although systematic shifts of the isotope values between the model and satellite data were found. The relationships between the isotopes in precipitation and to the surface temperature/precipitation amount were

consistent with the temperature effect in high latitudes and amount effect in the tropics, respectively.

A reverse seasonality in the δD_{vapor} values of the model results over the tropical convective regions when compared to the SCIAMACHY data signifies possible model biases in both the isotope scheme and in the hydrological cycle. In the tropics, Brown et al. (2013) find that the water source is dominated by convective detrainment and postcondensational exchange. Therefore, an increased convective activity and condensation in the model during the wet season and reduced precipitation during the winter months when compared to the observations plausibly contributed to this reversed seasonality of the δD_{vapor}, despite proper seasonal redistribution of precipitable water over the region. For instance, sensitivity studies by Risi et al. (2012b) identify that a moist bias caused by reduced precipitation efficiency and also by an excessive diffusion in the vertical advection scheme produces a lower or even reverse seasonality in the tropics and subtropics, as we see in IsoCAM. However, due to inter-model differences in the numerical schemes for the estimation of physical processes and model dynamics, it is not possible to assume that the same deficiencies cause the biases in IsoCAM. Such sensitivity experiments combined with testing the model results with observed isotopic data from different tropospheric levels would be required for a thorough understanding of the mechanisms behind the biases in the seasonal isotopic variability in the model. In addition, it should be taken into account while comparing the satellite data, that seasonal and selectional biases will be present in the SCIAMACHY data as well, since the satellite can not measure the data at all times and in all the regions equally well due to the presence of clouds or if the sun is very low (e.g. in local winter at higher latitudes). Likewise, studies with conceptual models (Noone, 2008) and satellite observations (Worden et al., 2007) suggest that some biases in simulating the isotopes in hydrological cycle are due to a lack of accounting for air mass mixing that introduces a non-Rayleigh isotope variability,

and from problems with correctly specifying the detailed cloud physics. Taking all these points to consideration, it is suggested that model deficiencies in reproducing the hydrology along with the parameterizations of isotopic exchanges plausibly led to model-data differences for isotopes in water vapor and precipitation.

6.4 Conclusions

The following conclusions were reached from the sensitivity experiments (Chapter 3) and the time-slice experiments for the past with comparison to proxy data (Chapter 4) and present-day isotopic distributions (Chapter 5) in regard to both the water isotope composition of precipitation and atmospheric water vapor.

- The changes in topography due to the large continental ice sheets and the changes in SST were the two predominant factors determining the distribution of oxygen isotopes in precipitation. The altitude effect and the changes in atmospheric circulation brought about by the LGM topography led to a depletion of $\delta^{18}O_{precip}$ in the high latitudes of the Northern Hemisphere.

- The local relationships of the isotope distribution in precipitation with surface temperature in the high latitudes and precipitation amount in the tropics change with climate. However, the results suggest that this difference between spatial and temporal slopes can be model-specific and associated with the simulated seasonality of precipitation, for instance, over Greenland.

- Changes in seasonality of precipitation and large-scale circulation caused variations in the distribution of isotopes over Africa. The δD_{precip} results for the different time-slices experiments agree with the δD_{wax} data qualitatively, thereby reaffirming the application of δD_{wax} as a proxy for past precipitation.

- Model deficiencies in properly simulating the surface temperature and convec-

tive precipitation along with the parameterizations of isotopic exchanges led to model-data differences of isotopes in water vapor and precipitation.

6.5 Outlook

The study reaffirms the use of stable isotopes as an indicator of ambient climate and the potential uses of modeling paleoclimate distribution of the isotopes. Nevertheless, inclusion of isotope tracers into the water cycle of earth system models with chemistry and ecosystem subcomponents will substantially improve the current understanding of the distribution of isotopes in past climates. Furthermore, use of a coupled model assures consistent simulation of the natural climate variabilities and assimilation of the feedback from different components of the model (for example, ocean-atmosphere-land feedbacks). For instance, these feedbacks may significantly improve the representation of the mid-Holocene or glacial climate, where large changes in general circulation and hydrological cycle are evident from the proxies. Another advantage of coupled models is that the isotope ratio of the carbonate shells can be directly compared to the model results, as shown by, for example, Schmidt et al. (2007). As an immediate step towards coupled models, Krandick (2013) used the stable isotope composition of precipitation and humidity from the IsoCAM results as a boundary condition to simulate the distribution of stable isotopes of water in the pre-industrial ocean, using the ocean general circulation model MITgcm fitted with water-isotope tracers.

It has been evident from the results that many of the regions with largest model-data discrepancies are associated with regions where the model has particular biases in resolving the temperature or hydrology, which are related to deficiencies in simulating the large-scale circulation, problems with convective precipitation and a poor representation of surface hydrology, as also noted by Noone and Sturm (2010). Reducing these model biases may also lead to the improvement of the isotope distribution.

However, Noone and Sturm (2010) suggest that an inadequate representation of post condensation exchange (Field et al., 2010) in the isotope schemes can cause differences in the isotopes in atmospheric water vapor even if the isotopes in precipitation are simulated accurately. Therefore, advanced cloud isotope schemes with more detailed cloud microphysical exchanges apart from the bulk microphysics used in IsoCAM are expected to improve the isotopes in vapor. Additionally, validating the present-day model results against the satellite data available at different tropospheric levels (TES data, Worden et al., 2007) will assist in understanding the model-data differences in isotopes in water vapor, distinguishing the reasons for these differences.

At present, the isotopes in the land schemes are limited to simple bucket-models like in this study, but experiments using land surface models with isotope physics (Yoshimura, 2004; Yoshimura et al., 2006; Henderson-Sellers, 2006) have shown that physical treatments of isotopes in the land-surface processes have a large impact on the isotopes in precipitation over mid- to high- latitudinal continents. Therefore, inclusion of a detailed isotopic schemes in the land models would enhance the robustness of the model results and possibly widen the prospects of a comparison of model results with the continental-bound proxies. The coarse model horizontal resolution (T31) chosen for the experiments is expected to cause spectral truncation of orography and could lead to smoothing of topography and relief. This can affect the prediction of small-scale features and to possibly lower the resolution of detailed patterns of distribution of isotopes in mountain ranges, for example, over the Tibetan plateau where the model produced larger differences from the observations. In addition to finer horizontal resolutions, a modeling study by Werner et al. (2011) finds that a combined increase of both the horizontal and vertical model resolution yields a further improvement of the present-day isotopic distribution due to improved simulations of large-scale moisture transport.

Bibliography

Bibliography

Araguás-Araguás, L., Froehlich, K., and Rozanski, K.: Stable isotope composition of precipitation over southeast Asia, Journal of Geophysical Research: Atmospheres (1984–2012), 103, 28 721–28 742, 1998.

Araguás-Araguás, L., Froehlich, K., and Rozanski, K.: Deuterium and oxygen-18 isotope composition of precipitation and atmospheric moisture, Hydrological Processes, 14, 1341–1355, 2000.

Bader, J. and Latif, M.: The impact of decadal-scale Indian Ocean sea surface temperature anomalies on Sahelian rainfall and the North Atlantic Oscillation, Geophysical Research Letters, 30, 2169, 2003.

Bader, J. and Latif, M.: The 1983 drought in the West Sahel: a case study, Climate dynamics, 36, 463–472, 2011.

Barbante, C., Barnola, J.-M., Becagli, S., Beer, J., Bigler, M., Boutron, C., Blunier, T., Castellano, E., Cattani, O., Chappellaz, J., et al.: One-to-one coupling of glacial climate variability in Greenland and Antarctica, Nature, 444, 195–198, 2006.

Berger, A.: Long-term variations of daily insolation and Quaternary climatic changes, Journal of the Atmospheric Sciences, 35, 2362–2367, 1978.

Berkelhammer, M., Risi, C., Kurita, N., and Noone, D.: The moisture source sequence for the Madden-Julian Oscillation as derived from satellite retrievals of HDO and H_2O, Journal of Geophysical Research, 117, D03 106, 2012a.

Berkelhammer, M., Stott, L., Yoshimura, K., Johnson, K., and Sinha, A.: Synoptic and mesoscale controls on the isotopic composition of precipitation in the western United States, Climate dynamics, pp. 1–22, 2012b.

Bijma, J., Spero, H., and Lea, D.: Reassessing foraminiferal stable isotope geochemistry: Impact of the oceanic carbonate system (experimental results), in: Use of proxies in paleoceanography, pp. 489–512, Springer, 1999.

Bonan, G. B.: Land surface model (LSM version 1.0) for ecological, hydrological, and atmospheric studies: Technical description and users guide. Technical note, Tech. rep., National Center for Atmospheric Research, Boulder, CO (United States). Climate and Global Dynamics Div., 1996.

BIBLIOGRAPHY

Bonan, G. B., Oleson, K. W., Vertenstein, M., Levis, S., Zeng, X., Dai, Y., Dickinson, R. E., and Yang, Z.-L.: The Land Surface Climatology of the Community Land Model Coupled to the NCAR Community Climate Model, Journal of Climate, 15, 3123–3149, 2002.

Bond, G., Heinrich, H., Broecker, W., Labeyrie, L., McManus, J., Andrews, J., Huon, S., Jantschik, R., Clasen, S., Simet, C., et al.: Evidence for massive discharges of icebergs into the North Atlantic ocean during the last glacial period, 1992.

Bony, S., Risi, C., and Vimeux, F.: Influence of convective processes on the isotopic composition (δ^{18}O and δD) of precipitation and water vapor in the tropics: 1. Radiative-convective equilibrium and Tropical Ocean–Global Atmosphere–Coupled Ocean-Atmosphere Response Experiment (TOGA-COARE) simulations, Journal of Geophysical Research, 113, D19 305, 2008.

Bowen, G. J.: Interpolating the isotopic composition of modern meteoric precipitation, Water Resources Research, 39, 1–13, 2003.

Braconnot, P., Joussaume, S., Noblet, N. D., and Ramstein, G.: Mid-Holocene and Last Glacial Maximum African monsoon changes as simulated within the Paleoclimate Modelling Intercomparison Project, Global and Planetary Change, 26, 51–66, 2000.

Braconnot, P., Otto-Bliesner, B., Harrison, S., Joussaume, S., Peterchmitt, J.-Y., Abe-Ouchi, A., Crucifix, M., Driesschaert, E., Fichefet, T., Hewitt, C., et al.: Results of PMIP2 coupled simulations of the Mid-Holocene and Last Glacial Maximum–Part 1: experiments and large-scale features, Climate of the Past, 3, 261–277, 2007.

Braconnot, P., Harrison, S. P., Kageyama, M., Bartlein, P. J., Masson-Delmotte, V., Abe-Ouchi, A., Otto-Bliesner, B., and Zhao, Y.: Evaluation of climate models using palaeoclimatic data, Nature Climate Change, 2012.

Brady, E. and Otto-Bliesner, B.: The role of meltwater-induced subsurface ocean warming in regulating the Atlantic meridional overturning in glacial climate simulations, Climate dynamics, 37, 1517–1532, 2011.

Briegleb, B., Bitz, C., Hunke, E., Lipscomb, W., and Schramm, J.: Description of the community climate system model version 2 sea ice model, National Center for Atmospheric Research, http://www. ccsm. ucar. edu/models/icecsim4, 2002.

Broccoli, A. and Manabe, S.: The effects of the Laurentide Ice Sheet on North American climate during the last glacial maximum, Géographie physique et Quaternaire, 41, 1987a.

Broccoli, A. and Manabe, S.: The influence of continental ice, atmospheric CO 2, and land albedo on the climate of the last glacial maximum, Climate Dynamics, 1, 87–99, 1987b.

BIBLIOGRAPHY

Broecker, W., Bond, G., Klas, M., Clark, E., and McManus, J.: Origin of the northern Atlantic's Heinrich events, Climate Dynamics, 6, 265–273, 1992.

Brown, D., Worden, J., and Noone, D.: Comparison of atmospheric hydrology over convective continental regions using water vapor isotope measurements from space, Journal of Geophysical Research, 113, D15 124, 2008.

Brown, D., Worden, J., and Noone, D.: Characteristics of tropical and subtropical atmospheric moistening derived from Lagrangian mass balance constrained by measurements of HDO and H_2O, Journal of Geophysical Research: Atmospheres, 2013.

Bush, A. and Philander, S.: The role of ocean-atmosphere interactions in tropical cooling during the last glacial maximum, Science, 279, 1341–1344, 1998.

Charles, C., Rind, D., Jouzel, J., Koster, R., and Fairbanks, R.: Glacial-interglacial changes in moisture sources for Greenland: Influences on the ice core record of climate, Science (Washington, DC);(United States), 263, 1994.

Chiang, J. C., Biasutti, M., and Battisti, D. S.: Sensitivity of the Atlantic intertropical convergence zone to last glacial maximum boundary conditions, Paleoceanography, 18, 1094, 2003.

Ciais, P. and Jouzel, J.: Deuterium and oxygen-18 in precipitation: Isotopic model, including mixed cloud processes, Journal of Geophysical Research, 99, 16 793–16, 1994.

Clapperton, C. M.: Nature of environmental changes in South America at the Last Glacial Maximum, Palaeogeography, Palaeoclimatology, Palaeoecology, 101, 189–208, 1993.

Clark, I. D. and Fritz, P.: Environmental isotopes in hydrogeology, CRC, 1997.

Cole, J. E., Rind, D., Webb, R. S., Jouzel, J., and Healy, R.: Climatic controls on interannual variability of precipitation $\delta^{18}O$: Simulated influence of temperature, precipitation amount, and vapor source region, Journal of geophysical research, 104, 14 223–14, 1999.

Collins, J. A., Schefuß, E., Heslop, D., Mulitza, S., Prange, M., Zabel, M., Tjallingii, R., Dokken, T. M., Huang, E., Mackensen, A., Schulz, M., Tian, J., Zarriess, M., and Wefer, G.: Interhemispheric symmetry of the tropical African rainbelt over the past 23,000 years, Nature Geoscience, 4, 42–45, doi:10.1038/ngeo1039, 2011.

Collins, J. A., Schefuß, E., Mulitza, S., Prange, M., Werner, M., Tharammal, T., Paul, A., and Wefer, G.: Estimating the hydrogen isotopic composition of past precipitation using leaf-waxes from western Africa, Quaternary Science Reviews, 65, 88–101, 2013.

BIBLIOGRAPHY

Collins, W. D., Rasch, P. J., Boville, B. A., Hack, J. J., McCaa, J. R., Williamson, D. L., Kiehl, J. T., Briegleb, B., Bitz, C., Lin, S., et al.: Description of the NCAR community atmosphere model (CAM 3.0), 2004.

Collins, W. D., Rasch, P. J., Boville, B. A., Hack, J. J., McCaa, J. R., Williamson, D. L., Briegleb, B. P., Bitz, C. M., Lin, S.-J., and Zhang, M.: The formulation and atmospheric simulation of the Community Atmosphere Model version 3 (CAM3), Journal of Climate, 19, 2144–2161, 2006.

Cook, K. H.: Generation of the African Easterly Jet and Its Role in Determining West African Precipitation, J. Climate, 12, 1165–1184, 1999.

Craig, H.: Isotopic variations in meteoric waters, Science, 133, 1702–1703, 1961.

Craig, H. and Gordon, L. I.: Deuterium and oxygen-18 variations in the ocean and the marine atmosphere, Consiglio nazionale delle richerche, Laboratorio de geologia nucleare, 1965.

Cuffey, K. M. and Clow, G. D.: Temperature, accumulation, and ice sheet elevation in central Greenland through the last deglacial transition, Journal of Geophysical Research, 102, 26 383–26, 1997.

Cuffey, K. M., Alley, R. B., Grootes, P. M., Bolzan, J. M., and Anandakrishnan, S.: Calibration of the δ^{18}O isotopic paleothermometer for central Greenland, using borehole temperatures, Journal of Glaciology, 40, 341–349, 1994.

d'Abreton, P. and Tyson, P.: Divergent and non-divergent water vapour transport over southern Africa during wet and dry conditions, Meteorology and Atmospheric Physics, 55, 47–59, 1995.

Dahe, Q.: Distribution of stable isotopes in surface snow along the route of the 1990 International Trans-Antarctica Expedition, Journal of Glaciology, 40, 1994.

Dahl-Jensen, D., Mosegaard, K., Gundestrup, N., Clow, G. D., Johnsen, S. J., Hansen, A. W., and Balling, N.: Past temperatures directly from the Greenland ice sheet, Science, 282, 268–271, 1998.

Dansgaard, W.: Stable isotopes in precipitation, Tellus, 16, 436–468, 1964.

Dansgaard, W., Johnsen, S., Clausen, H., and Gundestrup, N.: Stable isotope glaciology, vol. 197, CA Reitzel, 1973.

Deardorff, J.: A parameterization of ground-surface moisture content for use in atmospheric prediction models, Journal of Applied Meteorology, 16, 1977.

deMenocal, P., Ortiza, J., Guildersonb, T., Adkinsa, J., Sarntheinc, M., Bakera, L., and Yarusinskya, M.: Abrupt onset and termination of the African Humid Period : rapid climate responses to gradual insolation forcing, Quaternary Science Reviews, 19, 347–361, 2000.

BIBLIOGRAPHY

Deser, C., Capotondi, A., Saravanan, R., and Phillips, A. S.: Tropical Pacific and Atlantic climate variability in CCSM3, Journal of climate, 19, 2451–2481, 2005.

Dettman, D., Kohn, M., Quade, J., Ryerson, F., Ojha, T., and Hamidullah, S.: Seasonal stable isotope evidence for a strong Asian monsoon throughout the past 10.7 my, Geology, 29, 31–34, 2001.

Dickinson, R. E., Oleson, K. W., Bonan, G., Hoffman, F., Thornton, P., Vertenstein, M., Yang, Z.-L., and Zeng, X.: The Community Land Model and its climate statistics as a component of the Community Climate System Model, Journal of Climate, 19, 2302–2324, 2006.

Doherty, R., Kutzbach, J., Foley, J., and Pollard, D.: Fully coupled climate/dynamical vegetation model simulations over Northern Africa during the mid-Holocene, Climate Dynamics, 16, 561–573, doi:10.1007/s003820000065, 2000.

Duplessy, J.-C., Labeyrie, L., and Waelbroeck, C.: Constraints on the ocean oxygen isotopic enrichment between the Last Glacial Maximum and the Holocene: Paleoceanographic implications, Quaternary Science Reviews, 21, 315–330, 2002.

Fairbanks, R. G.: A 17, 000-year glacio-eustatic sea level record: influence of glacial melting rates on the Younger Dryas event and deep-ocean circulation, Nature, 342, 637–642, 1989.

Feng, X., Faiia, A. M., and Posmentier, E. S.: Seasonality of isotopes in precipitation: A global perspective, Journal of Geophysical Research, 114, D08 116, 2009.

Field, R. D., Jones, D. B., and Brown, D. P.: Effects of postcondensation exchange on the isotopic composition of water in the atmosphere, Journal of Geophysical Research, 115, D24 305, 2010.

Frankenberg, C., Yoshimura, K., Warneke, T., Aben, I., Butz, A., Deutscher, N., Griffith, D., Hase, F., Notholt, J., Schneider, M., et al.: Dynamic processes governing lower-tropospheric HDO/H_2O ratios as observed from space and ground, Science, 325, 1374–1377, 2009.

Friederichs, P. and Paeth, H.: Seasonal prediction of African precipitation with ECHAM4 T42 ensemble simulations using a multivariate MOS recalibration scheme, Climate Dynamics, 27, 761–786, 2006.

Gasse, F.: Hydrological changes in the African tropics since the Last Glacial Maximum, Quaternary Science Reviews, 19, 189–211, 2000.

Gat, J.: Isotope hydrology: A study of the water cycle, vol. 6, Imperial College Press, London, 2010.

Gat, J. R.: Oxygen and hydrogen isotopes in the hydrologic cycle, Annual Review of Earth and Planetary Sciences, 24, 225–262, 1996.

BIBLIOGRAPHY

Gates, W. L., Boyle, J. S., Covey, C., Dease, C. G., Doutriaux, C. M., Drach, R. S., Fiorino, M., Gleckler, P. J., Hnilo, J. J., Marlais, S. M., et al.: An overview of the results of the Atmospheric Model Intercomparison Project (AMIP I), Bulletin of the American Meteorological Society, 80, 29–55, 1999.

Giannini, A., Saravanan, R., and Chang, P.: Oceanic forcing of Sahel rainfall on interannual to interdecadal time scales, Science, 302, 1027–1030, 2003.

Gonfiantini, R., Roche, M., Olivry, J., Fontes, J., and Zuppi, G.: The altitude effect on the isotopic composition of tropical rains, Chemical Geology, 181, 147–167, 2001.

Grootes, P. and Stuiver, M.: Oxygen 18/16 variability in Greenland snow and ice with 10^{-3}- to 10^5-year time resolution, Journal of Geophysical Research, 102, 26 455–26, 1997.

Hack, J. J.: Parameterization of moist convection in the National Center for Atmospheric Research community climate model (CCM2), Journal of Geophysical Research: Atmospheres (1984–2012), 99, 5551–5568, 1994.

Hack, J. J., Caron, J. M., Yeager, S. G., Oleson, K. W., Holland, M. M., Truesdale, J. E., and Rasch, P. J.: Simulation of the global hydrological cycle in the CCSM Community Atmosphere Model version 3 (CAM3): Mean features, Journal of climate, 19, 2199–2221, 2006.

Hansen, J., Lacis, A., Rind, D., Russell, G., Stone, P., Fung, I., Ruedy, R., and Lerner, J.: Climate sensitivity: Analysis of feedback mechanisms, Geophysical Monograph Series, 29, 130–163, 1984.

Hastenrath, S.: Decadal-scale changes of the circulation in the tropical Atlantic sector associated with Sahel drought, International Journal of Climatology, 10, 459–472, 1990.

Heinrich, H.: Origin and consequences of cyclic ice rafting in the northeast Atlantic Ocean during the past 130,000 years, Quaternary research, 29, 142–152, 1988.

Hemming, S.: Heinrich events: Massive late Pleistocene detritus layers of the North Atlantic and their global climate imprint, Reviews of Geophysics, 42, RG1005, 2004.

Henderson-Sellers, A.: Improving land-surface parameterization schemes using stable water isotopes: Introducing the 'iPILPS' initiative, Global and Planetary Change, 51, 3–24, 2006.

Herold, M. and Lohmann, G.: Eemian tropical and subtropical African moisture transport: an isotope modelling study, Climate dynamics, 33, 1075–1088, 2009.

Hewitt, C. and Mitchell, J.: Radiative forcing and response of a GCM to ice age boundary conditions: cloud feedback and climate sensitivity, Climate Dynamics, 13, 821–834, 1997.

BIBLIOGRAPHY

Hewitt, C. D. and Mitchell, J. F. B.: GCM simulations of the climate of 6 kys BP: mean changes and interdecadal variability, Journal of Climate, 9, 3505–3529, 1996.

Hoffmann, G. and Heimann, M.: Water isotope modeling in the Asian monsoon region, Quaternary International, 37, 115–128, 1997.

Hoffmann, G., Werner, M., and Heimann, M.: Water isotope module of the ECHAM atmospheric general circulation model: A study on timescales from days to several years, Journal of Geophysical Research, 103, e16, 1998.

Hoffmann, G., Jouzel, J., and Masson, V.: Stable water isotopes in atmospheric general circulation models, Hydrological Processes, 14, 1385–1406, 2000.

Horita, J., Rozanski, K., and Cohen, S.: Isotope effects in the evaporation of water: a status report of the Craig–Gordon model, Isotopes in Environmental and Health Studies, 44, 23–49, 2008.

Hurrell, J. W., Hack, J. J., Shea, D., Caron, J. M., and Rosinski, J.: A new sea surface temperature and sea ice boundary dataset for the Community Atmosphere Model, Journal of Climate, 21, 5145–5153, 2008.

IAEA/WMO.: Global Network of Isotopes in Precipitation: The GNIP database, available at: http://www-naweb.iaea.org/napc/ih/IHS resources gnip.html (last access; 10 April 2012), 2006.

IPCC (Intergovernmental Panel on Climate Change); Solomon, S., et al. (Eds.).: Climate change 2007: the Physical Science Basis. Contribution of Working Group I to the Fourth Assessment Report of the Intergovernmental Panel on Climate Change. Summary for Policymakers., Cambridge, UK and New York, USA: Cambridge University Press, 996pp, 2007.

Johnsen, S. J., Dansgaard, W., Clausen, H., and Langway, C.: Oxygen isotope profiles through the Antarctic and Greenland ice sheets, Nature, 235, 429–434, 1972.

Johnsen, S. J., Dansgaard, W., and White, J.: The origin of Arctic precipitation under present and glacial conditions, Tellus B, 41, 452–468, 1989.

Johnsen, S. J., Dahl-Jensen, D., Gundestrup, N., Steffensen, J. P., Clausen, H. B., Miller, H., Masson-Delmotte, V., Sveinbjörnsdottir, A. E., and White, J.: Oxygen isotope and palaeotemperature records from six Greenland ice-core stations: Camp Century, Dye-3, GRIP, GISP2, Renland and NorthGRIP, Journal of Quaternary Science, 16, 299–307, 2001.

Johnson, K. R. and Ingram, B. L.: Spatial and temporal variability in the stable isotope systematics of modern precipitation in China: implications for paleoclimate reconstructions, Earth and Planetary Science Letters, 220, 365–377, 2004.

BIBLIOGRAPHY

Joussaume, S. and Jouzel, J.: Paleoclimatic tracers: An investigation using an atmospheric general circulation model under ice age conditions: 2. Water isotopes, Journal of Geophysical Research, 98, 2807–2830, 1993.

Joussaume, S., Taylor, K. E., Mitchell, F. B., Kutzbach, E., Harrison, S. P., Prentice, I. C., Broccoli, A. J., Bonfils, C., Dong, B., Guiot, J., Henerich, K., Hewitt, C. D., Jolly, D., Kim, J. W., Kislov, A., Kitoh, A., Loutre, M. F., Masson, V., Mcavaney, B., Mcfarlane, N., Nobler, N. D., Peltier, W. R., Pollard, I. D., Rind, D., Royer, F., Schlesinger, M. E., Valdes, P., Vettoretti, G., Webb, R. S., and Wyputta, U.: Monsoon changes for 6000 years ago : Results of 18 simulations from the Paleoclimate Modeling Intercomparison Project (PMIP) TM, Geophys. Res. Letters, 26, 859–862, 1999.

Jouzel, J.: Water stable isotopes: Atmospheric composition and applications in polar ice core studies, Treatise on Geochemistry, 4, 213–243, 2003.

Jouzel, J. and Merlivat, L.: Deuterium and oxygen-18 in precipitation: Modeling of the isotopic effects during snow formation, Journal of Geophysical Research: Atmospheres (1984–2012), 89, 11 749–11 757, 1984.

Jouzel, J., Russell, G., Suozzo, R., Koster, R., White, J., and Broecker, W.: Simulations of the HDO and $H_2^{18}O$ atmospheric cycles using the NASA GISS general circulation model: the seasonal cycle for present-day conditions, Journal of Geophysical Research, 92, 14 739–14, 1987.

Jouzel, J., Koster, R. D., Suozzo, R. J., and Russell, G. L.: Stable water isotope behavior during the last glacial maximum: A general circulation model analysis, Journal of Geophysical Research, 99, 25 791–25, 1994.

Jouzel, J., Alley, R. B., Cuffey, K., Dansgaard, W., Grootes, P., Hoffmann, G., Johnsen, S. J., Koster, R., Peel, D., Shuman, C., et al.: Validity of the temperature reconstruction from water isotopes in ice cores, Journal of Geophysical Research, 102, 26–26, 1997.

Jouzel, J., Hoffmann, G., Koster, R., and Masson, V.: Water isotopes in precipitation:: data/model comparison for present-day and past climates, Quaternary Science Reviews, 19, 363–379, 2000.

Kageyama, M. and Valdes, P. J.: Impact of the North American ice-sheet orography on the Last Glacial Maximum eddies and snowfall, Geophysical research letters, 27, 1515–1518, 2000.

Kiehl, J., Hack, J., Bonan, G., Boville, B., Williamson, D., and Rasch, P.: The national center for atmospheric research community climate model: CCM3, Journal of Climate, 11, 1131–1149, 1998.

Kim, S.-J.: The effect of atmospheric CO_2 and ice sheet topography on LGM climate, Climate dynamics, 22, 639–651, 2004.

BIBLIOGRAPHY

Kim, S.-J., Flato, G., Boer, G., and McFarlane, N.: A coupled climate model simulation of the Last Glacial Maximum, Part 1: transient multi-decadal response, Climate Dynamics, 19, 515–537, 2002.

Kim, S.-J., Crowley, T. J., Erickson, D. J., Govindasamy, B., Duffy, P. B., and Lee, B. Y.: High-resolution climate simulation of the last glacial maximum, Climate Dynamics, 31, 1–16, 2007.

Krandick, A.: Incorporation and simulation of stable water isotopes in the ocean circulation model MITgcm, Master's thesis, University of Bremen, Bremen, 2013.

Kutzbach, J. E. and Guetter, P. J.: The influence of changing orbital parameters and surface boundary conditions on climate simulations for the past 18, 000 years, Journal of the Atmospheric Sciences, 43, 1726–1759, 1986.

Kutzbach, J. E. and Liu, Z.: Response of the African Monsoon to Orbital Forcing and Ocean Feedbacks in the Middle Holocene Response of the African Monsoon to Orbital Forcing and Ocean Feedbacks in the Middle Holocene, Science, 278, 440–443, doi:10.1126/science.278.5337.440, 1997.

Kutzbach, J. E., Bonan, G., and Foley, J.: Vegetation and soil feedbacks on the response of the African monsoon to orbital forcing in the early to middle Holocene, Nature, 384, 623–626, 1996.

Lamb, P. J.: Case Studies of Tropical Atlantic Surface Circulation Patterns During Recent Sub-Saharan Weather Anomalies: 1967 and 1968, Monthly Weather Review, 106, 482–491, 1978.

Lambeck, K. and Chappell, J.: Sea level change through the last glacial cycle, Science, 292, 679–686, 2001.

Latif, M., Dommenget, D., Dima, M., and Grötzner, A.: The Role of Indian Ocean Sea Surface Temperature in Forcing East African Rainfall Anomalies during December–January 1997/98, Journal of Climate, 12, 3497–3504, 1999.

Lautenschlager, M. and Santer, B. D.: Atmospheric Response to a Hypothetical Tibetan Ice Sheet., Journal of climate, 4, 386–394, 1991.

Lawrence, J. R., Gedzelman, S. D., Dexheimer, D., Cho, H.-K., Carrie, G. D., Gasparini, R., Anderson, C. R., Bowman, K. P., and Biggerstaff, M. I.: Stable isotopic composition of water vapor in the tropics, Journal of Geophysical Research: Atmospheres (1984–2012), 109, 2004.

Lee, J.-E. and Fung, I.: "Amount effect" of water isotopes and quantitative analysis of post-condensation processes, Hydrological Processes, 22, 1–8, 2008.

Lee, J.-E., Fung, I., DePaolo, D. J., and Henning, C. C.: Analysis of the global distribution of water isotopes using the NCAR atmospheric general circulation model, Journal of Geophysical Research, 112, D16 306, 2007.

BIBLIOGRAPHY

Lee, J.-E., Fung, I., DePaolo, D. J., and Otto-Bliesner, B.: Water isotopes during the Last Glacial Maximum: New general circulation model calculations, Journal of Geophysical Research, 113, D19 109, 2008.

Lee, J.-E., Johnson, K., and Fung, I.: Precipitation over South America during the Last Glacial Maximum: An analysis of the "amount effect" with a water isotope-enabled general circulation model, Geophysical Research Letters, 36, 1–5, 2009.

Lee, J.-E., Risi, C., Fung, I., Worden, J., Scheepmaker, R. A., Lintner, B., and Frankenberg, C.: Asian monsoon hydrometeorology from TES and SCIA-MACHY water vapor isotope measurements and LMDZ simulations: Implications for speleothem climate record interpretation, Journal of Geophysical Research, 117, D15 112, 2012.

LeGrande, A. N. and Schmidt, G. A.: Sources of Holocene variability of oxygen isotopes in paleoclimate archives, Climate of the Past, 5, 441–455, doi:10.5194/cp-5-441-2009, 2009.

Levin, N. E., Zipser, E. J., and Cerling, T. E.: Isotopic composition of waters from Ethiopia and Kenya: Insights into moisture sources for eastern Africa, Journal of Geophysical Research, 114, 1–13, doi:10.1029/2009JD012166, 2009.

Levis, S., Bonan, G. B., and Bonfils, C.: Soil feedback drives the mid-Holocene North African monsoon northward in fully coupled CCSM2 simulations with a dynamic vegetation model, Climate Dynamics, 23, 791–802, 2004.

Lewis, S. C., LeGrande, A. N., Kelley, M., and Schmidt, G. A.: Water vapour source impacts on oxygen isotope variability in tropical precipitation during Heinrich events, Climate of the Past, 6, 325–343, doi:10.5194/cp-6-325-2010, 2010.

Liu, Z., Carlson, A., He, F., Brady, E., Otto-Bliesner, B., Briegleb, B., Wehrenberg, M., Clark, P., Wu, S., Cheng, J., et al.: Younger Dryas cooling and the Greenland climate response to CO_2., Proceedings of the National Academy of Sciences of the United States of America, 109, 11 101, 2012.

Lorius, C., Ritz, C., Jouzel, J., Merlivat, L., and Barkov, N.: A 150,000-year climatic record from Antarctic ice, Nature, 316, 591–596, 1985.

Luz, B., Barkan, E., Yam, R., and Shemesh, A.: Fractionation of oxygen and hydrogen isotopes in evaporating water, Geochimica et Cosmochimica Acta, 73, 6697–6703, 2009.

Lynch-Stieglitz, J.: Tracers of past ocean circulation, The Oceans and Marine Geochemistry, Treatise on Geochemistry, 6, 433–451, 2003.

Mackensen, A. and Bickert, T.: Stable carbon isotopes in benthic foraminifera: proxies for deep and bottom water circulation and new production, in: Use of proxies in paleoceanography, pp. 229–254, Springer, 1999.

BIBLIOGRAPHY

Mackensen, A., Grobe, H., Hubberten, H.-W., Spiess, V., and Fütterer, D.: Stable isotope stratigraphy from the Antarctic continental margin during the last one million years, Marine geology, 87, 315–321, 1989.

Mahfouf, J., Cariolle, D., Royer, J., Geleyn, J., and Timbal, B.: Response of the Meteo-France climate model to changes in CO_2 and sea surface temperature, Climate dynamics, 9, 345–362, 1994.

Majoube, M.: Fractionation Factor of ^{18}O between water vapour and ice., Nature, 226, 1242, 1970.

Majoube, M.: Oxygen-18 and deuterium fractionation between water and steam, J. Chim. Phys. Phys. Chim. Biol, 68, 1423–1436, 1971.

Manabe, S.: Climate and the ocean circulation 1. The atmospheric circulation and the hydrology of earth's surface, Monthly Weather Review, 97, 739–774, 1969.

Manabe, S. and Broccoli, A.: The influence of continental ice sheets on the climate of an ice age, J. geophys. Res, 90, 2167–2190, 1985.

MARGO Project Members: Constraints on the magnitude and patterns of ocean cooling at the Last Glacial Maximum, Nat Geosci., 2, 127–332, 2009.

Masson-Delmotte, V., Kageyama, M., Braconnot, P., Charbit, S., Krinner, G., Ritz, C., Guilyardi, E., Jouzel, J., Abe-Ouchi, A., Crucifix, M., et al.: Past and future polar amplification of climate change: climate model intercomparisons and ice-core constraints, Climate Dynamics, 26, 513–529, 2006.

Masson-Delmotte, V., Hou, S., Ekaykin, A., Jouzel, J., Aristarain, A., Bernardo, R., Bromwich, D., Cattani, O., Delmotte, M., Falourd, S., et al.: A Review of Antarctic Surface Snow Isotopic Composition: Observations, Atmospheric Circulation, and Isotopic Modeling, Journal of Climate, 21, 3359–3387, 2008.

Masson-Delmotte, V., Buiron, D., Ekaykin, A., Frezzotti, M., Gallée, H., Jouzel, J., Krinner, G., Landais, A., Motoyama, H., Oerter, H., et al.: A comparison of the present and last interglacial periods in six Antarctic ice cores, Climate of the Past, 7, 397–423, 2011.

McCaa, J. R., Rothstein, M., Eaton, B. E., Rosinski, J. M., Kluzek, E., and Vertenstein, M.: User's Guide to the NCAR Community Atmosphere Model (CAM 3.0), 2004.

McManus, J., Francois, R., Gherardi, J., Keigwin, L., and Brown-Leger, S.: Collapse and rapid resumption of Atlantic meridional circulation linked to deglacial climate changes, Nature, 428, 834–837, 2004.

Meehl, G. A., Arblaster, J. M., Lawrence, D. M., Seth, A., Schneider, E. K., Kirtman, B. P., and Min, D.: Monsoon regimes in the CCSM3, Journal of climate, 19, 2482–2495, 2006.

BIBLIOGRAPHY

Merkel, U., Prange, M., and Schulz, M.: ENSO variability and teleconnections during glacial climates, Quaternary Science Reviews, 29, 86–100, 2010.

Merlivat, L. and Jouzel, J.: Global climatic interpretation of the deuterium-oxygen-18 relationship for precipitation, Journal of Geophysical Research, 84, 5029–5033, 1979.

Merlivat, L. and Nief, G.: Fractionnement isotopique lors des changements d'état solide-vapeur et liquide-vapeur de l'eau à des températures inférieures à 0°C, Tellus, 19, 122–127, 1967.

Mulitza, S., Dürkoop, A., Hale, W., Wefer, G., and Niebler, H. S.: Planktonic foraminifera as recorders of past surface-water stratification, Geology, 25, 335–338, 1997.

Mulitza, S., Boltovskoy, D., Donner, B., Meggers, H., Paul, A., and Wefer, G.: Temperature: $\delta^{18}O$ relationships of planktonic foraminifera collected from surface waters, Palaeogeography, Palaeoclimatology, Palaeoecology, 202, 143–152, 2003.

Mulitza, S., Prange, M., Stuut, J.-B., Zabel, M., von Dobeneck, T., Itambi, A. C., Nizou, J., Schulz, M., and Wefer, G.: Sahel megadroughts triggered by glacial slowdowns of Atlantic meridional overturning, Paleoceanography, 23, 1–11, doi: 10.1029/2008PA001637, 2008.

Nicholson, S.: A review of climate dynamics and climate variability in eastern Africa, in: In The Limnology, Climatology and Paleoclimatology of the East African Lakes, pp. 25–56, 1996.

Nicholson, S.: Land surface processes and Sahel climate, Reviews of Geophysics, 38, 117–139, 2000a.

Nicholson, S.: The nature of rainfall variability over Africa on time scales of decades to millenia, Global and Planetary Change, 26, 137–158, 2000b.

Nicholson, S.: Climatic and environmental change in Africa during the last two centuries, Climate Research, 17, 123–144, 2001.

Niebler, H.-S., Hubberten, H.-W., and Gersonde, R.: Oxygen isotope values of planktic foraminifera: A tool for the reconstruction of surface water stratification, in: Use of Proxies in Paleoceanography, pp. 165–189, Springer, 1999.

Noone, D.: Water isotopes in CCSM for studying water cycles in the climate system, in: 8th Annual CCSM workshop, Breckenridge, Colorado, 2003.

Noone, D.: Isotopic composition of water vapor modeled by constraining global climate simulations with reanalyses, Research Activities in Atmospheric and Oceanic Modeling, pp. 2–37, 2006.

Noone, D.: The influence of midlatitude and tropical overturning circulation on the isotopic composition of atmospheric water vapor and Antarctic precipitation, Journal of Geophysical Research: Atmospheres (1984–2012), 113, 2008.

Noone, D. and Simmonds, I.: Associations between δ^{18}O of Water and Climate Parameters in a Simulation of Atmospheric Circulation for 1979-95, Journal of Climate, 15, 3150–3169, 2002.

Noone, D. and Sturm, C.: Comprehensive dynamical models of global and regional water isotope distributions, Isoscapes, pp. 195–219, 2010.

Otto-Bliesner, B. L., Brady, E. C., Clauzet, G., Tomas, R., Levis, S., and Kothavala, Z.: Last glacial maximum and Holocene climate in CCSM3, Journal of Climate, 19, 2526–2544, 2006a.

Otto-Bliesner, B. L., Tomas, R., Brady, E. C., Ammann, C., Kothavala, Z., and Clauzet, G.: Climate sensitivity of moderate-and low-resolution versions of CCSM3 to preindustrial forcings, Journal of climate, 19, 2567–2583, 2006b.

Otto-Bliesner, B. L., Schneider, R., Brady, E., Kucera, M., Abe-Ouchi, A., Bard, E., Braconnot, P., Crucifix, M., Hewitt, C., Kageyama, M., et al.: A comparison of PMIP2 model simulations and the MARGO proxy reconstruction for tropical sea surface temperatures at last glacial maximum, Climate dynamics, 32, 799–815, 2009.

Palmer, T.: Influence of the Atlantic, Pacific and Indian Oceans on Sahel rainfall, Nature, 322, 251–253, 1986.

Paul, A., Mulitza, S., Pätzold, J., and Wolff, T.: Simulation of oxygen isotopes in a global ocean model, in: Use of Proxies in Paleoceanography, pp. 655–686, Springer, 1999.

Pausata, F., Li, C., Wettstein, J., Kageyama, M., and Nisancioglu, K.: The key role of topography in altering North Atlantic atmospheric circulation during the last glacial period, Clim. Past, 7, 1089–1101, 2011a.

Pausata, F. S. R., Battisti, D. S., Nisancioglu, K. H., and Bitz, C. M.: Chinese stalagmite δ^{18}O controlled by changes in the Indian monsoon during a simulated Heinrich event, Nature Geoscience, 4, 474–480, 2011b.

Peltier, W.: Global glacial isostasy and the surface of the ice-age Earth: the ICE-5G (VM2) model and GRACE, Annu. Rev. Earth Planet. Sci., 32, 111–149, 2004.

Petit, J.-R., Jouzel, J., Raynaud, D., Barkov, N., Barnola, J., Basile, I., Bender, M., Chappellaz, J., Davis, M., Delaygue, G., et al.: Climate and atmospheric history of the past 420,000 years from the Vostok ice core, Antarctica, Nature, 399, 429–436, 1999.

BIBLIOGRAPHY

Poage, M. A. and Chamberlain, C. P.: Empirical relationships between elevation and the stable isotope composition of precipitation and surface waters: Considerations for studies of paleoelevation change, American Journal of Science, 301, 1–15, 2001.

Prell, W. L. and Kutzbach, J. E.: Monsoon Variability Over the Past 150,000 Years, Journal of Geophysical Research, 92, 8411–8425, doi:10.1029/JD092iD07p08411, 1987.

Prentice, I. C. and Jolly, D.: Mid-Holocene and glacial-maximum vegetation geography of the northern continents and Africa, Journal of Biogeography, 27, 507–519, doi:10.1046/j.1365-2699.2000.00425.x, 2000.

Rahn, T.: Hydrology: Tropical rain recycling, Nature, 445, 495–496, 2007.

Rasch, P. J. and Williamson, D. L.: On shape-preserving interpolation and semi-Lagrangian transport, SIAM journal on scientific and statistical computing, 11, 656–687, 1990.

Rayner, N., Parker, D., Horton, E., Folland, C., Alexander, L., Rowell, D., Kent, E., and Kaplan, A.: Global analyses of sea surface temperature, sea ice, and night marine air temperature since the late nineteenth century, Journal of Geophysical Research, 108, 4407, 2003.

Richter, J. and Rasch, P.: Effects of convective momentum transport on the atmospheric circulation in the Community Atmosphere Model, version 3, Journal of Climate, 21, 1487–1499, 2008.

Rind, D.: Components of the ice age circulation, Journal of Geophysical Research, 92, 4241–4281, 1987.

Risi, C., Bony, S., and Vimeux, F.: Influence of convective processes on the isotopic composition (δ^{18}O and δD) of precipitation and water vapor in the tropics: 2. Physical interpretation of the amount effect, Journal of Geophysical Research, 113, D19 306, 2008a.

Risi, C., Bony, S., Vimeux, F., Descroix, L., Ibrahim, B., Lebreton, E., Mamadou, I., and Sultan, B.: What controls the isotopic composition of the African monsoon precipitation? Insights from event-based precipitation collected during the 2006 AMMA field campaign, Geophysical research letters, 35, 1–6, doi:10.1029/2008GL035920, 2008b.

Risi, C., Bony, S., Vimeux, F., Chong, M., and Descroix, L.: Evolution of the stable water isotopic composition of the rain sampled along Sahelian squall lines, Quarterly Journal of the Royal Meteorological Society, 136, 227–242, 2010a.

Risi, C., Bony, S., Vimeux, F., Frankenberg, C., Noone, D., and Worden, J.: Understanding the Sahelian water budget through the isotopic composition of water vapor and precipitation, Journal of Geophysical Research, 115, D24 110, 2010b.

BIBLIOGRAPHY

Risi, C., Bony, S., Vimeux, F., and Jouzel, J.: Water-stable isotopes in the LMDZ4 general circulation model: Model evaluation for present-day and past climates and applications to climatic interpretations of tropical isotopic records, Journal of Geophysical Research, 115, D12 118, 2010c.

Risi, C., Noone, D., Worden, J., Frankenberg, C., Stiller, G., Kiefer, M., Funke, B., Walker, K., Bernath, P., Schneider, M., et al.: Process-evaluation of tropospheric humidity simulated by general circulation models using water vapor isotopologues: 1. Comparison between models and observations, Journal of Geophysical Research, 117, D05 303, 2012a.

Risi, C., Noone, D., Worden, J., Frankenberg, C., Stiller, G., Kiefer, M., Funke, B., Walker, K., Bernath, P., Schneider, M., et al.: Process-evaluation of tropospheric humidity simulated by general circulation models using water vapor isotopic observations: 2. Using isotopic diagnostics to understand the mid and upper tropospheric moist bias in the tropics and subtropics, Journal of Geophysical Research, 117, D05 304, 2012b.

Rowell, D. P.: The Impact of Mediterranean SSTs on the Sahelian Rainfall Season, Journal of Climate, 16, 849–862, 2003.

Rozanski, K. and Araguás-Araguás, L.: Spatial and temporal variability of stable isotope composition of precipitation over the South American continent, Bull. Inst. fr. études andines, 24, 379–390, 1995.

Rozanski, K. and Sonntag, C.: Vertical distribution of deuterium in atmospheric water vapour, Tellus, 34, 135–141, 1982.

Rozanski, K., Sonntag, C., and Münnich, K.: Factors controlling stable isotope composition of European precipitation, Tellus, 34, 142–150, 1982.

Rozanski, K., Araguás-Araguás, L., and Gonfiantini, R.: Isotopic patterns in modern global precipitation, Geophysical Monograph Series, 78, 1–36, 1993.

Rozanski, K., Johnsen, S. J., Schotterer, U., and Thompson, L.: Reconstruction of past climates from stable isotope records of palaeo-precipitation preserved in continental archives, Hydrological sciences journal, 42, 725–745, 1997.

Sauer, P. E., Miller, G. H., and Overpeck, J. T.: Oxygen isotope ratios of organic matter in arctic lakes as a paleoclimate proxy: field and laboratory investigations, Journal of Paleolimnology, 25, 43–64, 2001.

Scheepmaker, R. A., Frankenberg, C., Galli, A., Butz, A., Schrijver, H., Deutscher, N. M., Wunch, D., Warneke, T., Fally, S., and Aben, I.: Improved water vapour spectroscopy in the 4174-4300 cm^{-1} region and its impact on SCIAMACHY HDO/H_2O measurements, Atmospheric Measurement Techniques, 6, 879–894, doi: 10.5194/amt-6-879-2013, 2013.

BIBLIOGRAPHY

Schefuß, E., Schouten, S., and Schneider, R. R.: Climatic controls on central African hydrology during the past 20,000 years., Nature, 437, 1003–6, doi: 10.1038/nature03945, 2005.

Schefuß, E., Kuhlmann, H., Mollenhauer, G., Prange, M., and Pätzold, J.: Forcing of wet phases in southeast Africa over the past 17,000 years., Nature, 480, 509–12, doi:10.1038/nature10685, 2011.

Shackleton, N. J. and Opdyke, N. D.: Oxygen isotope and palaeomagnetic stratigraphy of Equatorial Pacific core V28-238: Oxygen isotope temperatures and ice volumes on a 10^5 year and 10^6 year scale, Quaternary research, 3, 39–55, 1973.

Schmidt, G. A.: Oxygen-18 variations in a global ocean model, Geophysical Research Letters, 25, 1201–1204, 1998.

Schmidt, G. A., LeGrande, A. N., and Hoffmann, G.: Water isotope expressions of intrinsic and forced variability in a coupled ocean-atmosphere model, Journal of geophysical research, 112, D10 103, 2007.

Severinghaus, J. P. and Brook, E. J.: Abrupt climate change at the end of the last glacial period inferred from trapped air in polar ice, Science, 286, 930–934, 1999.

Severinghaus, J. P., Sowers, T., Brook, E. J., Alley, R. B., and Bender, M. L.: Timing of abrupt climate change at the end of the Younger Dryas interval from thermally fractionated gases in polar ice, Nature, 391, 141–146, 1998.

Sharp, Z.: Principles of stable isotope geochemistry, Pearson Education Upper Saddle River, NJ, USA, 2007.

Shi, N., Dupont, L., Beug, H., and Schneider, R.: Vegetation and climate changes during the last 21 000 years in SW Africa based on a marine pollen record, Vegetation History and Archaeobotany, 7, 127–140, 1998.

Shin, S., Sardeshmukh, P., Webb, R., Oglesby, R., and Barsugli, J.: Understanding the mid-Holocene climate, Journal of climate, 19, 2801–2817, 2006.

Shin, S.-I., Liu, Z., Otto-Bliesner, B., Brady, E., Kutzbach, J., and Harrison, S.: A simulation of the Last Glacial Maximum climate using the NCAR-CCSM, Climate Dynamics, 20, 127–151, 2002.

Sime, L. C., Tindall, J. C., Wolff, E. W., Connolley, W. M., and Valdes, P. J.: Antarctic isotopic thermometer during a CO_2 forced warming event, Journal of Geophysical Research, 113, D24 119, 2008.

Slingo, J.: The development and verification of a cloud prediction scheme for the ECMWF model, Quarterly Journal of the Royal Meteorological Society, 113, 899–927, 1987.

BIBLIOGRAPHY

Stager, J., Ryves, D., Chase, B., and Pausata, F.: Catastrophic drought in the Afro-Asian monsoon region during Heinrich event 1, Science, 331, 1299–1302, 2011.

Staniforth, A. and Côté, J.: Semi-Lagrangian integration schemes for atmospheric models-a review, Monthly Weather Review, 119, 2206–2223, 1991.

Stein, U. and Alpert, P.: Factor separation in numerical simulations, Journal of the Atmospheric Sciences, 50, 2107–2115, 1993.

Stenni, B., Jouzel, J., Masson-Delmotte, V., Röthlisberger, R., Castellano, E., Cattani, O., Falourd, S., Johnsen, S., Longinelli, A., Sachs, J., et al.: A late-glacial high-resolution site and source temperature record derived from the EPICA Dome C isotope records (East Antarctica), Earth and Planetary Science Letters, 217, 183–195, 2004.

Stewart, M. K.: Stable isotope fractionation due to evaporation and isotopic exchange of falling waterdrops: Applications to atmospheric processes and evaporation of lakes, Journal of Geophysical Research, 80, 1133–1146, 1975.

Sturm, C., Vimeux, F., and Krinner, G.: Intraseasonal variability in South America recorded in stable water isotopes, Journal of Geophysical Research, 112, D20 118, 2007.

Sturm, C., Zhang, Q., and Noone, D.: An introduction to stable water isotopes in climate models: benefits of forward proxy modelling for paleoclimatology, Clim. Past, 6, 115–129, 2010.

Sundqvist, H.: Parameterization of condensation and associated clouds in models for weather prediction and general circulation simulation, in: Physically-based modelling and simulation of climate and climatic change, pp. 433–461, Springer, 1988.

Sylvestre, F.: Moisture Pattern During the Last Glacial Maximum in South America, Past Climate Variability in South America and Surrounding Regions, pp. 3–27, 2009.

Taylor, C.: The vertical variations of the isotopic concentrations of tropospheric water vapour over continental Europe and their relationship to tropospheric structure, NZ Inst. Nucl. Sci. Rep, p. 44, 1972.

Texier, D. and Noblet, N. D.: Sensitivity of the African and Asian monsoons to mid-Holocene insolation and data-inferred surface changes, Journal of Climate, 13, 164–181, 2000.

Tharammal, T., Paul, A., Merkel, U., and Noone, D.: Influence of Last Glacial Maximum boundary conditions on the global water isotope distribution in an atmospheric general circulation model, Climate of the Past, 9, 789–809, doi: 10.5194/cp-9-789-2013, 2013.

BIBLIOGRAPHY

Thompson, L. G., Mosley-Thompson, E., and Henderson, K. A.: Ice-core palaeoclimate records in tropical South America since the Last Glacial Maximum, Journal of Quaternary Science, 15, 377–394, 2000.

Thorncroft, C. D. and Blackburn, M.: Maintenance of the African easterly jet, Quarterly Journal of the Royal Meteorological Society, 125, 763–786, doi:10.1002/qj.49712555502, 1999.

Tierney, J. E., Russell, J. M., Huang, Y., Damstlé, J. S. S., Hopmans, E. C., and Cohen, A. S.: Northern hemisphere controls on tropical southeast African climate during the past 60,000 years., Science, 322, 252–255, 2008.

Tierney, J. E., Lewis, S. C., Cook, B. I., LeGrande, A. N., and Schmidt, G. A.: Model, proxy and isotopic perspectives on the East African Humid Period, Earth and Planetary Science Letters, 307, 103–112, doi:10.1016/j.epsl.2011.04.038, 2011a.

Tierney, J. E., Russell, J. M., Sinninghe, J. S., Huang, Y., and Verschuren, D.: Late Quaternary behavior of the East African monsoon and the importance of the Congo Air Boundary, Quaternary Science Reviews, 30, 798–807, doi:10.1016/j.quascirev.2011.01.017, 2011b.

Timbal, B., Mahfouf, J., Royer, J., Cubasch, U., and Murphy, J.: Comparison between doubled CO_2 time-slice and coupled experiments, Journal of climate, 10, 1463–1469, 1997.

Tindall, J., Valdes, P., and Sime, L. C.: Stable water isotopes in HadCM3: Isotopic signature of El Niño–Southern Oscillation and the tropical amount effect, Journal of Geophysical Research, 114, D04 111, 2009.

Todd, M., Washington, R., and Palmer, P.: Water vapour transport associated with tropical–temperate trough systems over southern Africa and the southwest Indian Ocean, International journal of climatology, 24, 555–568, 2004.

Trenberth, K. E.: Atmospheric moisture recycling: Role of advection and local evaporation, Journal of Climate, 12, 1368–1381, 1999.

Trenberth, K. E., Dai, A., Rasmussen, R. M., and Parsons, D. B.: The changing character of precipitation, Bulletin of the American Meteorological Society, 84, 1205–1218, 2003.

Ueda, H. T. and Garfield, D. E.: Drilling Through the Greenland Ice Sheet., Tech. rep., DTIC Document, 1968.

Ummenhofer, C. C., Sen Gupta, A., and England, H. M.: Contributions of Indian Ocean Sea Surface Temperatures to Enhanced East African Rainfall, J. Climate, 22, 993–1013, doi:10.1175/2008JCLI2493.1, 2009.

Van Campo, E.: Monsoon fluctuations in two 20,000-yr BP oxygen-isotope/pollen records off southwest India, Quaternary Research, 26, 376–388, 1986.

BIBLIOGRAPHY

Vidal, L., Labeyrie, L., Cortijo, E., Arnold, M., Duplessy, J., Michel, E., Becque, S., and Van Weering, T.: Evidence for changes in the North Atlantic Deep Water linked to meltwater surges during the Heinrich events, Earth and Planetary Science Letters, 146, 13–27, 1997.

Vuille, M., Bradley, R., Werner, M., Healy, R., and Keimig, F.: Modeling $\delta^{18}O$ in precipitation over the tropical Americas: 1. Interannual variability and climatic controls, Journal of Geophysical Research, 108, 4174, 2003.

Vuille, M., Werner, M., Bradley, R., and Keimig, F.: Stable isotopes in precipitation in the Asian monsoon region, Journal of Geophysical Research, 110, D23 108, 2005.

Washington, R. and Todd, M.: Tropical-temperate links in southern African and Southwest Indian Ocean satellite-derived daily rainfall, International journal of climatology, 19, 1601–1616, 1999.

Weaver, A., Eby, M., Fanning, A., and Wiebe, E.: Simulated influence of carbon dioxide, orbital forcing and ice sheets on the climate of the Last Glacial Maximum, Nature, 394, 847–853, 1998.

Webb, R., Rind, D., Lehman, S., Healy, R., Sigman, D., et al.: Influence of ocean heat transport on the climate of the Last Glacial Maximum, Nature, 385, 695–699, 1997.

Wefer, G., Berger, W., Bijma, J., and Fischer, G.: Clues to ocean history: a brief overview of proxies, in: Use of Proxies in Paleoceanography, pp. 1–68, Springer, 1999.

Werner, M., Mikolajewicz, U., Heimann, M., and Hoffmann, G.: Borehole Vesus Isotope Temperatures on Greenland: Seasonality Does Matter, Geophysical Research Letters, 27, No. 5, 2000.

Werner, M., Heimann, M., and Hoffmann, G.: Isotopic composition and origin of polar precipitation in present and glacial climate simulations, Tellus B, 53, 53–71, 2001.

Werner, M., Langebroek, P. M., Carlsen, T., Herold, M., and Lohmann, G.: Stable water isotopes in the ECHAM5 general circulation model: Toward high-resolution isotope modeling on a global scale, Journal of Geophysical Research: Atmospheres (1984–2012), 116, 2011.

White, J. W. and Gedzelman, S. D.: The isotopic composition of atmospheric water vapor and the concurrent meteorological conditions, Journal of Geophysical Research: Atmospheres (1984–2012), 89, 4937–4939, 1984.

Williamson, D. L. and Olson, J. G.: Climate simulations with a semi-Lagrangian version of the NCAR Community Climate Model, Monthly Weather Review;(United States), 122, 1994.

BIBLIOGRAPHY

Williamson, D. L. and Rasch, P. J.: Two-dimensional semi-Lagrangian transport with shape-preserving interpolation, Mon. Wea. Rev, 117, 102–129, 1989.

Williamson, D. L. and Rasch, P. J.: Water vapor transport in the NCAR CCM2, Tellus A, 46, 34–51, 1994.

Worden, J., Noone, D., Bowman, K., Beer, R., Eldering, A., Fisher, B., Gunson, M., Goldman, A., Herman, R., Kulawik, S. S., et al.: Importance of rain evaporation and continental convection in the tropical water cycle, Nature, 445, 528–532, 2007.

Wright, J. S., Sobel, A. H., and Schmidt, G. A.: Influence of condensate evaporation on water vapor and its stable isotopes in a GCM, Geophysical Research Letters, 36, L12 804, 2009.

Wu, H., Guiot, J., Brewer, S., and Guo, Z.: Climatic changes in Eurasia and Africa at the last glacial maximum and mid-Holocene: reconstruction from pollen data using inverse vegetation modelling, Climate Dynamics, 29, 211–229, 2007.

Wunch, D., Toon, G. C., Blavier, J.-F. L., Washenfelder, R. A., Notholt, J., Connor, B. J., Griffith, D. W., Sherlock, V., and Wennberg, P. O.: The total carbon column observing network, Philosophical Transactions of the Royal Society A: Mathematical, Physical and Engineering Sciences, 369, 2087–2112, 2011.

Xie, P. and Arkin, P.: Global precipitation: A 17-year monthly analysis based on gauge observations, satellite estimates, and numerical model outputs, Bulletin of the American Meteorological Society, 78, 2539–2558, 1997.

Yan, Z. and Petit-Maire, N.: The last 140 ka in the Afro-Asian arid/semi-arid transitional zone, Palaeogeography, Palaeoclimatology, Palaeoecology, 110, 217–233, 1994.

Yeager, S., Shields, C., Large, W., and Hack, J.: The low-resolution CCSM3, Journal of climate, 19, 2545–2566, 2006.

Yoshimura, K.: Effect of land surface processes on precipitation isotopes, in: Proceedings of the 6th International Study Conference on GEWEX in Asia and GAME, Kyoto, Japan, pp. 3–5, 2004.

Yoshimura, K., Oki, T., Ohte, N., and Kanae, S.: A quantitative analysis of short-term ^{18}O variability with a Rayleigh-type isotope circulation model, Journal of Geophysical research, 108, 4647, 2003.

Yoshimura, K., Miyazaki, S., Kanae, S., and Oki, T.: Iso-MATSIRO, a land surface model that incorporates stable water isotopes, Global and Planetary Change, 51, 90–107, 2006.

Yoshimura, K., Frankenberg, C., Kanamitsu, M., Worden, J., and Roeckmann, T.: Comparison of an isotopic atmospheric general circulation model with new quasi-global satellite measurements of water vapor isotopologues, Journal of Geophysical Research, 116, D19 118–1, 2011.

BIBLIOGRAPHY

Zhang, G. J. and McFarlane, N. A.: Sensitivity of climate simulations to the parameterization of cumulus convection in the Canadian Climate Centre general circulation model, Atmosphere-Ocean, 33, 407–446, 1995.

Zhang, G. J. and Mu, M.: Effects of modifications to the Zhang-McFarlane convection parameterization on the simulation of the tropical precipitation in the National Center for Atmospheric Research Community Climate Model, version 3, Journal of geophysical research, 110, D09 109, 2005.

Zhao, C., Liu, X., Leung, L. R., and Hagos, S.: Radiative impact of mineral dust on monsoon precipitation variability over West Africa, Atmos. Chem. Phys, 11, 1879–1893, 2011.

Zhao, Y., Braconnot, P., Marti, O., Harrison, S., Hewitt, C., Kitoh, a., Liu, Z., Mikolajewicz, U., Otto-Bliesner, B., and Weber, S.: A multi-model analysis of the role of the ocean on the African and Indian monsoon during the mid-Holocene, Climate Dynamics, 25, 777–800, doi:10.1007/s00382-005-0075-7, 2005.